



UNIVERSITAT POLITÈCNICA
DE CATALUNYA
BARCELONATECH

*Design optimization and
performance analysis
methodology for PMSMs
to improve efficiency
in hydraulic applications*

Carlos Andrés Candelo Zuluaga

ADVERTIMENT La consulta d'aquesta tesi queda condicionada a l'acceptació de les següents condicions d'ús: La difusió d'aquesta tesi per mitjà del repositori institucional UPCommons (<http://upcommons.upc.edu/tesis>) i el repositori cooperatiu TDX (<http://www.tdx.cat/>) ha estat autoritzada pels titulars dels drets de propietat intel·lectual **únicament per a usos privats** emmarcats en activitats d'investigació i docència. No s'autoritza la seva reproducció amb finalitats de lucre ni la seva difusió i posada a disposició des d'un lloc aliè al servei UPCommons o TDX. No s'autoritza la presentació del seu contingut en una finestra o marc aliè a UPCommons (*framing*). Aquesta reserva de drets afecta tant al resum de presentació de la tesi com als seus continguts. En la utilització o cita de parts de la tesi és obligat indicar el nom de la persona autora.

ADVERTENCIA La consulta de esta tesis queda condicionada a la aceptación de las siguientes condiciones de uso: La difusión de esta tesis por medio del repositorio institucional UPCommons (<http://upcommons.upc.edu/tesis>) y el repositorio cooperativo TDR (<http://www.tdx.cat/?locale-attribute=es>) ha sido autorizada por los titulares de los derechos de propiedad intelectual **únicamente para usos privados enmarcados** en actividades de investigación y docencia. No se autoriza su reproducción con finalidades de lucro ni su difusión y puesta a disposición desde un sitio ajeno al servicio UPCommons No se autoriza la presentación de su contenido en una ventana o marco ajeno a UPCommons (*framing*). Esta reserva de derechos afecta tanto al resumen de presentación de la tesis como a sus contenidos. En la utilización o cita de partes de la tesis es obligado indicar el nombre de la persona autora.

WARNING On having consulted this thesis you're accepting the following use conditions: Spreading this thesis by the institutional repository UPCommons (<http://upcommons.upc.edu/tesis>) and the cooperative repository TDX (<http://www.tdx.cat/?locale-attribute=en>) has been authorized by the titular of the intellectual property rights **only for private uses** placed in investigation and teaching activities. Reproduction with lucrative aims is not authorized neither its spreading nor availability from a site foreign to the UPCommons service. Introducing its content in a window or frame foreign to the UPCommons service is not authorized (*framing*). These rights affect to the presentation summary of the thesis as well as to its contents. In the using or citation of parts of the thesis it's obliged to indicate the name of the author.



UNIVERSITAT POLITÈCNICA
DE CATALUNYA
BARCELONATECH

PhD program in Electrical Engineering

Design Optimization and Performance Analysis Methodology for PMSMs to Improve Efficiency in Hydraulic Applications

Doctoral thesis by:

Carlos Andrés Candelo Zuluaga

Thesis advisors:

Dr. Jordi-Roger Riba Ruiz

Dr. Antoni Garcia Espinosa

Electrical Engineering Department

Terrassa, September 2021

“Invention is the most important product of man’s creative brain. The ultimate purpose is the complete mastery of mind over the material world, the harnessing of human nature to human needs.”

- *Nikola Tesla*

Abstract

In the recent years, water pumping and other hydraulic applications are increasingly demanding motors capable to operate under different working conditions, including variable pressure and volumetric flow demands. Moreover, the technical evolution trend of pumping components is to minimize the size, offering compact and adaptable hydraulic units. Hence, the need to optimize the electric motor part to reduce the volume according this trend, maximizing the efficiency, decreasing material and fabrication costs, reducing noise and improving thermal dissipation have originated the research field of this project.

So far different methodologies have been focused on designing electrical machines considering few aspects, such as the rated conditions with some size limitations. In addition, the optimization strategies have been based on single operation conditions, improving multiple aspects but not considering the overall performance of the machine and its influence with the working system.

This research changes the design and optimization paradigm, focusing on defining beforehand the desired performance of the electrical machine in relation with the application system. The customization is not limited to an operating point but to the whole performance space, which in this case is the torque-speed area. Thus, the designer has plenty of freedom to study the system, and define the desired motor performance establishing the size, thermal and mechanical limitations from the beginning of the process.

Moreover, when designing and optimizing electrical machines, the experimental validation is of major importance. From an industrial scope so far, the testing methodologies are focused on evaluating point by point the electrical machine performance, being a robust and trustable way to measure and validate the electrical machine characteristics. Nevertheless, this method requires a large time to prepare the experimental setup and to evaluate the whole motor performance. For this reason, there is a special interest on improving parameter estimation and performance evaluation techniques for electrical machines to reduce evaluation time, setup complexity and increase the number of physical magnitudes to measure in order to have deeper information. This research also develops methodologies to extend the electrical machine experimental validation providing information to evaluate the motor performance.

This doctoral thesis has been developed with a collaboration agreement between UPC and the company MIDTAL TALENTOS S.L. The thesis is included within the Industrial Doctorates program 2018 DI 019 promoted by the Generalitat de Catalunya.

Keywords

Permanent magnet machines Design optimization Design tools
Magnetic losses Finite element analysis Hydraulic applications
Finite element method Water pumps Parameter estimation
Performance analysis System identification Field oriented control

Sumario

En los últimos años, el bombeo de agua, entre otras aplicaciones hidráulicas, exige cada vez más motores capaces de operar en diferentes condiciones de trabajo, incluyendo las demandas variables de presión y caudal volumétrico. Además, la evolución técnica de los componentes de bombeo está cada vez más minimizando el tamaño, ofreciendo unidades hidráulicas compactas y adaptables. De ahí la necesidad de optimizar la parte del motor eléctrico para reducir el volumen de acuerdo con esta tendencia, maximizando la eficiencia, disminuyendo los costos de material y fabricación, reduciendo el ruido y mejorando la disipación térmica. Todos estos factores han creado el campo de investigación sobre el cual se desarrolla este proyecto.

Hasta ahora las metodologías se han centrado en diseñar las máquinas eléctricas considerando unos pocos aspectos técnicos, como las condiciones nominales con algunas limitaciones de tamaño. Además, las estrategias de optimización se han basado en condiciones de operación única, mejorando múltiples aspectos sin considerar el rendimiento general de la máquina y su influencia en el sistema de trabajo.

Esta investigación cambia el paradigma de diseño y optimización centrándose en definir de antemano el rendimiento deseado de la máquina eléctrica en relación con el sistema de aplicación. La personalización no se limita a un punto de funcionamiento sino a todo el espacio de operación, que en este caso se expresa en el espacio par-velocidad. Así, el diseñador tiene libertad para estudiar el sistema, definir el rendimiento deseado del motor estableciendo el tamaño, limitaciones térmicas y mecánicas desde el inicio del proceso.

Además, a la hora de diseñar y optimizar máquinas eléctricas, la validación experimental es de gran importancia. En el ámbito industrial hasta ahora, las metodologías de ensayo han sido enfocadas a evaluar punto por punto la máquina eléctrica, siendo una forma robusta y confiable de medir y validar sus características. Sin embargo, este método requiere mucho tiempo para preparar la configuración experimental y evaluar el motor en toda su zona de operación. Por esta razón, existe un interés especial en mejorar la estimación de parámetros y las técnicas de evaluación de la operación de las máquinas eléctricas reduciendo tiempo, complejidad y aumentando el número de magnitudes físicas a medir teniendo más información sobre la máquina. Esta investigación también desarrolla metodologías para extender la validación experimental de la máquina eléctrica proporcionando información para evaluar el rendimiento del motor.

Esta tesis doctoral ha sido desarrollada con un convenio de colaboración entre la Universidad Politécnica de Cataluña UPC y la empresa MIDTAL TALENTOS S.L. La tesis se engloba dentro del plan de Doctorados Industriales 2018 DI 019 impulsado por la Generalitat de Catalunya.

Acknowledgements

I would like first to thank my directors Dr. Jordi Roger Riba and Dr. Antoni Garcia Espinosa. Jordi, you have been during these three years an example of perseverance, guidance, dedication and integrity, especially in the most difficult moments where the sincere affection and comprehension given helped me to be in the right place at the right time with one of the most important people of my life. Toni, your experience, knowledge and humanity have been of major importance for the realization of this thesis and for my personal growth as a professional and researcher, your truly passion for this field inspired me being a role model of excellence in work and in life.

A special thank also to MIDTAL TALENTOS S.L, in particular to Ramón Vazquez for giving me the opportunity to undertake this thesis within the industrial PhD program. Thank you for showing faith towards me, for listening my contributions, new ideas and proposals in the projects involved in the company. I would like to thank him to make me feel part of the company. Also, special acknowledgements to my co-workers and friends Pere, Francesc and Carles for helping and integrating me within the company.

Me gustaría darle un especial agradecimiento a mi familia. A mi padre Carlos, ya no estás aquí, pero tu luz y tu fortaleza sigue entre nosotros, sé que de algún modo este paso lo damos juntos. A mi madre Zulay, sin ti todo esto no tendría ningún sentido, sin el cariño, dedicación y esfuerzo empleados durante todo este tiempo no hubiese aprendido lo más importante de mi vida, este paso también lo damos juntos. A Núria, por el apoyo y amor incondicional brindados incluso en los peores momentos. A mis amigos y hermanos Antonio, Alberto y Rincón, siempre habéis estado y siempre estaréis. A mi familia en Colombia, vuestro orgullo es mi orgullo.

Me gustaría agradecer a mis compañeros y amigos del laboratorio AMBER, Akash, David, Gabriel, Jimmy, Liu, Pau, también a estudiantes como Dinesh, Nabil, Marc y tantos otros con los que tuve la suerte de compartir tantas risas y apoyo durante este camino. También me gustaría agradecer a Manuel Moreno por aportar su buen humor y actitud, además de ayudarme con los ensayos. A los compañeros y amigos del grupo MCIA, especialmente a Alejandro y Carles por contagiarme tanta energía y pasión por el trabajo bien hecho. A Geovany, Víctor, Eva y Paco, por lo poco compartido, pero de grandísima calidad.

A mis compañeros y amigos del Kung Fu, por estar ahí cuando más lo necesitaba y enseñarme la faceta más sincera de la amistad.

Table of Contents

Table of Contents	x
Index of figures	xiii
Index of tables.....	xvii
1. Introduction.....	1
1.1 <i>Research topic.....</i>	2
1.2 <i>Working system</i>	5
1.3 <i>Hypotheses.....</i>	8
1.4 <i>Goals and objectives</i>	10
2. State of the art.....	11
2.1 <i>Synchronous machine technology</i>	12
2.2 <i>Classical electromagnetic design.....</i>	16
2.3 <i>Reluctance and thermal networks.....</i>	23
2.4 <i>Design based on anisotropic layer theory machine analytic model</i>	27
2.5 <i>Electromagnetic, thermal and mechanical finite element analysis.....</i>	29
2.6 <i>Electrical machines optimization methodologies</i>	38
2.7 <i>Recent developments in design optimization of PMSM.....</i>	41
2.8 <i>Recent developments in design optimization of electrical machines for hydraulic applications</i>	42
2.9 <i>Recent developments in parameter estimation and performance evaluation methodologies.....</i>	43
2.10 <i>Standards and regulations</i>	45
3. Research and Development Methodology	47
3.1 <i>Methodology.....</i>	48
4. Design Optimization Methodology	51
<i>Nomenclature.....</i>	53

4.1	<i>Design optimization algorithm</i>	55
4.2	<i>Losses computation</i>	57
4.3	<i>PMSM torque-speed-efficiency map evaluation based on magneto static FEA model validation</i>	64
4.4	<i>PMSM torque-speed-efficiency map design and optimization validation</i>	67
4.5	<i>PMSM design optimization conclusions</i>	73
5.	Water Pumping design application	75
	<i>Nomenclature</i>	76
5.1	<i>Electrical machine topology selection</i>	78
5.2	<i>PMSM-WP design methodology with efficiency maps</i>	88
5.3	<i>PMSM Characteristics</i>	99
5.4	<i>PMSM validation by means of Time Dependent FEA Validation</i>	101
5.5	<i>Optimization Convergence and Computational Burden</i>	102
5.6	<i>PMSM design and optimization methodology. Conclusions</i>	103
6.	PMSM Parameter Estimation	104
	<i>Nomenclature</i>	106
6.1	<i>PMSM parameter estimation methodology overview</i>	108
6.2	<i>PMSM testing procedure</i>	108
6.3	<i>Parameter estimation algorithm to identify inductances and FOC strategy</i> .	114
6.4	<i>Parameter estimation results</i>	121
6.5	<i>Parameter estimation methodology conclusions</i>	128
7.	PMSM Performance Evaluation	129
	<i>Nomenclature</i>	130
7.1	<i>PMSM blocked rotor test and performance analysis methodology</i>	132
7.2	<i>Parameter estimation and performance evaluation results</i>	140
7.3	<i>PMSM performance evaluation from parameter estimation conclusions</i>	145
8.	Thesis Conclusions	146

9. Further Work	150
10. Thesis Scientific Dissemination.....	151
10.1 <i>Journal articles</i>	151
10.2 <i>Conference articles</i>	152
11. Bibliography	153
Appendix - Resources	168
A.1 <i>Software</i>	168
A.2 <i>Hardware</i>	168
A.3 <i>Measurement devices</i>	169
A.4 <i>Data acquisition devices</i>	173
A.5 <i>Voltage sources</i>	174
A.6 <i>Motor drives</i>	174
A.7 <i>Electrical machine test bench</i>	177
A.8 <i>APICOM Cento test bench</i>	178
A.9 <i>Parameter estimation and performance evaluation test bench</i>	179

Index of figures

Figure 1: Water pumping working system	5
Figure 2: Hydraulic curves. (a) Pump efficiency (η_{pump}) (b) Height pressure (H_{pump}) (c) Mechanical power required by the pump (P_{pump}) over volumetric flow rate	5
Figure 3: Water pump torque-speed operation area.....	6
Figure 4: Water pump experimental torque-speed-efficiency map.....	7
Figure 5: Example of area of interest selection and motor profile characteristics	7
Figure 6: From efficiency map to geometry. a) Desired efficiency map over specified torque-speed region b) Geometry representation.....	8
Figure 7: Prices (CNY) of Neodymium since 2013 to 2021, [8]	14
Figure 8: Mechanical constant over mechanical power per pole for p=1-6	17
Figure 9: Stator geometry definition	20
Figure 10: Rectangular element representation of the two dimensional reluctance grid where the numbers are nodes and the reluctances are defined as R_x and R_y	24
Figure 11: Mesh fluxes determination with magnetic vector potential example.....	25
Figure 12: Equivalent reluctance circuit example	26
Figure 13: Dirichlet's boundary condition along the outer stator diameter	30
Figure 14: Dirichlet's boundary condition in a symmetry sector	31
Figure 15: Neumann's boundary condition in a symmetry sector	31
Figure 16: d-q axis criteria for different synchronous machine configurations	33
Figure 17: IPMSM d-q axis representation with current space vector in motoring quadrant to perform the magneto-static computation	35
Figure 18: Magneto-static computation algorithm to obtain the flux linkage and torque over the current space vector angle and module.....	36
Figure 19: Electrical machine generalized optimization work flow	39
Figure 20: IE Energy efficiency classes curves for 6 pole at 50 Hz machines	46
Figure 21: Methodology for the development of the research work	48
Figure 22: PMSM design optimization algorithm	56
Figure 23: Magneto static computations algorithm	57
Figure 24: Magnetic flux density discrete distribution over the stator teeth and yoke regions (a). Toyota Prius 2004 magnetic flux density distribution at $i_d = -270$ A and $i_q = 270$ A (b).....	59
Figure 25: (d-q) electrical model representation	60
Figure 26: (d-q) electrical model algorithm to compute the torque-speed-efficiency map considering the control strategy	62

Figure 27: Pattern search optimization solver algorithm description.....	64
Figure 28: PMSM Toyota Prius 2004 experimental efficiency map (a). PMSM Toyota Prius 2004 magneto static model torque-speed-efficiency map.	65
Figure 29: PMSM Toyota Prius 2004 torque-speed-iron losses map, experimental (a) vs magneto static FEA model (b).....	67
Figure 30: PMSM Toyota Prius 2004 seed torque-speed-efficiency map (a) and design optimization geometry (b)	69
Figure 31: PMSM Toyota Camry 2007 torque-speed-efficiency map (a) Obtained through experimental data (b) Obtained using original geometry through time-dependent FEA model (c) Obtained through design optimization algorithm using magneto-static FEA model.....	71
Figure 32: <i>Patternsearch</i> optimization convergence (a) PMSM Toyota Prius 2004 (b) PMSM Toyota Camry 2007.....	72
Figure 33: Double layer winding layout candidates (a) 4 poles 6 slots, (b) 6 poles 9 slots, (c) 8 poles 9 slots, (d) 10 poles 9 slots and (e) 10 poles 12 slots [121].	80
Figure 34: 4 poles 6 slots machines star of slots for three phases	81
Figure 35: 6 poles 9 slots machines star of slots for three phases	82
Figure 36: 8 poles 9 slots machines star of slots for three phases	83
Figure 37: 10 poles 9 slots machines star of slots for three phases	84
Figure 38: 10 poles 12 slots machines star of slots for three phases	86
Figure 39: PMSM design methodology for WP applications using torque-speed-efficiency maps.....	89
Figure 40: Water pump experimental torque-speed-efficiency map.....	93
Figure 41: PMSM design optimization reference torque-speed-efficiency map	95
Figure 42: PMSM torque-speed-efficiency map with design optimization FEA model (a) and experimental test (b)	96
Figure 43: PMSM-WP FEA torque-speed-efficiency map (a) design optimization FEA model (b) experimental	97
Figure 44: (a) PMSM prototype assembly (b) PMSM-WP system (c) PMSM test bench	99
Figure 45: PMSM experimental setup for evaluating motor performance	101
Figure 46: (a) PMSM phase current at rated conditions experimental versus FEA (b) Torque at rated conditions experimental versus FEA.....	102
Figure 47: PMSM parameter estimation methodology overview.....	108
Figure 48: PMSM parameter estimation testing process	109
Figure 49: PMSM setup for parameter estimation	112

Figure 50: DAQ and transducer accuracy overlap.....	113
Figure 51: PMSM vector diagram of the fundamental magnitudes.	115
Figure 52: PMSM vector diagram including the harmonic vector representation.	115
Figure 53: PMSM current, voltage and flux linkage 1 st harmonic Blondel diagram	117
Figure 54: PMSM parameter estimation algorithm overview	120
Figure 55: ABB PMSM d-q Blondel current diagram, estimated versus experimental	121
Figure 56: GNC PMSM d-q Blondel diagram parameter estimation values of current	122
Figure 57: Experimental setup required to measure the reference inductances	123
Figure 58: L_d estimation versus reference method. (a) L_d versus i_d (b) L_d versus i_d ...	124
Figure 59: L_q estimation versus reference method. (a) L_q versus i_d (b) L_q versus i_d ...	124
Figure 60: L_d axis accuracy (A_{Ld}), (a) A_{Ld} versus i_d (b) A_{Ld} versus i_q	126
Figure 61: L_q axis accuracy (A_{Lq}), (a) A_{Lq} versus i_d (b) A_{Lq} versus i_q	127
Figure 62: PMSM blocked rotor test experimental setup and procedure algorithm....	132
Figure 63: Electrical models used to (a) identify the PMSM parameters and (b) to reproduce the PMSM performance	133
Figure 64: Instantaneous iron losses for parameter identification electrical model	135
Figure 65: Parameter identification algorithm to extract inductances and iron losses	137
Figure 66: PMSM performance reproduction algorithm using d-q electrical model	139
Figure 67: Iron losses estimation versus d-q currents and frequency.....	140
Figure 68: (a) Parameter estimation d flux linkage map versus d - q currents. (b) FEA d flux linkage map versus d - q currents. (c) Absolute error between FEA and experimental maps.....	142
Figure 69: (a) Parameter estimation q flux linkage map versus d - q currents. (b) FEA q flux linkage map versus d - q currents. (c) Absolute error between FEA and experimental maps.....	143
Figure 70: PMSM torque-speed-efficiency map (a) Parameter estimation performance evaluation, (b) FEA and (c) Experimental. (d) Absolute error between model and FEA maps.....	145
Figure 71: Dell Precision 7820 Workstation [126].....	168
Figure 72: CPU features [127]	169
Figure 73: Zimmer four channel power analyzer LMG450 [128].....	169
Figure 74: Tektronix A622 current probe [129].....	170
Figure 75: FLUKE i30s current clamp [131]	170
Figure 76: ABB VS750B voltage transducer [133].....	171
Figure 77: HBM T20WN torque transducer [134]	172
Figure 78: Thermocouple type K [135].....	172

Figure 79: DAQ NI PCI 6259 (a) [136] and NI SCB 68 (b) [137].....	173
Figure 80: NI USB-6353 DAQ [138]	174
Figure 81: SP300VAC600W [140].....	174
Figure 82: ABB DGV700 converter [141]	175
Figure 83: Brushless motor kit YROTATE-IT-RX23T [142].....	175
Figure 84: Electrical machine test bench.....	177
Figure 85: Apicom cento test bench (eddy current dynamometer)	178
Figure 86: Alternative parameter estimation experimental set up.....	179

Index of tables

Table 1: Allowable current densities for permanent magnets motors and cooling method	17
Table 2: Maximum magnetic flux density of synchronous machines	19
Table 3: Relation between electrical quantities and thermal quantities [29].....	26
Table 4: Rotating electrical machines standards and regulations	45
Table 5: Efficiency classes.....	46
Table 6: PMSM Toyota Prius 2004 torque-speed-efficiency.....	65
Table 7 PMSM Toyota Prius 2004 iron losses magneto static method vs time dependent FEA	66
Table 8: PMSM Toyota Prius 2004/Camry 2007 predesign parameters	68
Table 9: PMSM Toyota Prius 2004 geometric parameters comparison.....	68
Table 10: PMSM Toyota Prius 2004 experimental and design optimization magneto static efficiency map comparison.....	70
Table 11: PMSM Toyota Camry 2007 geometric parameters comparison.....	70
Table 12: Product requirements.....	78
Table 13: Efficiency requirements	78
Table 14: Fundamental winding factor for 4, 6, 8 and 10 poles / 6, 9 and 12 slots	79
Table 15: Star of slots properties for 4 poles and 6 slots.....	81
Table 16: MMF harmonic content of 4 poles 6 slots for double layer concentrated winding	81
Table 17: Star of slots properties for 6 poles and 9 slots.....	82
Table 18: MMF harmonic content of 6 poles 9 slots for double layer concentrated winding	82
Table 19: Star of slots properties for 8 poles and 9 slots.....	83
Table 20: MMF super harmonic content of 8 poles 9 slots for double layer concentrated winding	83
Table 21: MMF harmonic content of 8 poles 9 slots for double layer concentrated winding	84
Table 22: Star of slots properties for 10 poles and 9 slots.....	84
Table 23: MMF super harmonic content of 8 poles 9 slots for double layer concentrated winding	85
Table 24: MMF harmonic content of 8 poles 9 slots for double layer concentrated winding	85
Table 25: Star of slots properties for 10 poles and 12 slots.....	85

Table 26: MMF super harmonic content of 8 poles 12 slots for double layer concentrated winding	86
Table 27: MMF harmonic content of 8 poles 12 slots for double layer concentrated winding	86
Table 28: Design-optimization geometric parameters	91
Table 29: PMSM geometric rules	92
Table 30: Design optimization materials.....	93
Table 31: Design optimization fixed parameters.....	93
Table 32: Water pump efficiency map data labels.....	94
Table 33: Reference efficiency distribution levels.....	94
Table 34: PMSM torque-speed-efficiency map.....	96
Table 35: PMSM-WP system torque-speed efficiency map values comparison	98
Table 36: PMSM-WP efficiency labels comparison against reference map	98
Table 37: PMSM geometry values	99
Table 38: PMSM characteristics	100
Table 39: Measurement and acquisition devices details	110
Table 40: PMSM parameter estimation instrumentation.....	112
Table 41: Standard uncertainty considering the measurement devices.....	114
Table 42: ABB PMSM characteristic	121
Table 43: GNC PMSM characteristics.....	122
Table 44: Instrumentation used for reference inductance method.....	123
Table 45: Inductance and PM flux linkage parameters mean values comparison, parameter estimation method versus reference method	125
Table 46: Accuracy mean values for d-q inductances estimation	127
Table 47: ZES Zimmer power analyzer LMG450 characteristics.....	169
Table 48: Tektronix A622 current probe characteristics [130].....	170
Table 49: FLUKE i30s current clamp characteristics [132]	171
Table 50: ABB VS750B voltage transducer characteristics [133]	171
Table 51: HBM T20WN torque transducer characteristics.....	172
Table 52: Thermocouple type K characteristics [135].....	173
Table 53: DAQ NI PCI 6259 [136] and NI SCB 68 [137] characteristics	173
Table 54: DAQ NI-6353 [139].....	174
Table 55: SP300VAC600W Voltage Source specifications [140]	174
Table 56: ABB DGV700 converter characteristics [141]	175
Table 57: YROTATE-IT-RX23T characteristics.....	176

1. Introduction

This first chapter introduces the subject of research of this thesis. First, the research topic is introduced in section 1.1, exposing the market trends for water pumping applications and the electrical machines demands. Then, the working system is exposed in section 1.2. Subsequently, the hypotheses are postulated in section 1.3 providing the basis ideas from which the research and development of this thesis is oriented. Finally, and according to the hypotheses formulated, the objectives of this research are exposed in section 1.4, detailing the targets of the project.

Contents

1.1	Research topic
1.2	Working system
1.3	Hypotheses
1.4	Goals and objectives

1.1 Research topic

In the recent years due to the wide range of applications where water pumping is required, the operational concept of this system is evolving. For water pumping applications, so far, the induction motor has been the most implemented electrical machine, usually conceived to operate in a fixed operating point for constant pressure and volumetric flow demands. Nevertheless, nowadays hydraulic applications are increasingly requiring systems capable to operate efficiently in different conditions. Some of the most demanding applications within water pumping industry which require multiple operational conditions to the electrical machine are listed below.

- **Water pumping for domestic residential:**

Domestic residential applications require a non-constant pressure and volumetric flow demands. For instance, for water supply, the volumetric flow demands changes depending of the number of terminals (washing machine, dishwasher, water taps, toilet tank, etc.).

- **Water pumping for collective residential:**

For collective residential, for instance, in pressurization of potable water, the pressure may change as a function of multiple factors forcing to adapt the motor operation to guarantee a target pressure in each of the required sectors in real time.

- **Water pumping for swimming pools:**

For some swimming pool applications such as integrated fountains with variable demands or for recreational applications with non-constant supply.

- **Water pumping for agriculture:**

For some agriculture applications it is necessary to adapt the water supply for different irrigation sectors.

- **Water pumping for water treatment:**

The applications for water treatment deal with intermittent processes. During a water treatment cycle divided in different sub-processes, each of these sub-processes requires different pressure and volumetric flow demands. In addition, the viscosity and density of the untreated water is not constant.

- **Pumping for industry and construction sector:**

In industry applications, including the construction sector, there are fluids with different viscosities, variable densities and different pressure requirements.

Moreover, the industry trend for water pumping systems is to minimize the volume of all components, providing compact products for the same applications. All these aspects have opened a research field to implement new design and optimization methodologies for electrical

machines and specifically applied in water pumping systems. To contribute in this field, it is necessary to perform a deep analysis of the whole aspects involving the electric machine part.

Regarding the electric motor, there are different topology options to be implemented in several applications. The first topology and the most used during the 20th century has been the induction motor (IM), from single to three phase windings. The main advantages of these motors are their high reliability in adverse conditions, self-starting capability, the absence of control strategy and the low cost of the materials. The second topology introduced recently in the industry is the permanent magnet synchronous motor (PMSM). This topology includes diverse rotor configurations with different features, such as the surface permanent magnet synchronous motor (SPMSM), or the interior permanent magnet synchronous motor (IPMSM) which at the same time have different magnet layouts. The third topology is the synchronous reluctance machine (SRM). This machine has the advantage of being a rare earth magnet-free machine, therefore the cost is much lower than PMSMs. An interesting variation of this machine topology is the permanent magnet assisted synchronous reluctance machine (PMA-SynchRM). This variation includes permanent magnets but their key role is to improve some features of the SRM, such as the power factor and the torque density. Therefore, the permanent magnets can be hard ferrites, keeping the cost of the machine low.

Focusing on the tools available to design electrical machines, finite element analysis (FEA) has become the preferential tool, due to the high precision and the multiphysics capability. Nevertheless, one of the main drawbacks, is the computational burden, becoming incompatible for the everyday use, limiting its usability for industry projects where the available time to design an electric machine is long. For this reason, the research must consider the use of the most advanced design tools taking into account the feasibility in terms of time, computational resources and cost, becoming not only a functional but a practical tool to be used in industry applications.

Furthermore, from an industrial scope so far, the testing methodologies are focused on evaluating point by point the electrical machine performance, being a robust and trustable way to measure and validate the electrical machine characteristics. Nevertheless, this method requires a large time to prepare the experimental setup and to evaluate the whole motor performance. For this reason, there is a special interest on improving parameter estimation and performance evaluation techniques for electrical machines to reduce evaluation time, setup complexity and increase the number of physical magnitudes to measure in order to have deeper information. For this reason, the research should not be developed only to design and optimize electrical machines, but also

to provide procedures to analyze and validate the motor performance as a complement of the standard test methodology.

As a noteworthy point, so far the methodologies for designing and optimizing electrical machines consider only few aspects such the rated conditions with some size limitations. In addition, the optimization strategies have been based on single operation conditions, thus improving multiple aspects without considering the overall performance of the machine and its influence with the working system.

This research changes the design and optimization paradigm focusing on defining in advance the desired performance of the electrical machine in relation with the application system. The customization is not limited to an operating point but to the whole performance space, which in this case is the torque-speed area. Thus, the designer has plenty of freedom to study the system, define the desired motor performance establishing the size, thermal and mechanical limitations from the beginning of the process.

To summarize, this research work aims to develop a methodology to design and optimize electrical machines for hydraulic applications considering multiple operating points, being able to reduce volume and cost, using advanced design tools without avoiding functionality and practicability for industry applications. Moreover, the methodology must consider efficient techniques to validate experimentally the electric motor performance as a complement of the standard test procedure.

1.2 Working system

The working system is presented. It is mainly composed of three components, the motor drive (MD), the electrical machine (M) and the water pump (WP). Figure 1 exposes the working system including the power network (NW) either three or single phase line.

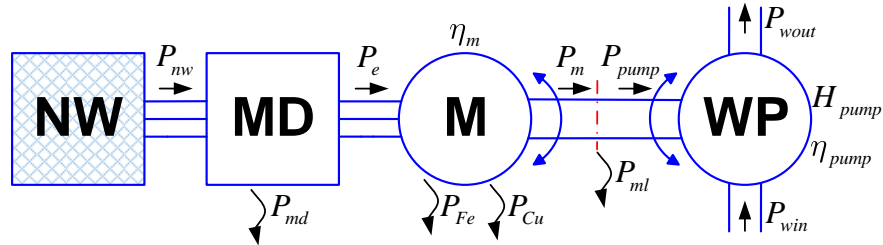


Figure 1: Water pumping working system

The water pump performance must be considered to give useful information about the electrical machine demands. To do so, as a first step, the hydraulic curves of the application are profiled, those are the hydraulic efficiency, pressure and required power over volumetric flow rate.

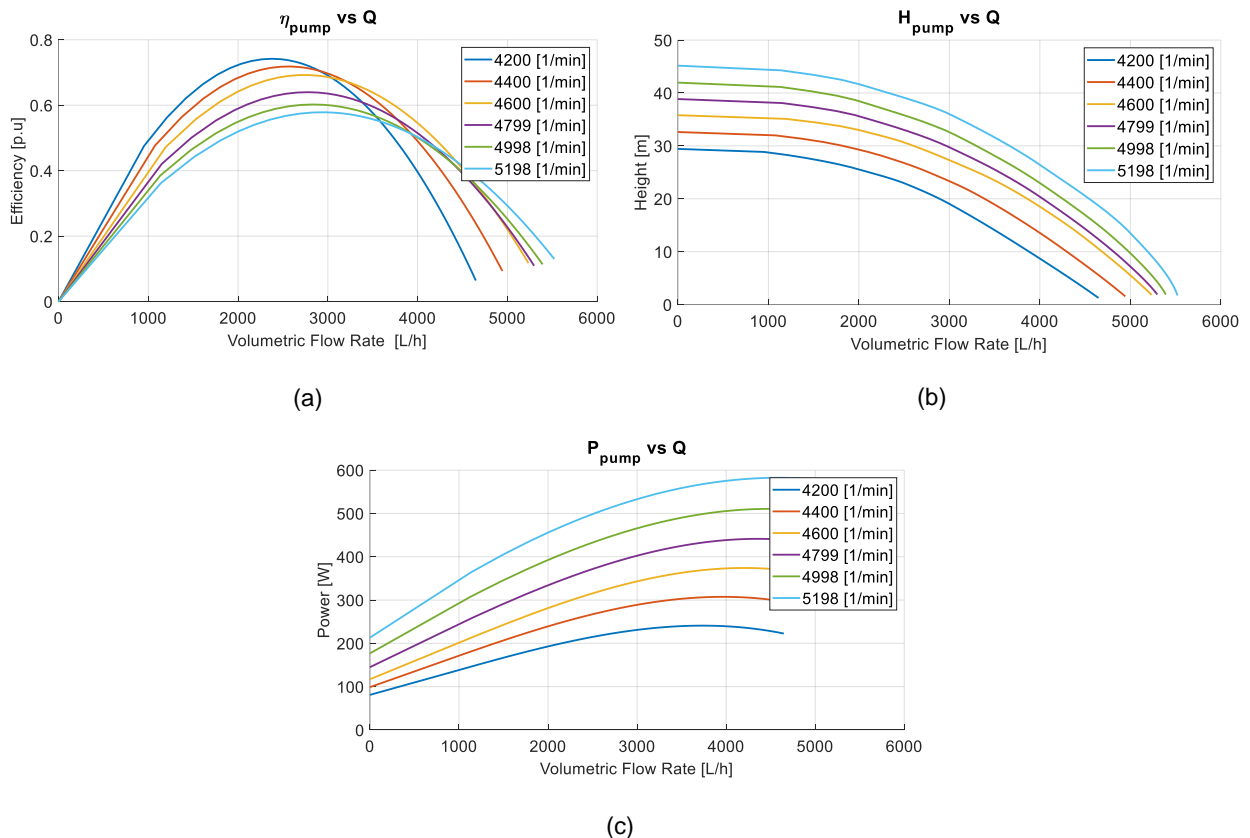


Figure 2: Hydraulic curves. (a) Pump efficiency (η_{pump}) (b) Height pressure (H_{pump}) (c) Mechanical power required by the pump (P_{pump}) over volumetric flow rare.

From the curves exposed in Figure 2, the motor requirements are calculated. Despite having the hydraulic curves, they are expressed as a function of the volumetric flow rate, which does not provide useful information about the motor requirements. To transform all available data to extract the motor demands some conversions are needed.

First, the torque demands expressed as a function of the volumetric flow rate are obtained from the mechanical power (P_{pump}).

$$T_{pump}(Q_{pump}, n) = \frac{P_{pump}(Q_{pump}, n)}{n} \quad (1)$$

Once the torque demands are calculated, for each angular speed the full torque range is known. Thus, along the rotational speed range, the torque area defining the working region of the electrical machine in torque-speed area is found.

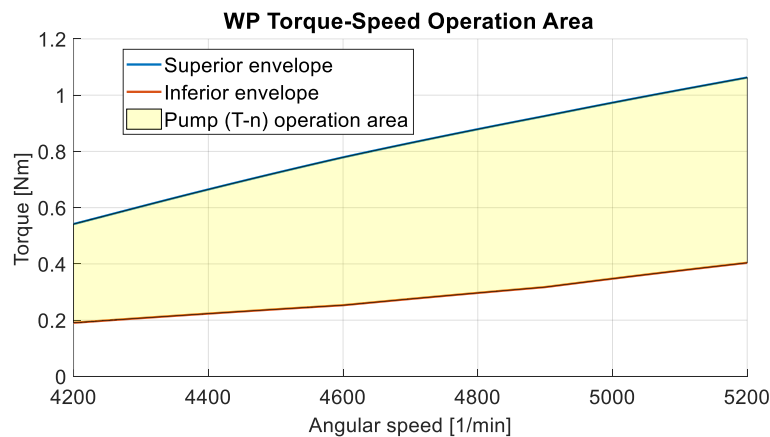


Figure 3: Water pump torque-speed operation area.

Figure 3 shows the water pump torque-speed operation area. The superior and inferior envelopes define, respectively, the maximum and minimum torques demanded by the water pump for every rotational speed.

For all operational points rearranged in the torque-speed plane, the hydraulic efficiency η_{pump} is available. Therefore, the hydraulic efficiency can be placed within the torque-speed map. This is named hydraulic torque-speed efficiency map as shown in Figure 4.

$$T_{pump}(Q_{pump}, n), \eta_{pump}(Q_{pump}, n) \rightarrow \eta_{pump}(n, T_{pump}) \quad (2)$$

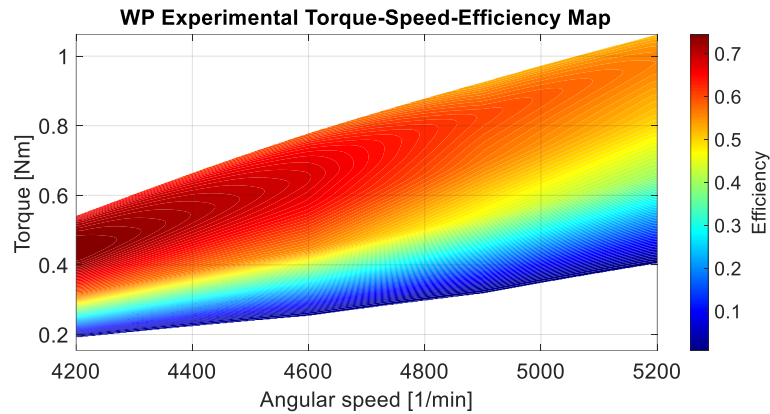


Figure 4: Water pump experimental torque-speed-efficiency map.

The experimental torque-speed-efficiency map of the water pump is the basis and starting point from which the hypotheses are formulated and, therefore, the starting point to develop the design optimization methodology. The objective is to locate the region of interest where the system is required to operate. Thus, the designer can customize the motor adapting its performance to the given region. Special interest is brought to the efficiency due the overall system is intended to be improved by defining the electrical motor performance.

For instance, Figure 5 shows a generic example where, starting from the experimental torque-speed-efficiency map of the water pump, the area of interest is selected. Multiple electrical machine envelopes can be defined, i.e., rated torque, rated speed, maximum speed, etc. The design strictly depends on the designer criterion.

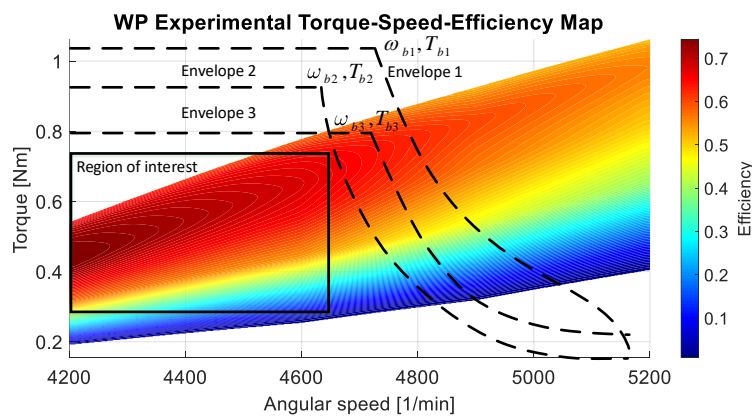


Figure 5: Example of area of interest selection and motor profile characteristics

1.3 Hypotheses

This section presents the hypotheses addressed for the research development. They are formulated to lay the foundation of the research and indicate the development field.

1.3.1 Hypothesis 1: Electric machine geometry from the efficiency map

Connecting with the example exposed in Figure 5, if the region of interest is selected and the electrical machine envelope is defined, the first hypothesis considers that **it is possible to define on first hand, within a region, the electrical machine torque-speed-efficiency map and through an algorithm to find a suitable unique geometry which accomplish these characteristics.**

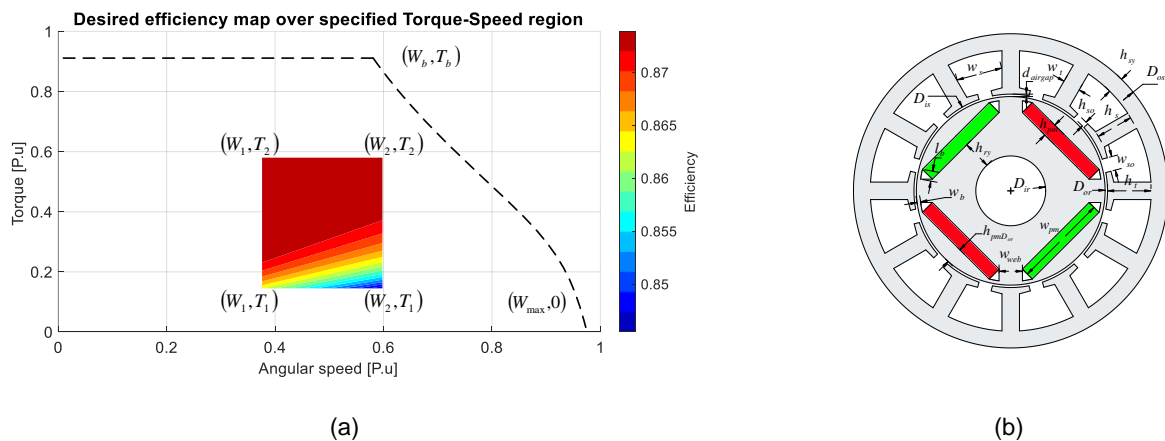


Figure 6: From efficiency map to geometry. a) Desired efficiency map over specified torque-speed region b) Geometry representation

The design optimization algorithm starts from the designer specifications, i.e., torque-speed envelope, region of interest and torque-speed efficiency map, and finishes with the electrical machine geometry accomplishing these requirements.

1.3.2 Hypothesis 2: Optimization with finite element analysis (FEA)

Computational resources are increasing with recent developments [1], and the modern optimization techniques allow the use of finite element methods to model electrical machines [2]. The third hypothesis considers, within the scope of this project, that **it is possible to implement an optimization algorithm for electrical machines using finite element analysis (FEA) with low computational burden.**

1.3.3 Hypothesis 3: Parameter estimation and performance evaluation methodology complementing standard test

As commented in the introduction of this thesis, the standard testing methodologies are focused on evaluating point by point the electrical machine performance, being a robust and trustable way to measure and validate the electrical machine characteristics. Nevertheless, this method requires a large time to prepare the experimental setup and to evaluate the whole motor performance. Thus the third hypothesis postulates that **it is possible to implement complementary algorithms and auxiliary test to expand the information of the electrical machine acquired from standard experimental test and reduce time when evaluating the motor performance.**

1.4 Goals and objectives

As stated the thesis aims change the design and optimization paradigm, focusing on defining beforehand the desired performance of the electrical machine in relation with the application system. Giving to the designer plenty of freedom to study the system, and define the desired motor performance establishing the size, thermal and mechanical limitations from the beginning of the process. Moreover, there is a special interest on improving parameter estimation and performance evaluation techniques for electrical machines to reduce evaluation time, setup complexity and increase the number of physical magnitudes to measure in order to have deeper information. Based on this explanation, this section exposes the main goals and objectives of the research project.

1. To develop a novel design and optimization algorithm focusing on defining beforehand the desired performance of the electrical machine in relation with the application system. The customization must include the whole performance space, which in this case is the torque-speed area.
2. To adapt the methodology specifically for water pumping applications. Thus, requiring a deep knowledge of the electrical machine demand.
3. To use finite element analysis (FEA) as a modelling technique. The model is aimed to be fast and precise in order to be used in optimization algorithms in affordable time. These desirable characteristics are of major importance in industry allowing to use the algorithm for different applications and perform multiple design changing the desired characteristics before prototyping stage.
4. To develop parameter estimation algorithm to complement the electrical machine measures using the standard experimental validation.
5. To develop a complementary test and algorithm which helps to evaluate the electrical machine performance. Thus providing a fast and efficient way to validate in second hand the motor performance reducing time and experimental complexity.
6. The electrical machine designed for the hydraulic application must accomplish with IE4 category from IEC 60034-30 efficiency standard.

2. State of the art

This chapter introduces the background of the research field analyzing the strengths and weaknesses of the different methodologies. Based on this analysis, the importance of proposing a new design and optimization approach is justified.

First of all, section 2.1 exposes the synchronous machine technology, showing the different topologies and explaining their differences. Section 2.2 describes the classical electromagnetic design by means of analytical equations. Section 2.3 details the improvement of the electromagnetic and thermal analysis with respect to the method exposed in section 2.2 by implementing reluctance and thermal networks, respectively. Section 2.4 Introduces another analytical methodology called anisotropic layer theory, which has provided good results within the design and optimization of electrical machines field. Section 2.5 introduces the methodologies to perform electromagnetic, thermal and mechanical analysis by using Finite Element Analysis (FEA). Section 2.6 describes the optimization methodologies. Sections 2.7 and 2.8 expose the recent developments of electrical machines design optimization methodologies including hydraulic applications. Finally, Section 2.9 exposes the state of art of testing, parameter estimation and performance analysis methodologies.

Contents

2.1	Synchronous machine technology
2.2	Classical electromagnetic design
2.3	Reluctance and thermal networks
2.4	Design based on anisotropic layer theory machine analytic model
2.5	Electromagnetic, thermal and mechanical finite element analysis
2.6	Electrical machines optimization methodologies
2.7	Recent developments in design optimization of PMSM
2.8	Recent developments in design optimization of electrical machines for hydraulic applications
2.9	Recent developments in parameter estimation and performance evaluation methodologies

2.1 Synchronous machine technology

This section reviews synchronous machine topologies and their evolution. Rotor wound synchronous machines are out of the scope of this study.

2.1.1 Permanent magnet synchronous machines (PMSM)

The concept of placing permanent magnets instead of coil excitation in synchronous machines predates the 20th century. The concept had to wait for developments in different related areas, such as in permanent magnet materials with more remanent flux density and higher coercive force to make them practicable. On the other hand, the control strategies had to develop in order to extract the high potentiality of these machines [3].

One of the first permanent magnet materials for electrical machines was magnetic cobalt steel. It was commercially available in 1920 having an energy product of 1 MGOe. Nevertheless, due its low coercivity, it could demagnetize during normal operation. A publication in 1925 [4] shows the earliest examples of permanent magnet machines using cobalt-steel.

Permanent magnet materials improved in posterior decades with the development of the family of Alnico magnets alloys. The energy product of these magnets occasionally reached 10 MGOe. These materials were developed between the 30's and 60's. Nevertheless, Alnico magnets still suffered from low coercivity. In order to overcome this inconvenient, the engineers designed a special pole shoe, to protect the magnets from demagnetizing magnetomotive force. These first prototypes, were constructed with line star squirrel cage, which represents the firsts hybridization of the asynchronous and permanent magnet synchronous machine [5].

Ferrite ceramic permanent magnets became practicable in 1960's, becoming a low cost alternative. The main inconvenient of these magnets is the low remanent flux density, typically 0.4 T. Nevertheless, due to the low cost and its resistance to corrosion, they are a good alternative in commercial applications. In 1976 Volkrodt [3] exposed a Siemens interior permanent magnet synchronous machine based on ferrite magnets and a spoke rotor, thus allowing to increase the air gap flux density amplitude.

The opportunity to extract reluctance torque from interior permanent magnet configurations in addition to the alignment torque became a subject of investigation in the earliest 70's. The hybrid nature of the torque can be expressed in terms of direct-quadrature axis as:

$$T = \frac{m}{2} \cdot p \cdot i_q \cdot (\psi_{PM} + (L_d - L_q) \cdot i_d) = \frac{m}{2} \cdot p \cdot i_q \cdot \psi_{PM} + \frac{m}{2} \cdot p \cdot i_q \cdot (L_d - L_q) \cdot i_d \quad [N \cdot m] \quad (3)$$

T is the instantaneous torque produced by the machine, p is the number of pole pairs, Ψ_{pm} is the permanent magnet flux linkage, i_d and i_q are the currents in direct and quadrature axis respectively and L_d and L_q are the inductances in the same axis reference. The first term, which includes the permanent magnet flux linkage, is the so called alignment torque or magnet torque. The second term, including the difference of direct and quadrature axis inductances is called reluctance torque. Analyzing the given equation, can be deduced that increasing the difference between direct and quadrature axis inductance increases the reluctance torque component.

The incoming availability during the 1970's of high strength magnets or also called rare earth magnets beginning with the Samarium-Cobalt (SmCo) and later in 1980's the Neodymium-Iron-Boron (NdFeB), made it possible to reach high values of torque and power density. Magnet manufacturers, mainly located in China, worked to decrease the cost of Neodymium magnets during the 1990's. That opened the commercial availability of this material to construct electrical machines for different applications.

2.1.1.1 Surface permanent magnet synchronous machines (SPMSM or SMPMSM)

This rotor topology introduces the first type of permanent magnet machine. The permanent magnets are placed in the outer part of the rotor (SPMSM or SMPMSM). This machine is a non-salient pole machine, i.e., the inductances in direct and quadrature axis can be considered equal. This particular feature has direct consequences on the control operation.

This arrangement results in a higher air gap flux density because the magnet is facing directly to the air-gap without any interruption [6]. Nevertheless, they have lower structural integrity and mechanical robustness, making it feasible only for low speed applications if the rotor is large enough. Moreover, the construction, in some cases, requires bounding protection in order to avoid the magnets to be untapped from the rotor.

2.1.1.2 Interior Permanent Magnet Synchronous Machines (IPMSM)

The Interior or Inset Permanent Magnet Synchronous Machine (IPMSM) has the magnets placed within the rotor structure. There are several different magnet layout configurations within this family, such as the spoke topology or the V-shape, among others.

Mechanically, this machine is robust, being practicable for high speed applications. Due to its geometrical disposition, the direct and quadrature axis inductances are different, generally the quadrature axis inductance is higher than the direct axis inductance by a maximum ratio of three. This characteristic allows the extraction of reluctance torque, which adds up to the alignment torque. Thus, this machine allows a high torque density with less magnet volume.

2.1.1.3 Neodymium price volatility

The commercialization of Neodymium and in particular in form of NdFeB for permanent magnets, since 1980s, has had a huge effect for the PMSM development. The price of NdFeB magnets was high during the first years of commercialization. China had the main role in lowering the market price due its very large reserves of rare-earth materials in comparison with other countries, being the dominant NdFeB magnet manufacturer in the world.

Figure 7 shows the price (CNY) of Neodymium since 2013 to 2021. It can be seen a decreasing trend from 2013 to 2017 which contributed positively into PMSM development, especially in electric vehicles sector. After that, the prices have increased with two historical peaks. The first peak of September of 2017 doubling the price of the beginning of the year and reaching values never seen since 2012. After this peak, the Neodymium price has been very unstable since the most recent raise experienced during March of 2021, where a price of 892463 CNY was reached mainly due the accident of EVER GIVEN in the Suez Canal [7].



Figure 7: Prices (CNY) of Neodymium since 2013 to 2021, [8]

This price volatility, mainly generalized for all the rare-earth materials, must be considered putting special attention when designing permanent magnet machines, due the economical aspect is of major importance to save material cost.

2.1.1.4 PMSM market

Three different PMSM family series have been selected to show an insight of the industry.

Yaskawa® PMSMs SS7-series eco family [9] cover power ranges between 2.2 kW and 300 kW. The rated speeds are 1150 rpm, 1450 rpm and 1750 rpm. The energy efficiency classes include IE3 and IE4. The motors include resolver position transducer together with speed drive.

Bongfiglioli® BMD PMSM family [10] have a huge variety from 150 W to 30 kW. The torque range covers from 0.85 to 45 Nm, and the nominal rotational speed lies between 1600 rpm and 6000 rpm.

VEM® PMSMs [11] have a huge variety for different applications. For instance, for energy saving applications there are the PE1R/PE0R families covering power ranges from 0.09 to 75 kW with 4, 6 and 8 poles. The speed ranges are between 750 to 3000 rpm with torques between 0.6 Nm and 860 Nm. On the other hand, for synchronous high power motors there are the P21R/P20R family. The power ranges include from 0.25 to 75 kW with 4, 6, 8 and 12 pole design from 500 to 3000 rpm including torque ranges from 0.55 Nm to 700 Nm. Finally, for high torque application requirements there are the P2.F and P2.B family ranges covering powers from 12 to 471 kW, with speed ranges from 200 to 600 rpm. The torques are between 573 Nm to 7500 Nm. All the motors of these families have 12 pole extensions.

2.1.2 Synchronous reluctance machines (Synch-RM)

Synchronous reluctance machines (Synch-RM) base their operation mainly on the production of reluctance torque due the high saliency ratio. The basic concepts and theory of this machine was studied by Blondel in 1913 [12]. Commercial interest in the implementation of synchronous reluctance machines grew in the decades of 60's and 70's, especially for variable speed applications.

Regarding the efficiency and power factor, in the early 20's, Kotsko [13] reported low values of these characteristics, unless the machines were designed to have a high saliency ratio. Then, it was introduced a rotor structure divided into multiple sections, helping the flux to circulate in one direction (d axis) while avoiding the circulation in the perpendicular axis (q axis). The concept of this machine has evolved into sophisticated configurations in order to increase as much as possible the rotor saliency, increasing the efficiency and power factor capabilities.

2.1.2.1 Synch-RM market

Nowadays, synchronous reluctance machines and drives are commercialized by different companies. For instance, ABB group offers a product portfolio from 1.1 to 350 kW of output power. Some of them fulfill the IE4 efficiency standard [14].

2.1.3 Permanent magnet assisted synchronous reluctance machine PMASynch-RM

The current trend during the last decade is to minimize the use of rare earth magnets as much as possible, due the price volatility and geographical economic factors. For this reason, the commercial trend, especially in the area of electrical vehicles propulsion, is innovating with the Permanent Magnet Assisted Synchronous Reluctance Machine. This machine is considered as a reluctance machine because the main torque production is due to the reluctance torque, nevertheless as the name indicates, it includes magnets. These magnets are placed basically to improve the power factor and to produce a minimum alignment torque assisting the principal reluctance component.

Due the nature of torque production of these machines, it is possible to use hard ferrites magnets, thus keeping a competitive cost, being feasible for a huge range of applications in industry.

2.1.3.1 PMASynch-RM market

Nowadays permanent magnet assisted synchronous reluctance machines have low popularity in the market, nevertheless, Nidec® group have a huge catalogue [15] of this electrical machine family, covering powers from 11 kW to 200 kW for 1500 and 3000 rpm.

2.2 Classical electromagnetic design

Electrical machines design is a highly nonlinear problem. Thus, it is necessary an advanced design tool to represent accurately the electromagnetic and thermal behaviors. All these design tools have been introduced recently in industry, but since the 20th century, the design procedure was performed by means of analytical equations, general rules and experimental factors acquired by the experience of the engineers [16].

This section exposes the basic concepts of the classical electromagnetic design, beginning with some initial constraints and assumptions. Next, the rotor sizing criteria is exposed, the calculation of the stator phase turns, the sizing of the magnet thickness using Ampere's Law and placing the suitable stator sizes to work near the magnetic saturation point.

2.2.1 Winding characteristics

For winding it is important to determine the type, i.e., distributed or concentrated, aspects as the maximum filling factor and the maximum current density depending of the cooling method, etc. A practicable filling factor is between 0.4 and 0.6 [p.u], this value mainly depending on the manufacturing methodology.

$$K_u = 0.4 \sim 0.6 \quad (4)$$

The current density for synchronous machines considering the cooling method is summarized in Table 1 [17], [18].

Table 1: Allowable current densities for permanent magnets motors and cooling method

	Direct air cooling	Direct water cooling
Current Density J [A/mm ²]	4-7.5	10-28

2.2.2 Mechanical load capacity

The mechanical load capacity or commonly known as mechanical loadability [17] is a constant that expresses the maximum mechanical power per unit of volume without causing any deformation in the rotor structure. The value of this constant depends on the number of poles and mechanical power, as shown in Figure 8.

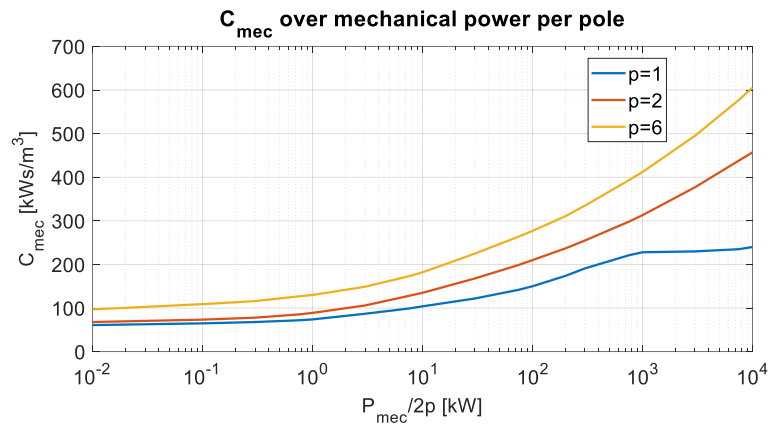


Figure 8: Mechanical constant over mechanical power per pole for p=1-6

2.2.3 Geometric aspect ratios

When sizing the electrical machine, some geometrical ratios are defined. Two main aspect ratios are presented.

- **Inner to outer stator diameter ratio:**
Typically, for PMSMs this ratio is between 0.45-0.6. This magnitude depends of the application.
- **Length to outer rotor diameter ratio:**
The length to outer rotor diameter ratio is defined considering the angular speed of the rotor, because it can create bending modes. Typically, for synchronous machines with more than one pole pair this ratio is calculated as:

$$\chi_{L/D_{or}} = \frac{\pi}{4 \cdot p} \cdot \sqrt{p} \quad (5)$$

On the other hand, for a pole pair machines this ratio is typically between 1-3.

2.2.4 Air gap length

The air gap length selection is of major importance. It influences the eddy losses caused by the tooth apertures when rotating, as well as, to the surface losses in the rotor created by the current linkage of the stator winding. Thus, a large air gap reduces the rotor losses by using the low pass filter effect of the air gap. On the other hand, if a small air gap is selected, the magnet cost is reduced in case of PMSMs because less volume is needed, or in IM it reduces the copper losses but increasing the iron losses.

Some empirical formulas [17] have been developed to design the air gap length as a function of the mechanical power. Nevertheless, no optimum value has been found in any case. Thus, the air gap length has to be calculated and optimized for each application.

$$\delta = \frac{0.2 + 0.01 \cdot P^{0.4}}{1000} [m], \text{ when } p = 1 \quad (6)$$

$$\delta = \frac{0.18 + 0.006 \cdot P^{0.4}}{1000} [m], \text{ when } p > 1 \quad (7)$$

2.2.5 Magnetic flux densities

In order to attain maximum power per volume in an electrical machine, it is necessary to work within the iron saturation region. However, the motor efficiency decreases due the increment of iron losses. Typically, the design flux densities are:

- **Stator teeth:**
For the stator teeth a maximum flux density between 1.6 and 2 Tesla is recommended. This value oscillates depending of the tooth dimensions. When increasing the slot area, it is necessary to increase the tooth flux density to allow a feasible space for the winding regions. Other aspects must be considered, such as the number of turns, current density, efficiency, etc.
- **Stator yoke:**
For the stator yoke lower saturation is recommended easing the heat transfer in radial direction. The typical values are between 1.1 and 1.6 Tesla.
- **Rotor yoke:**

Rotor yoke is designed below the saturation region. The objective is to reduce as much as possible the amount of rotor material without increasing the magnetic path reluctance. The typical values for this region are in between 1.0 and 1.5 Tesla.

- **Air gap:**

The air gap flux density peak is designed in correlation with the tooth peak value. To guarantee a suitable relation between the maximum peak induction of the teeth and air gap, respectively, the typical values are in between 0.8 and 1.0 Tesla.

All the magnetic flux density peaks are summarized in Table 2.

Table 2: Maximum magnetic flux density of synchronous machines

Flux density peak [T]	
Stator teeth	1.6-2.0
Stator yoke	1.1-1.6
Rotor yoke	1.0-1.5
Air gap	0.8-1.0

2.2.6 Back electromotive force

To calculate the number of stator turns, the back electromotive force at rated speed is calculated considering the power factor, typically the back electromotive force is guessed between 90-95% of the voltage source [19].

$$E_{pm} = 0.9 \sim 0.95 U_{ph} \quad [V] \quad (8)$$

2.2.7 Rotor sizing

To size the outer rotor diameter, the mechanical load capacity is used. Thus, when the rotor aspect ratio is selected [17], the air gap diameter is calculated. This diameter is set equal to the outer rotor diameter to keep the simplicity.

$$D_{airgap} = D_{or} = \sqrt[3]{\frac{P_{mec}}{C_{mec} \cdot \chi_{L/D_{or}} \cdot \frac{f}{p}}} \quad [m] \quad (9)$$

2.2.8 Stator phase turns

The stator phase turns are calculated considering back electromotive force, air-gap flux density and fundamental frequency. Thus, using the Faraday's induction law, the phase turns can be calculated as:

$$E_{pm} \cdot \sqrt{2} = N_{ph} \cdot (2 \cdot \pi \cdot f) \cdot k_{w1} \cdot \left(\frac{2}{\pi} \cdot \hat{B}_{d1} \cdot L_{eff} \cdot \tau_p \right) \quad [V] \quad (10)$$

$$N_{ph} = \frac{E_{pm} \cdot \sqrt{2}}{4 \cdot f \cdot k_{w1} \cdot \hat{B}_{d1} \cdot L_{eff} \cdot \tau_p} \quad (11)$$

If the permanent magnet magnetization profile is non-sinusoidal, the fundamental harmonic component must be used.

2.2.9 Stator geometry

Previously, the magnetic flux densities in different electrical machine parts have been defined. Therefore, by applying Gauss's law, the cross-sectional area of each stator part can be calculated, thus obtaining a basic sizing. On the other hand, considering the stator phase turns, the number of conductors per slot, the current density and the filling factor, the slot area can be calculated.

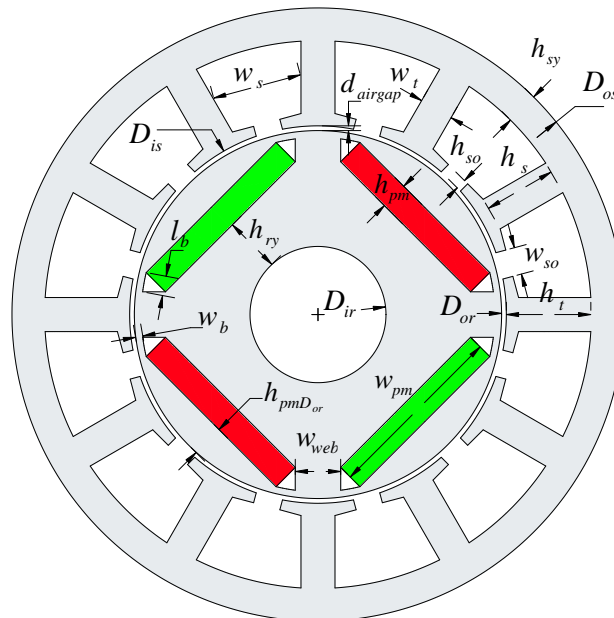


Figure 9: Stator geometry definition

To obtain the yoke height, the magnetic flux densities through the air gap and the stator yoke are required,

$$h_{sy} = \frac{\alpha_{pm} \cdot \hat{B}_d \cdot \tau_p \cdot L_{eff}}{2 \cdot k_s \cdot L \cdot \hat{B}_{sy}} \quad m \quad (12)$$

Being k_s the stacking factor, τ_p the pole pitch, L_{eff} the effective air gap length, L the stack length and α_{pm} the magnet coverage.

To take into account the fringing effect, the effective length of the cross-sectional area is determined by the following relation,

$$L_{eff} = L + 2 \cdot \delta \quad m \quad (13)$$

Being δ the air gap height and L the stack length.

Next, the tooth width is obtained following the same law.

$$w_t = \frac{\hat{B}_d \cdot \tau_s \cdot L_{eff}}{k_s \cdot L \cdot \hat{B}_t} \quad m \quad (14)$$

τ_p being the slot pitch.

The slot width is assigned as the remaining part of the slot pitch.

$$w_s = \tau_s - w_t \quad m \quad (15)$$

Once the slot width is obtained, the next step is to determine the suitable slot height to allocate the wires.

$$h_s = \frac{z_q \cdot \frac{I_s}{J}}{k_u \cdot (w_s - w_{so})} \quad [m] \quad \text{being } q < 1 \quad \text{and double layer} \quad (16)$$

$$h_s = \frac{z_q \cdot \frac{I_s}{J}}{k_u \cdot w_s} \quad [m] \quad \text{being } q \geq 1 \quad (17)$$

The tooth height is assumed to be equal to the slot height plus the height of the tooth aperture.

$$h_t = h_s + h_{ta} = h_s + h_{so} \quad [m] \quad (18)$$

h_{so} being the slot aperture height, and h_{ta} the tooth aperture height. They are assumed to be equal.

Finally, once the tooth and stator yoke heights are known, it is possible to find the outer stator diameter.

$$D_{os} = D_{is} + 2 \cdot h_t + 2 \cdot h_{sy} \quad [m] \quad (19)$$

When dealing with concentrated and double layer winding types, the winding process requires some free area so that the winding needle can pass.

2.2.10 Magnet Thickness

When designing PMSMs, the magnet thickness is calculated by applying Ampere's law.

- **Air gap magnetic voltage:**

$$\hat{U}_d = \left(\frac{\hat{B}_{d1}}{\mu_0} \right) \cdot \delta \cdot k_c \cdot A \quad (20)$$

- **Stator yoke magnetic voltage:**

$$\hat{U}_{sy} = \hat{H}_{sy} \cdot \frac{\pi \cdot D_{os} - h_{sy}}{2 \cdot p} \cdot A \quad (21)$$

- **Stator tooth magnetic voltage:**

$$\hat{U}_t = \hat{H}_t \cdot h_t \cdot A \quad (22)$$

- **Rotor yoke magnetic voltage:**

$$\hat{U}_{ry} = \hat{H}_{ry} \cdot \frac{\pi \cdot D_{or} - h_{ry}}{2 \cdot p} \cdot A \quad (23)$$

Being k_c the Carter's coefficient.

Once the magnetic voltages are calculated, it is possible to calculate the permanent magnet height. First the ratio between the outer rotor surface and the magnet's surface is calculated.

$$R_{pm} = \frac{\tau_p \cdot \alpha_{pm}}{w_{pm}} \quad (24)$$

In case of being a surface mounted permanent magnet synchronous motor (SPMSM), the area of the magnet and the outer rotor surface are equivalent, and thus, $R_{pm} = 1$.

Once calculated the surface ratio, the magnet height can be calculated using half of the magnetic circuit path. Depending of the rotor configuration can be defined in two different ways.

- **Surface mounted or interior permanent magnet:**

$$h_{pm} = \frac{\hat{U}_d + \hat{U}_t + \frac{\hat{U}_{sy}}{2} + \frac{\hat{U}_{ry}}{2}}{\frac{\hat{B}_{pm} - \hat{B}_d \cdot R_{pm}}{\mu_{pm} \cdot \mu_0}} \cdot m \quad (25)$$

- **Spoke:**

$$h_{pm} = \frac{\hat{U}_d + \hat{U}_t + \hat{U}_{sy} + \hat{U}_{ry}}{\frac{\hat{B}_{pm} - \hat{B}_d \cdot R_{pm}}{\mu_{pm} \cdot \mu_0}} \cdot m \quad (26)$$

2.3 Reluctance and thermal networks

2.3.1 Reluctance networks

The reluctance networks method (RNM) [20] [21], is mainly based on Ohm's Law in combination with Kirchhoff's Laws applied to magnetic circuits.

$$U_i = Re_i \cdot \varphi_i \quad (27)$$

U_i , Re_i and φ_i being the magnetic voltage, reluctance and magnetic flux respectively of the component i respectively.

Kirchhoff's law for the magnetic flux in a node is as follows,

$$\sum_{i=1}^n \varphi_i = 0 \quad (28)$$

Kirchhoff's law for the magnetic voltages of the meshes is as,

$$\sum_{i=1}^n U_i = 0 \quad (29)$$

This method is one of the oldest for modelling magnetic circuits in electrical machines and transformers. When the complexity of the system increases, it is required to develop extensive multimode reluctance networks systems. Moreover, taking into account the non-linearity of the ferromagnetic materials leads to a complex reluctance definition. One of the main advantages is the low computational burden.

The RNM was first used by Janusz Turowski in 1960 [21] for two dimensional modelling of three phase transformers. The same author in 1969 [22] introduced the reluctance network model to be applied in three dimensional cases. Some other authors contributed to the theory of RNMs, as Davey and King [23] and Carpenter [24], Djurovic and Moson [25].

Some recent studies have implemented the reluctance networks to design and optimize electrical machines. For instance, López [26] uses reluctance networks to perform a range optimization of a synchronous reluctance motor and permanent magnet assisted synchronous reluctance machine taking into account the driving cycle. Raminosa [27] presents a nonlinear reluctance network approach to compute the electromotive force waveforms of a synchronous reluctance machine. Asfirane [28] uses a mesh of reluctance network to evaluate the performance of linear permanent magnet machines.

2.3.1.1 Reluctance networks derived from finite differences

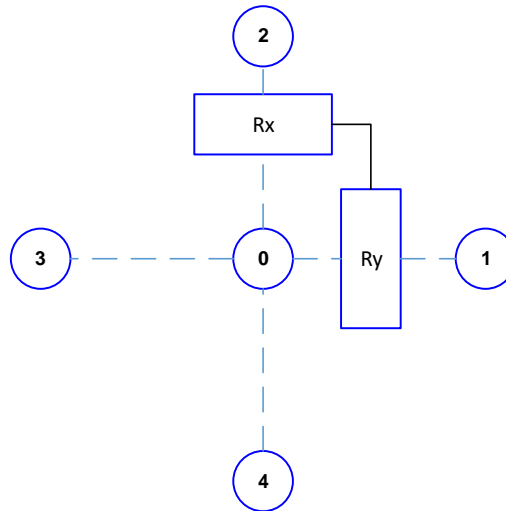


Figure 10: Rectangular element representation of the two dimensional reluctance grid where the numbers are nodes and the reluctances are defined as R_x and R_y

Reluctance networks definition around *node 0* where its magnetic vector potential is known as A_0 comes from Poisson equation for magnetic vector potential A in 2D Cartesian coordinates in regions including current sources is as,

$$\frac{\partial^2 A}{\partial x^2} + \frac{\partial^2 A}{\partial y^2} = -\mu \cdot J \quad (30)$$

The previous equation can be extended into difference equation by expressing it into Taylor series for x and y . (31) expresses the magnetic vector potential values of nodes 1 and 3 respectively.

$$A_1 = A(x+h) = A(x) + \frac{h}{1!} \cdot A'(x) + \frac{h^2}{2!} \cdot A''(x) + \dots \quad (31)$$

$$A_3 = A(x-h) = A(x) - \frac{h}{1!} \cdot A'(x) + \frac{h^2}{2!} \cdot A''(x) - \dots$$

Adding both sides of the equal and assuming the term $A(x) = A_0$.

$$\frac{\partial^2 A(x,y)}{\partial x^2} \approx \frac{1}{h^2} \cdot (A_1 + A_3 - 2 \cdot A_0) \quad (32)$$

$$\frac{\partial^2 A(x,y)}{\partial y^2} \approx \frac{1}{a^2} \cdot (A_2 + A_4 - 2 \cdot A_0) \quad (33)$$

Therefore,

$$\frac{A_1 - A_0}{h^2} + \frac{A_3 - A_0}{h^2} + \frac{A_2 - A_0}{a^2} + \frac{A_4 - A_0}{a^2} = -\mu \cdot J \quad (34)$$

Adding the terms, $a \cdot h / \mu$ and reluctances per linear meter as,

$$\begin{aligned} R_x &= \frac{h}{\mu \cdot a} \\ R_y &= \frac{a}{\mu \cdot h} \end{aligned} \quad (35)$$

It is obtained,

$$A_1 - A_0 \cdot R_y + A_3 - A_0 \cdot R_y + A_2 - A_0 \cdot R_x + A_4 - A_0 \cdot R_x = -I_0 \quad (36)$$

Being I_0 the total current in a single mesh.

Recalling the relations,

$$\Phi_i = \iint_{s_i} B_i \cdot ds_i = \oint A_i \cdot dl_i \quad (37)$$

For a rectangular mesh as represents the next figure,

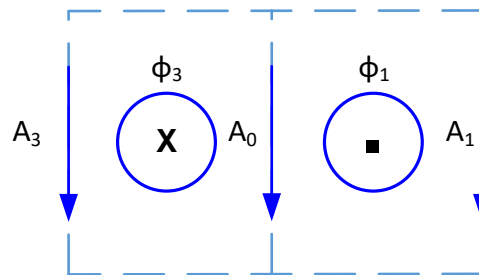


Figure 11: Mesh fluxes determination with magnetic vector potential example

Therefore, the flux crossing along magnetic vector potential 3 and 0 is determined by the expression,

$$\Phi_3 = A_0 - A_3 \quad (38)$$

The equivalent reluctance networks are as,

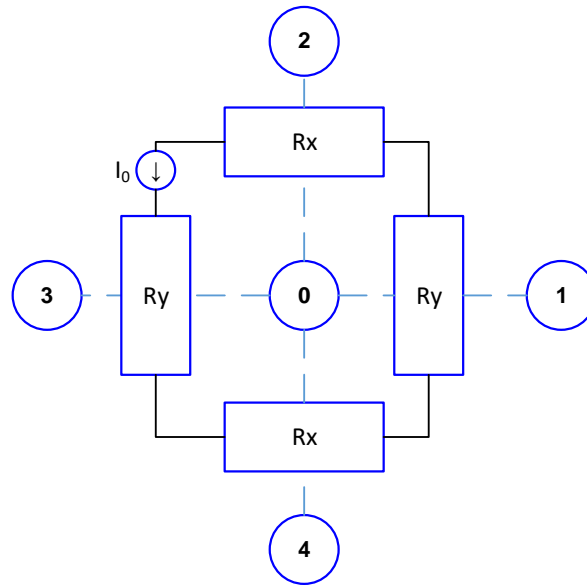


Figure 12: Equivalent reluctance circuit example

Obtaining Kirchhoff and Ohm equations for magnetic circuits,

$$\Phi_1 \cdot R_y + \Phi_3 \cdot R_y + \Phi_2 \cdot R_x + \Phi_4 \cdot R_x = I_0 \quad (39)$$

Giving a system of n current sources and m reluctances for each circuit the matrix expression is as,

$$\begin{bmatrix} I_0 \\ \dots \\ I_{m-1} \\ I_m \end{bmatrix} = \begin{bmatrix} R_{00} & \dots & R_{0n-1} & R_{0n} \\ \dots & \dots & \dots & \dots \\ R_{m-1} & \dots & R_{m-1n-1} & R_{m-1n} \\ R_{m0} & \dots & R_{mn-1} & R_{mn} \end{bmatrix} \begin{bmatrix} \phi_0 \\ \dots \\ \phi_{n-1} \\ \phi_n \end{bmatrix} \quad (40)$$

2.3.2 Thermal networks

The method of thermal networks is analogous to the reluctance networks method. The analogous relationships are listed in the following table.

Table 3: Relation between electrical quantities and thermal quantities [29]

Electrical Quantities			Thermal Quantities		
Potential	V	[V]	Temperature	θ	[oK]
Current	I	[A]	Heat	Q	[W]
Current density	J	[A/m ²]	Heat flux	q	[W/m ²]
Conductivity	σ	[S/m]	Thermal conductivity	λ	[W/m·K]
Resistance	R	[Ω]	Absolute thermal resistance	R_{th}	[K/W]
Resistivity	ρ	[Ω /m]	Thermal resistivity	ρ_{th}	[m·K/W]
Capacitance	C	[F]	Thermal capacitance	C_{th}	[J/oK]

In this way a thermal problem can be solved as an electrical circuit problem. The thermal conductance in solids across a homogeneous object can be calculated taking into account its thermal conductivity by:

$$G_{th} = \frac{\lambda \cdot A}{L} = \frac{1}{R_{th}} \quad (41)$$

A being the cross sectional area where the heat flow is passing through.

On the other hand, for gases and fluids, it is necessary to represent not only the conductance, but also the convective heat dissipation.

The thermal resistance due to the convection can be calculated as,

$$R_{th} = \frac{1}{\alpha \cdot A} \quad (42)$$

Being α the convection heat transfer coefficient [$\text{W}/\text{m}^2 \cdot \text{K}$]. The calculus of this constant can be extracted from the experimental relation:

$$\alpha = \frac{\lambda_{air} \cdot Nu}{2 \cdot L} \quad (43)$$

Being Nu the Nusselt number which describes the ratio of convective to conductive heat transfer perpendicular to the boundary of study.

2.4 Design based on anisotropic layer theory machine analytic model

In 1954 Mishkin [30] developed for the first time the anisotropic layer theory machine analytic model for induction machines derived directly from Maxwell equations. The model is simplified considering rectangular coordinates. Posterior studies applied the anisotropic layer theory for linear machines [31] or other machine topologies [32], [33].

2.4.1 Magnetic vector potential theory

To obtain the magnetic vector potential, a cylindrical coordinate system is used [34]. The magnetic flux density B_n and magnetic field strength H_n have its components along the φ and θ axis. Considering the previous magnitudes, the magnetic vector potential for one material is as,

$$A_n \varphi, \theta, t = \hat{A}_n \varphi \cdot e^{j \cdot \omega_e t - p \cdot \theta} \cdot u_z \quad (44)$$

The current density associated with the layer is as,

$$J_n = \nabla \times \left[\bar{\mu}_n^{-1} \cdot \nabla \times A_n \right] = \sigma_n \cdot E_n + v_n \times B_n + J_{en} \quad (45)$$

the permeability tensor being defined as,

$$\bar{\mu}_n = \begin{bmatrix} \mu_{\varphi n} & 0 \\ 0 & \mu_{\theta n} \end{bmatrix} \quad (46)$$

E_n being the electric field, v_n the mechanical speed of the layer of analysis, and σ_n the electrical conductivity of the layer.

2.4.2 Layer model

Assuming the electrical conductivity of the layer null, the medium equation for the magnetic vector potential is as,

$$\frac{\partial^2}{\partial \varphi^2} \cdot \hat{A}_n \varphi + \frac{1}{\varphi} \cdot \frac{\partial}{\partial \varphi} \cdot \hat{A}_n \varphi - \frac{\alpha_n^2}{p^2} \cdot \hat{A}_n \varphi = -\hat{J}_{en} \quad (47)$$

the external current density J_{en} is calculated as,

$$J_{en \varphi, \theta, t} = \hat{J}_{en} \varphi \cdot e^{j \cdot \omega_e t - p \cdot \theta} \cdot u_z \quad (48)$$

where,

$$\alpha_n^2 = \frac{\mu_{\theta n}}{\mu_{\varphi n}} \cdot p^2 \quad (49)$$

2.4.3 Non-conductive layer, no excitation

For a non-conductive layer with no excitation $J_{en} = 0$.

$$\frac{\partial^2}{\partial \varphi^2} \cdot \hat{A}_n \varphi + \frac{1}{\varphi} \cdot \frac{\partial}{\partial \varphi} \cdot \hat{A}_n \varphi - \frac{\alpha_n^2}{p^2} \cdot \hat{A}_n \varphi = 0 \quad (50)$$

Then, based on the layer to model, specific equations can be derived. Solving the previous equation,

$$\hat{A}_n \varphi = a_n \cdot \varphi^{\alpha_n} + b_n \cdot \varphi^{-\alpha_n} \quad (51)$$

Being the magnetic flux density the curl of the magnetic vector potential, $\hat{B}_n = \nabla \times \hat{A}_n$.

$$\hat{B}_{\varphi n} \varphi = -\frac{j \cdot p}{\varphi} \cdot \left[a_n \cdot \varphi^{\alpha_n} + b_n \cdot \varphi^{-\alpha_n} \right] \quad (52)$$

$$\hat{B}_{\theta n} \varphi = -\frac{\alpha_n}{\varphi} \cdot [a_n \cdot \varphi^{\alpha_n} - b_n \cdot \varphi^{-\alpha_n}] \quad (53)$$

2.4.4 Non-conductive layer, imposed current

For a non-conductive layer with excitation $J_{en} \neq 0$. Therefore,

$$\hat{A}_n \varphi = a_n \cdot \varphi^{\alpha_n} + b_n \cdot \varphi^{-\alpha_n} + \hat{G}_n \cdot \varphi^2 \quad (54)$$

$$\hat{G}_n = -\hat{J}_{en} \cdot \frac{\mu_{\varphi n} \cdot \mu_{\theta n}}{4 \cdot \mu_{\varphi n} - p^2 \cdot \mu_{\theta n}} \quad (55)$$

The magnetic flux density components are,

$$\hat{B}_{\varphi n} \varphi = -\frac{j \cdot p}{\varphi} \cdot [a_n \cdot \varphi^{\alpha_n} + b_n \cdot \varphi^{-\alpha_n} + \hat{G}_n \cdot \varphi^2] \quad (56)$$

$$\hat{B}_{\theta n} \varphi = -\frac{\alpha_n}{\varphi} \cdot \left[a_n \cdot \varphi^{\alpha_n} - b_n \cdot \varphi^{-\alpha_n} + \frac{2}{\alpha_n} \cdot \hat{G}_n \cdot \varphi^2 \right] \quad (57)$$

2.5 Electromagnetic, thermal and mechanical finite element analysis

For general physics problems, the description of the governing laws are expressed by means of partial differential equations (PDEs) [35]. Generally, these equations cannot be solved analytically when considering a specific geometry and boundary conditions. Thus, a discretization method is used to solve the PDEs by means of numerical equations.

- **Electromagnetic field:**

To determine the electromagnetic field within electrical machines, the finite element method solves the Maxwell's equations with additional laws and boundary conditions to determine the interaction of electromagnetic fields with media.

- **Thermal field:**

For the thermal field it is considered the heat produced by the Joule effect in the wires and the heat produced by the hysteresis and eddy currents.

- **Structural mechanics:**

The deformations, stresses and strains are calculated in the region of study, so that rotor integrity and the deformation of the stator teeth are analyzed.

2.5.1 Electromagnetic analysis of electrical machines with magneto-static computations

This subsection develops the general features when studying the electromagnetic field in electrical machines by means of magneto-static computations [36], [37].

2.5.2 Reduction to a 2D problem

Three-dimensional FEM analysis requires extensive computer resources, which is time-consuming. For this reason, the problem is usually reduced to two-dimensional case, using the machine symmetry along the longitudinal axis. Thus, the magnetic fields along the z-axis (longitudinal axis) are assumed identical. The effect of the ending edges is considered or modelled via lumped parameters [38].

2.5.3 Boundary conditions

Proper boundary conditions leads into a simplification of the case [39], [37]. There are mainly three different boundary conditions.

- **Dirichlet's boundary condition:**

The value assigned to the boundary is assumed to be constant, resulting as a magnetic insulator. Therefore, no flux lines cross the boundary.

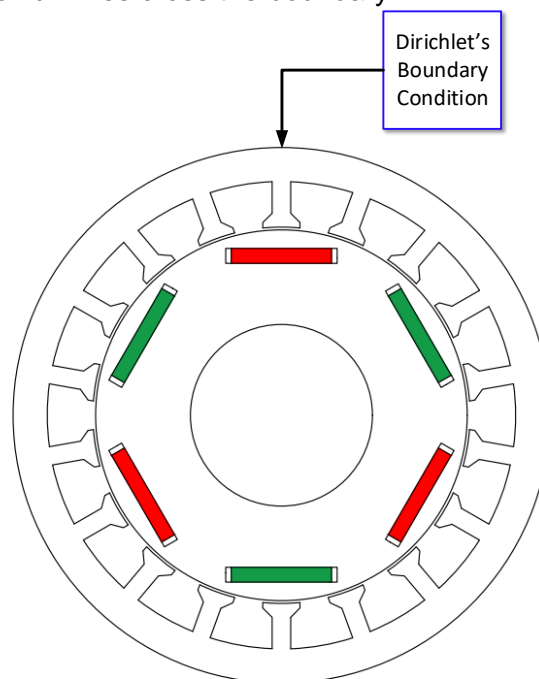


Figure 13: Dirichlet's boundary condition along the outer stator diameter

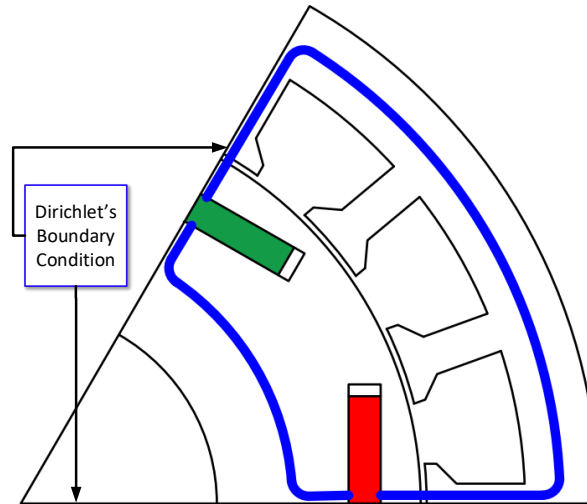


Figure 14: Dirichlet's boundary condition in a symmetry sector

- **Neumann's boundary condition:**

This condition imposes a continuity across the boundary. Thus, the partial derivative of the magnetic field perpendicular to the boundary is zero. The flux lines are forced to be perpendicular to the boundary line.

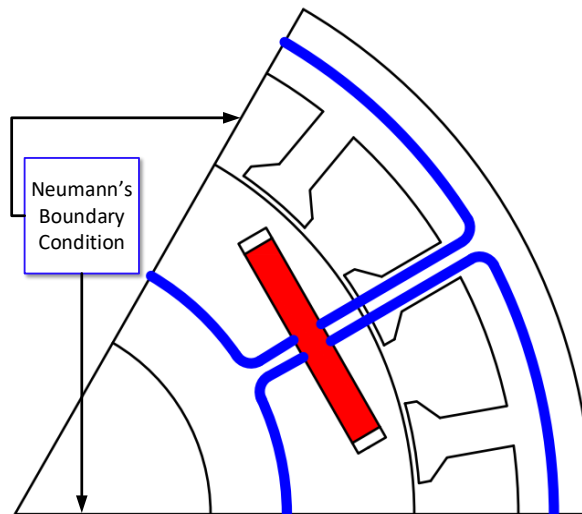


Figure 15: Neumann's boundary condition in a symmetry sector

- **Periodic conditions:**

When studying electrical machines, the magnetic field paths are repeated along the full circumference of the geometry. The number of repetitions depends on the machine periodicity, which is defined as the greater common divisor between the number of slots and the number of pole pairs.

$$t = G.C.D. Q, p \quad (58)$$

The case presented in Figure 13 has 6 poles and 18 slots. So, the periodicity is 3. Thus, it is necessary to represent at least three slots in one symmetry sector.

When only one pole is represented within the sector symmetry, it is called odd symmetry. Nevertheless, when the sector symmetry includes a pole pair, the sector symmetry is called pair. For example, when having 9 slots and 3 pole pairs. The periodicity is 3 slots, but in this case, these 3 slots include a pole pair, thus in this case the periodicity is pair.

2.5.4 Permanent magnet flux linkage

The flux linkage is defined as the flux passing through a phase winding multiplied by the number of effective turns of the winding. The permanent magnet flux linkage is obtained under no load conditions. So, it does not consider the flux created by the coil excitation. On one hand, the most important value to be obtained is the peak value of the flux linkage, which is obtained when the permanent magnet is aligned with the phase of study. Nevertheless, the flux linkage as a function of the rotor position is useful to find the back-electromotive force profile.

2.5.5 Back electromotive force

The computation of the back electromotive force can be obtained from a static simulation when the flux linkage profile over the rotor position is known [37]. Then, the instantaneous back electromotive force is defined as the product of the angular velocity and the flux linkage.

2.5.6 Computation of the direct axis inductance

The direct axis inductance is defined as the flux linkage divided by the current in the d axis. In permanent magnet synchronous motors (PMSM) this axis is aligned with the magnetic flux of the magnets. Nevertheless, in synchronous reluctance machines (Synch-RM) and permanent magnet assisted reluctance machines (PMASynch-RM) the main flux is produced by the stator excitation, thus the d axis is set in the minimum reluctance path, being the electrical orthogonal axis to the permanent magnet cavity [40].

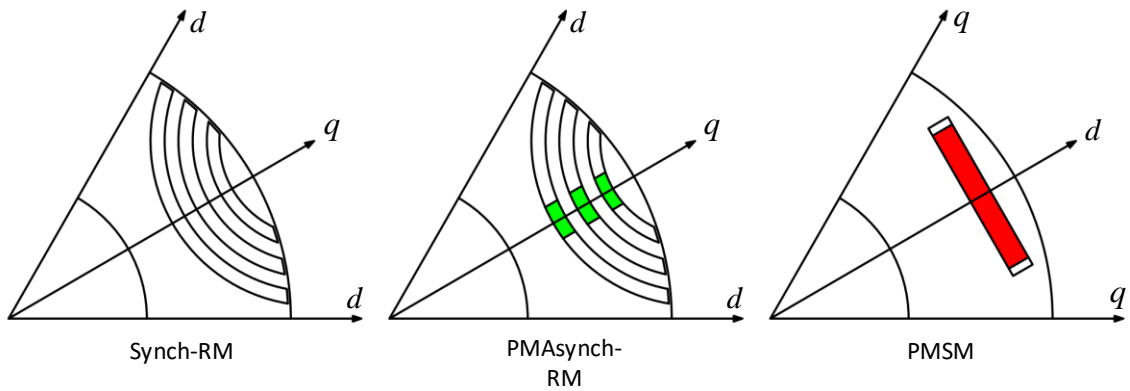


Figure 16: d-q axis criteria for different synchronous machine configurations

The rotor d axis is aligned with the reference coil, or coil a . Then, the current space vector is pointed towards the direct axis:

$$\begin{cases} i_d = i_s \\ i_q = 0 \end{cases} \quad (59)$$

Assuming a three phase system, the inverse Park transformation is as,

$$\begin{bmatrix} i_a \\ i_b \\ i_c \end{bmatrix} = \frac{2}{m} \begin{bmatrix} \cos \alpha & -\sin \alpha \\ \cos\left(\alpha - \frac{2\cdot\pi}{3}\right) & -\sin\left(\alpha - \frac{2\cdot\pi}{3}\right) \\ \cos\left(\alpha + \frac{2\cdot\pi}{3}\right) & -\sin\left(\alpha + \frac{2\cdot\pi}{3}\right) \end{bmatrix} \begin{bmatrix} i_d \\ i_q \end{bmatrix} \quad (60)$$

Therefore, assuming the phase a aligned with the d axis:

$$\begin{cases} i_a = \frac{2}{m} \cdot i_s \\ i_b = -\frac{1}{m} \cdot i_s \\ i_c = -\frac{1}{m} \cdot i_s \end{cases} \quad (61)$$

From FEM results the d -axis inductance can be obtained as,

$$L_d i_d = \frac{\psi_d - \psi_{pm}}{i_d} H \quad (62)$$

Being ψ_d the total flux linkage in phase a , and ψ_{pm} the total flux linkage of the permanent magnet.

In the case a Synch-RM or PMASynch-RM configurations, the inductance can be calculated as,

$$L_d i_d = \frac{\psi_d}{i_d} H \quad (63)$$

Equation (63) considers no permanent magnet flux contribution along the d -axis.

2.5.7 Computation of the quadrature axis inductance

The quadrature axis inductance is calculated following the same strategy as explained in direct axis. For this study the current space vector is aligned with the q axis. Since the rotor position convention remains constant, the current values are changed as,

$$\begin{cases} i_a = 0 \\ i_b = \frac{\sqrt{3}}{m} \cdot i_s \\ i_c = -\frac{\sqrt{3}}{m} \cdot i_s \end{cases} \quad (64)$$

If a PMSM is considered, the permanent magnet flux is not linked in this axis. Therefore:

$$L_q i_q = \frac{\psi_q}{i_q} H \quad (65)$$

When considering a PMASynch-RM, the flux of the permanent magnets contributes to the stator flux linkage. Therefore, it is necessary to subtract the contribution of the permanent magnets.

$$L_q i_q = \frac{\psi_q - \psi_{pm}}{i_q} H \quad (66)$$

2.5.8 Computation of d - q inductances considering cross-coupling effect

In 2.5.6 and 2.5.7, the d - q axis were decoupled. However, in real applications the direct and quadrature axis inductances are not independent [40]. This is called cross-coupling effect [41], [42], which is due to the magnetic saturation. Thus, when injecting current in the d axis, the quadrature inductance is affected, and vice versa. Therefore:

$$\begin{cases} L_d = L_d i_d \cdot i_q \\ L_q = L_q i_d \cdot i_q \end{cases} \quad (67)$$

In order to have enough information about this effect, a multi-static FEM analysis is proposed. The objective is to change gradually the space vector angle from the d axis to the q axis.

For PMSMs, the motoring operation is placed in the second quadrant. For PMASynch-RM and Synch-RM the motoring operation is placed in the first quadrant. For the sake of simplicity, the algorithm is explained for the PMSM case.

Figure 17 shows a simplified case for PMSMs showing the working quadrant and a current space vector.

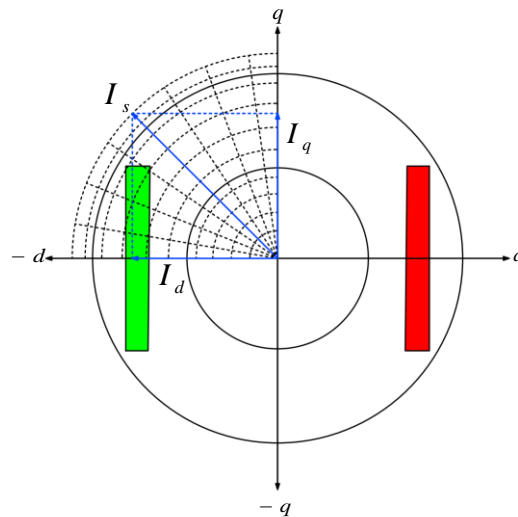


Figure 17: IPMSM d-q axis representation with current space vector in motoring quadrant to perform the magneto-static computation

First, the d axis of the rotor, where the PM flux is pointing outwards radially, is aligned with the reference phase, usually called phase a . Then, the current space vector is injected towards the negative d axis and the magneto-static FEA simulation is performed. This same process is repeated for different amplitudes and angles of the current space vector within the motoring quadrant.

To decompose the linkage flux in d - q axis, the Park's transform is applied.

$$\begin{bmatrix} \psi_d \\ \psi_q \end{bmatrix} = \frac{m}{2} \begin{bmatrix} \cos \alpha & \cos\left(\alpha - \frac{2 \cdot \pi}{3}\right) & \cos\left(\alpha - \frac{4 \cdot \pi}{3}\right) \\ -\sin \alpha & -\sin\left(\alpha - \frac{2 \cdot \pi}{3}\right) & -\sin\left(\alpha - \frac{4 \cdot \pi}{3}\right) \end{bmatrix} \begin{bmatrix} \psi_a \\ \psi_b \\ \psi_c \end{bmatrix} \quad (68)$$

Figure 18 shows the Magneto-static computation algorithm to obtain the flux linkage and torque over the current space vector angle and module.

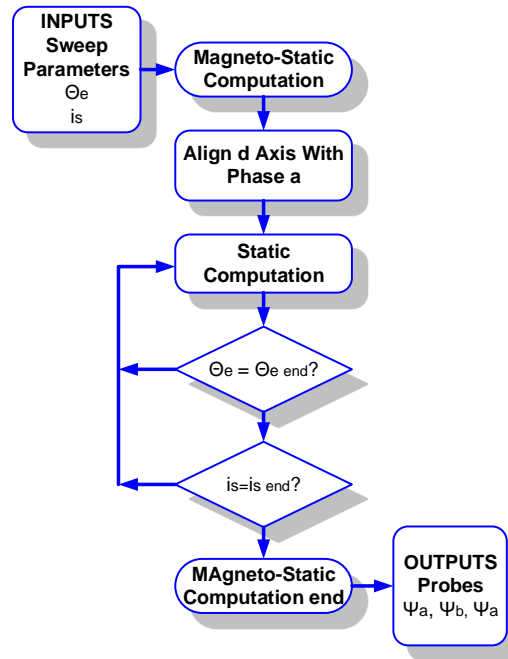


Figure 18: Magneto-static computation algorithm to obtain the flux linkage and torque over the current space vector angle and module

2.5.9 Torque computation

Torque computation by means of finite element analysis can be done in different ways [43]. The most used method is called Maxwell's stress tensor. Nevertheless, some other methods can be used, as the Coulomb's virtual work principle, magnetic co-energy derivation method, magnetizing current method, or Arkkio, method among others.

- **Maxwell stress tensor:**

Maxwell stress tensor is defined as,

$$T_{elec} = L \cdot \int_s \vec{r} \wedge \left\{ \frac{1}{\pi_0} \cdot \vec{B} \cdot \vec{n} \cdot \vec{B} - \left(\frac{1}{2 \cdot \pi_0} \right) \cdot \vec{B}^2 \cdot \vec{n} \right\} \cdot ds \quad (69)$$

where L is the air-gap length, B the magnetic flux density, r the air-gap radius and \vec{n} the normal direction of the surface integration.

- **Coulomb's virtual work principle:**

This method computes the integration of virtual work over the finite elements between the fixed part and the moving part. The deformation of the moving part is understood as the work of a force acting through this boundary. The integral expression is expressed as,

$$T_{elec} = \int_{\Omega} L \cdot \left[-B_t \cdot \bar{G}^{-1} \cdot \left(\frac{d\bar{G}}{d\phi} \right) \cdot H + \int_0^H B \cdot dH \cdot |\bar{G}|^{-1} \cdot \left(\frac{d \cdot |\bar{G}|}{d\phi} \right) \right] \cdot d\Omega \quad (70)$$

The integration is performed in the finite elements adjacent to the moving boundary. G is the Jacobian matrix of the mesh's deformation, and $\left(\frac{d \cdot |\bar{G}|}{d\phi} \right)$ denotes the variation of

deformation for a certain displacement.

- **Magnetic co-energy derivation method:**

When keeping the current constant, the torque can be calculated by deriving the magnetic co-energy W' .

$$T_{elec} = L \cdot \frac{dW'}{d\theta_r} = \frac{d \int_{\Omega} \vec{B} \cdot d\vec{H} \cdot d\Omega}{d\theta_r} \quad (71)$$

The torque is calculated numerically from the difference of two adjacent co-energies, thus resulting the following expression:

$$T_{elec} = L \cdot \frac{W'_{\theta_r + \Delta\theta_r} - W'_{\theta_r}}{\Delta\theta_r} \quad (72)$$

- **Magnetizing current method:**

This method calculates the magnetizing current and magnetic flux density over the finite element edges of the ferromagnetic materials and the air. The mathematical expression is as,

$$T_{elec} = \left(\frac{L}{\pi_0} \right) \cdot \int_s \vec{r} \wedge (B_{t1}^2 - B_{t2}^2) \cdot \vec{n} - B_{t1} \cdot B_{t2} - B_{n2}^2 \cdot \vec{t} \cdot ds \quad (73)$$

B_{t1} and B_{t2} are the tangential components of magnetic flux density in the ferromagnetic and air domains respectively, B_{n2} is the normal induction of the air-gap domain.

- **Arkkio's method:**

Arkkio's method integrates the torque given by the Maxwell's stress tensor in the air-gap volume.

$$T_{elec} = \left(\frac{L}{\pi_0 \cdot (r_s - r_r)} \right) \cdot \int_s \vec{r} \cdot B_r \cdot B_t \cdot ds \quad (74)$$

Where B_t and B_r are the tangential and radial components of magnetic flux density. On the other hand, r_s and r_r are the internal and external radius of the air-gap.

2.6 Electrical machines optimization methodologies

The optimization methodologies for electrical machines have become important due to the increasing interest to boost energy efficiency for different engineering applications [2]. Nevertheless, due to the high nonlinearity and the number of parameters required, it leads to a very complex problem when optimization is desired. The recent algorithms developed for nonlinear optimization problems have opened a new design opportunity in the field of study [44].

Most of the electrical machine models are based on finite element methods, thus avoiding to apply analytical equations. However, FEA is time-consuming, so some advanced optimization algorithms are needed to reduce the optimization time.

This subsection exposes different optimization methodologies used for electrical machines. First the general optimization workflow is exposed [45].

2.6.1 Electrical machine optimization work flow

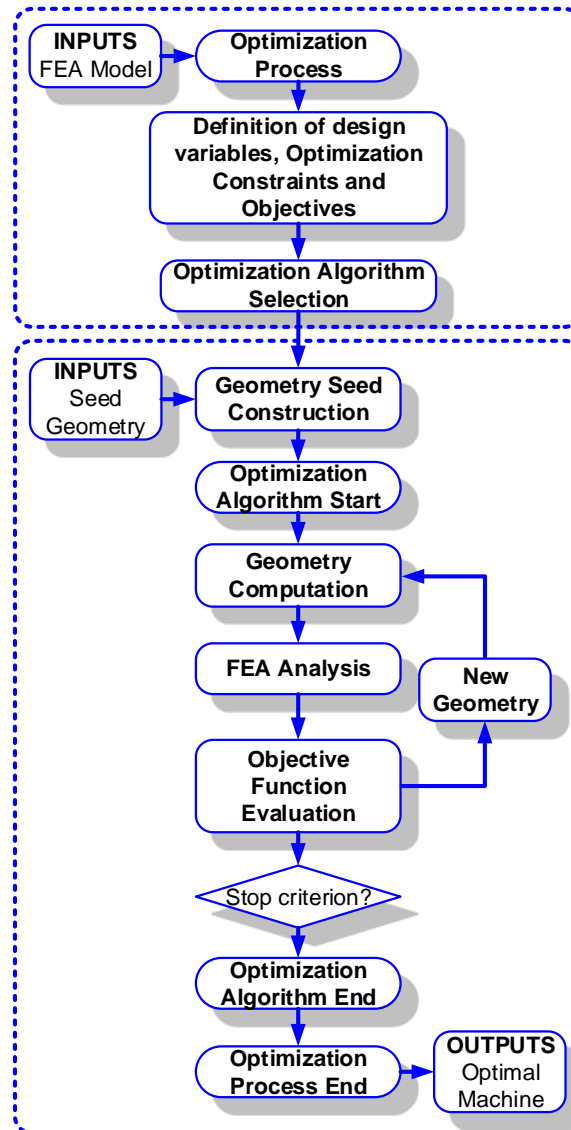


Figure 19: Electrical machine generalized optimization work flow

2.6.2 Genetic Algorithms

Genetic algorithms (GA) create a set of electrical machines population represented by chromosomes [46]. The solutions from the first population, also called parent population, are evaluated and used to create the second generation of electrical machines. The new generation is created by means of evolutive techniques such as crossover, mutation and selection. From the parent population, the best individuals are selected to transfer their genetic information to the following generation, and so on. The algorithm repeats the process until reaching the target machine.

One of the features which makes GA algorithm suitable, is its capabilities to optimally find the global minima and avoiding local minima solutions [47]. However, from a computational point of view, GA is not considered efficient [48].

2.6.3 Differential evolution

Differential evolution algorithms (DE) [49] have been the most widely used optimization methods for electrical machines optimization. The algorithm methodology works similar to GA. The first population is randomly created for the given constraints. The candidates are created following the techniques explained in GA algorithm, crossover and mutation. Nevertheless, DE always maintains the best candidate, even if it is from a past generation, and thus, after a certain amount of iterations, DE finds the best candidate.

2.6.4 Particle swarm optimization

Particle swarm optimization algorithm (PSO) is an evolutionary population algorithm. Nevertheless, the search criteria is based on the behavior of bird flocks searching for food [2]. PSO starts with an initial population, commonly called particles. Each particle has an intrinsic number of parameters. The group of particles are called compound swarm. The swarm starts searching for the best solution in the multidimensional parameter dimension, with a random search direction and without specified gradient. The swarm, then, starts to move within the searching space evaluating the fitness function. The particles move toward the best solution by regulating the speed, based in its own experience and searching information with other particles. Thus, in every iteration the particles update the current solutions and then, the swarm searches for the next steps, gathering the information and pointing the swarm towards the best solution.

2.6.5 Surrogate models, multi-level and hybrid methods

As commented before, FEA models require huge computational resources. In order to solve this inconvenient some techniques have been developed. The first approach are based on approximate models to solve the optimization problem [50]. The approximation models can be established as surrogate models for FEA or through lumped parameters circuits. Other techniques are based on using design of experiments (DoE) and statistical methods [51].

The most used surrogate models applied in electrical machines design are the response surface method (RS) [52] [53], which explores the relationship between the independent variables and the response or predicted variable. The main objective of RS is to first analyze a sequence of experiments derived from a (DoE) in order to obtain the optimal response of the system. On the

other hand, the second method is the Kriging model [46] which represents in terms of a model the relation between the design variables and the output function. Some recent studies use Kriging model-based optimization. Taran [54] uses Kriging models for electrical machines to achieve the optimum solution with three dimensional FEA optimization. Zhu [52] used a similar methodology for multi-objective optimization of a magnetic planetary geared permanent magnet brushless machine.

Other alternative to surrogate models is the so-called multi-level optimization. This strategy is based on subdividing the design variables in many subsets, thus, the most sensitive variables are analyzed independently for a better search [55].

2.7 Recent developments in design optimization of PMSM

Electrical machine design and optimization fields, with the research evolution are demanding algorithms faster and reliable for industry applications. PMSMs have been the preferential choice due to their features [17], [37]. Some earlier studies coupled the design and optimization algorithms with FEA. The aim was to maximize the electrical machine efficiency according to the driving cycle of an electrical vehicle [56]. However, FEA requires high computational resources, which forced the authors of [56] to perform the optimization in a reduce number of geometric parameters. Overcoming this drawback, posterior studies [57] used magneto-static FEA with lumped circuit modeling. References [26], [58] applied static analysis with reluctance networks. Nevertheless iron losses calculation in [26], [57], [58] do not consider the harmonic content of the electromagnetic variables, leading into considerable errors at high frequencies.

By applying FEA jointly with magneto-static analysis using space-time transformation [59] allows transforming spatial quantities into the time domain. Further studies in this field applied space-time transformation into design-optimization algorithms for electrical machines. For instance, [60] applied this method to analyze the driving cycle performance of a PMSM for traction application. Other studies focused on different electrical machine topologies. For example [61] optimized a brushless doubly-fed induction machine. In [62] a computationally-efficient FEA (CE-FEA) approach based on pseudo rotating position (PRS) is presented. This improvement allows comparing the performance of different optimization techniques. Further research works applied these concepts for designing and optimizing electrical machines by considering the rated conditions [63]. For instance, [64] uses the methodology to improve the rated output power without increasing the material cost. Other researches analyze a reduced number of operating points, knowing the driving cycle [65], whereas [57], [66] limited the number of variables to be optimized.

Focusing on related fields, there are researches focused on optimizing the efficiency distribution on a limited operating area. For example, [67] developed a design optimization algorithm combining FEA and mesh adaptive direct search (MADS), attaining maximum efficiency in maximum consumption areas for heavy duty electric vehicles (HD-EV). Similarly, reference [68] applies a multi-criteria design and optimization methodology to a PMSM considering the driving cycle using some efficiency points.

Other studies avoid using FEA applying supervised machine learning [69]. As a main drawback these methods are limited to a specific machine topology, while increasing the complexity using analytical models to perform electromagnetic [70] or thermal analyses [71].

2.8 Recent developments in design optimization of electrical machines for hydraulic applications

Water pump applications are progressively demanding reduction of size in order to achieve compact designs and, at the same time, the capability of operating with multiple load conditions [72]. Within the pump system, focusing on the motoring part, and considering the aspects mentioned in previous sections, PMSMs have become the most suitable choice to achieve these characteristics, due to their superior capabilities [17], [37].

Regarding the motor topologies used in water pumping, earlier studies compare the performance using PMSMs to actuate submersible pumps instead of IMs [73], concluding that power savings of around 20% are feasible. Posterior works show the feasibility of feeding autonomous solar powered water pumping systems with PMSMs, reducing economic costs and system complexity [74]. Reference [75] shows a solar water pumping system operating uninterrupted with PMSMs. Other studies focused on improving the PMSM control to adapt the operation for water pumping applications. For instance, in [76] a PMSM sensorless speed drive for single-stage photovoltaic (PV) water pumping applications is presented. It allows to remove current sensors, thus reducing installation costs, which is one of the most important requirements in this industry sector. Other studies as [77] improve PMSM drive, by proposing a fuzzy pre-compensated hybrid proportional integral (PI) controller, because it offers improved parameter sensitivity against conventional PI controllers with constant parameters.

Recent studies regarding PMSM design optimization methodologies focus on pumping applications. For instance, [78] designs a low voltage (12 Vdc) PM motor for electric transmission oil pump applications, whereas in [79] a high power SPMSM directly coupled pump application using time-dependent FEA is designed.

Despite new contributions in this field, there is a lack of works focusing on the PMSM design for water pumping applications, so this thesis contributes in this area.

2.9 Recent developments in parameter estimation and performance evaluation methodologies

Parameter estimation for electrical machines is an extensive research field. The main purpose is to characterize the motor performance, as well as to improve the motor drive control, thus adapting the performance to the specific PMSM application [80]. As mentioned in previous chapters, PMSMs require special attention due their capabilities, such as high precision, high dynamic performance, adaptability, reduced power losses, high torque density, etc. To take full advantage of these potentialities, advanced vector control algorithm are used [81].

FEA is commonly used to extract motor parameters [40] allowing to compute the motor performances under different operational conditions. Besides the great advantages, FEA has multiple drawbacks, thus making it difficult to be applied in industry applications. FEA requires a high computational burden, deep knowledge of geometry, winding topology, materials, etc. This increases the difficulty to characterize PMSM in industry applications because manufacturers usually do not provide the required data to reproduce the motor performance in FEA. Therefore, high interest has been put into parameter identification with measurable data, i.e., currents, voltages, or rotor speed among others [82].

Different methods can be found in the bibliography, which are divided in two main categories, i.e., online and offline parameter estimation [83]. Earliest studies such [84] presented an experimental approach to identify model parameters of different types of synchronous machines by evaluating flux linkages from voltage acquisitions. Later variants were introduced, for instance in [85] the magnetic model is characterized exclusively from experimental data without requiring any offline mathematical manipulation. Other improvements are found in [86], where the cross magnetic saturation effect is considered at standstill operation with or without locking the rotor. Other estimation strategies focus on a specific magnitude such as the rotor position by analyzing the current waveforms [87], not only in PMSMs but also in switched reluctance machines without using a position sensor [88].

Online parameter estimation identifies PMSM parameters in real-time operation, i.e., it avoids stopping the motor operation to perform the identification. There are three main categories, numerical methods [89]–[91], observer-based methods [92]–[95] and artificial intelligence (AI)-based methods [80][71]. Reference [96] analyzes the converter voltage disturbance influence on

the estimation, whereas [97] develops an online sensorless speed tracking for PMSMs. In [98] an active flux based sensorless control to estimate the rotor position at low speed is developed. Other improvements were introduced in [99], identifying the stator resistance and PM flux linkage. More recent studies lie on improving sensorless controls using parameter estimation algorithms, for instance [100] presents an online identification approach to detect the load current at low speed conditions, specially affected by the position estimation error. In [101] an online parameter estimation using high frequency (HF) signals estimated the impedance model, thus allowing to use this method either online or offline.

Offline methods obtain data separately for further parameter estimation. It requires stopping the motor operation and perform required experiments to extract data. Three main categories are defined, frequency domain methods [102], [103], time domain methods [82], [104] and finite element methods [105].

Performance evaluation of permanent magnet synchronous machines PMSM is an active research field, because it enables to reproduce the machine performance, reducing time, reducing costs and allowing to reproduce different scenarios [83]. Traditional testing methodologies require a great deal of time and efforts to prepare the experimental set up and to test different operating conditions. For instance, conventional tests include the non-load test, torque test, load test, loss test, thermal test and inductance test, among others. Data synchronization and the selection of the instrumentation in order to adapt the measurements to the specific application adds complexity to the problem.

Some standardized tests to measure PMSMs parameters to characterize its performance have been proposed, as the standstill frequency response (SSFR) [102], [106], [107]. In [108] a test based on generating sinusoidal signals by using a voltage-source inverter has been proposed. The IEEE 115-2019 standard [109] for synchronous machines performance identification considers different testing methods, nevertheless most of them are not applicable to PMSMs. Some testing methodologies for PMSMs have been proposed in the literature. For instance, [110] proposes an indirect testing methodology to determine the mechanical characteristic of the multiunit PMSM under no load conditions. Other studies focus on analyzing the PMSM losses by indirect testing, as [111] or [112], which develops a practical testing solution to optimally design the stator harmonic currents to minimize the torque ripple using speed harmonics. Other studies focus on identifying the PMSM parameters to then reproduce the motor performance using mathematical models together with measurable data, as voltages currents or rotor speed [82].

Different methodologies have been proposed in the literature, they being divided into online and offline parameter identification [83].

2.10 Standards and regulations

Electrical machines have to accomplish some standards and regulations if they are meant to be commercialized, which are listed in Table 4.

Table 4: Rotating electrical machines standards and regulations

Standard Title	IEC Standard	EN / DIN VDE
Rotating electrical machines. Rating and performance	IEC 60034-1 IEC 60085	EN 60034-1
Rotating electrical machines. Efficiency classes of single-speed, three-phase, cage-induction motors	IEC 60034-30	-
Rotating electrical machines. Standard methods for determining losses and efficiency from tests	IEC 60034-2-1	DIN EN 60034-2-1
Dimensions and output series for rotating electrical machines. Frame numbers 56 to 400 and flange numbers 55 to 1080.	IEC 60072	EN 50347
Rotating electrical machines. Terminal markings and direction of rotation	IEC 60034-8	EN 60034-8
Rotating electrical machines. Classification of types of construction, mounting arrangements and terminal box position.	IEC 60034-7	EN 60034-7
Rotating electrical machines. Thermal protection.	IEC 60034-11	-
Rotating electrical machines. Methods of cooling.	IEC 60034-6	EN 60034-6
Rotating electrical machines .Degrees of protection provided by the integral design of rotating electrical machines.	IEC 60034-5	EN 60034-5
Rotating electrical machines. Mechanical vibration of certain machines with shaft heights 56 mm and higher.	EN 60034-14	EN 60034-14
Rotating electrical machines. Noise limits.	IEC 60034-9	EN 60034-9
Rotating electrical machines. Starting performance of single-speed three-phase cage induction motors.	IEC 60034-12	EN 60034-12
CENELEC standard voltages.	IEC 60038	-

Special attention requires the IEC 60034-30 standard for efficiency classes for low voltage AC motors. This standard was published by the International Electrotechnical Commission on March 6 of 2014. The standard aims to harmonize the energy efficiency classes for electric motors. Compared with its previous version, i.e., IEC 60034-30:2008, the last update expands the range of products including 8 poles machines introducing the concept of IE4 efficiency performance class or super premium efficiency.

2.10.1 Efficiency class definition

There are four different efficiency classes, standard, high, premium and super premium efficiency. Each of them named IE1, IE2, IE3 and IE4 respectively.

Table 5: Efficiency classes

Super-Premium efficiency	IE4
Premium efficiency	IE3
High efficiency	IE2
Standard efficiency	IE1

The power ranges cover from 120 W to 10 MW. The new standard includes:

- Electrical machines with single speed, single phase and three phase at 50 and 60 Hz.
- 2, 4, 6, or 8 poles.
- Rated power from 120 W to 10 MW.
- Motors with continuous operation in rated power conditions accomplishing the temperature raise allowable by the insulation class.
- Ambient temperature from -20°C to 60°C.
- Maximum altitude up to 4000 m above sea level.

For instance, Figure 20 shows the efficiency levels versus the rated power for six pole machines at 50 Hz.

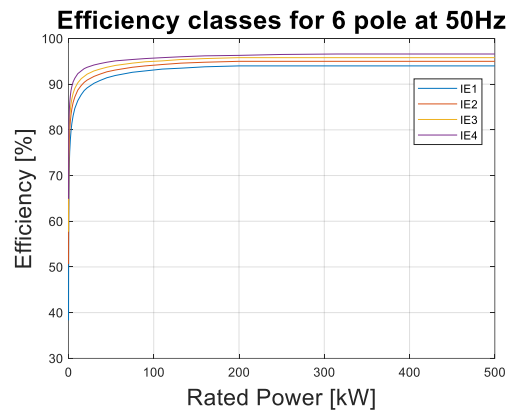


Figure 20: IE Energy efficiency classes curves for 6 pole at 50 Hz machines

3. Research and Development Methodology

This chapter introduces the development strategy to successfully achieve the objectives of the thesis. The research is divided in four main stages, i.e., definition, design, optimization and validation stages. For each one, the planned tasks are exposed, detailing the objectives of each one.

The aim of this chapter is to introduce the strategy of the project development to accomplish industrial doctorate goals either in terms of product development but as well as in scientific dissemination.

Contents

3.1	Methodology
-----	-------------

3.1 Methodology

The methodology diagram is exposed in Figure 21. The whole project has been divided in four main stages. The first is the definition stage where the electrical machine selection, the optimization strategy, the modeling technique, the parameter estimation and performance analysis methodology are defined. The second is the design stage, where the electrical machine model, the optimization algorithm, the testing and parameter estimation methodology and performance analysis algorithm are developed. The last is the validation stage, where all algorithms are validated either numerically and experimentally.

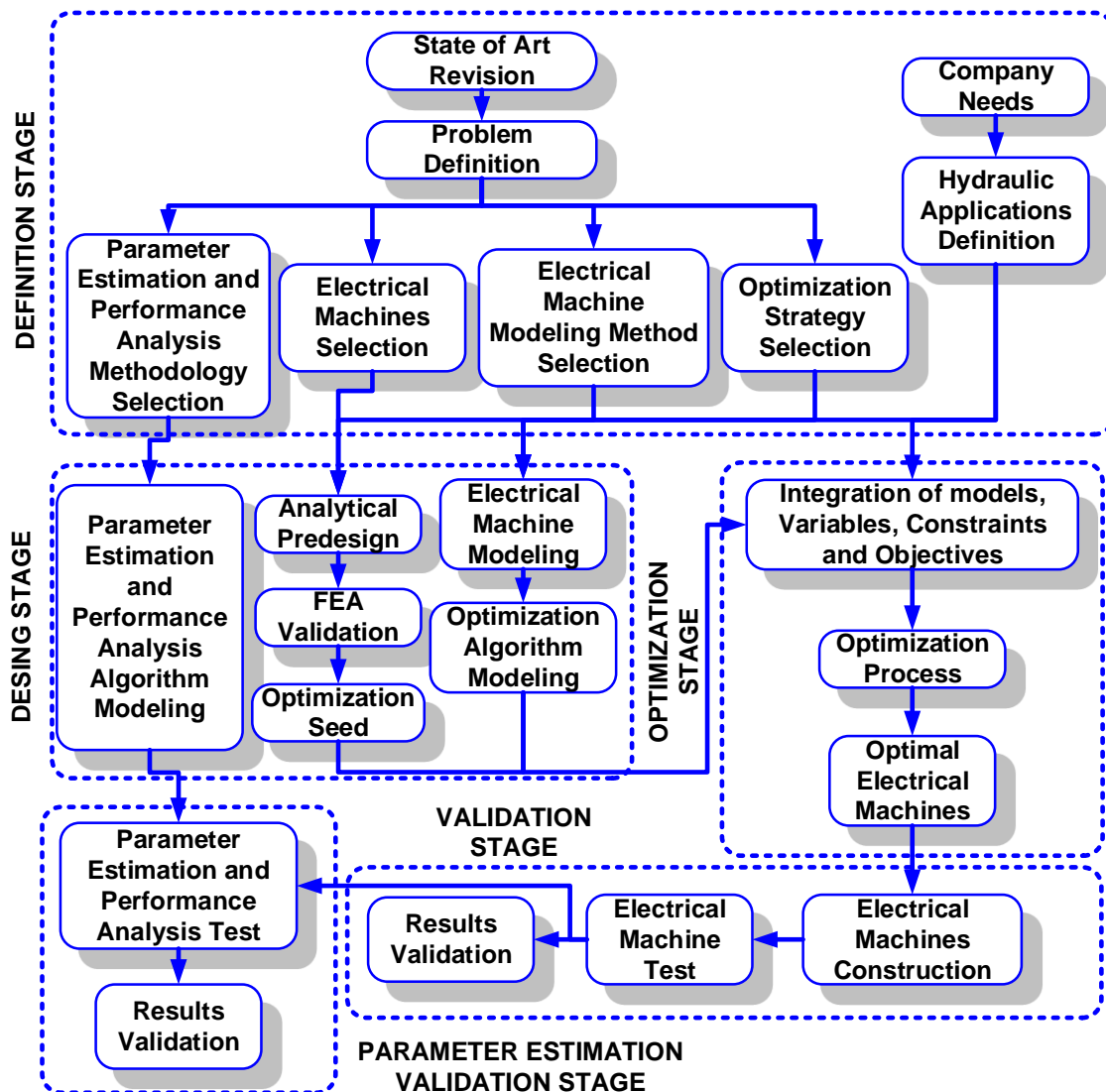


Figure 21: Methodology for the development of the research work

The methodology starts with the revision of state of art of whole disciplines related with the research field, such as the optimization techniques, electrical machines modeling, fault diagnosis,

parameter estimation algorithms, performance analysis, etc. As a result of this exhaustive review and considering the company needs as an industrial doctoral framework, the research requirements and the objectives are defined.

The process is developed following the sequence exposed in Figure 21.

1. Definition stage.

The definition stage aims to deepen in the research field by identifying the frontier of knowledge, thus providing all the information required to identify and outline the research and development strategy. The steps contained in this stage are:

1.1. **Electrical machine selection.** During this process the electrical machine is selected considering the water pump application.

1.2. **Modeling method for electrical machines** considering the available resources and accuracy.

1.3. **Optimization strategy selection** taking into account the modeling method and the available resources.

1.4. **Definition of the hydraulic applications.**

1.5. **Parameter estimation and performance analysis techniques** to characterize and complement the standard test once the electrical machine is designed.

2. Design stage.

The design stage includes three parallel fields of development. One is focused on the optimization seed creation, the second is focused on the development of the electrical machine model and optimization algorithm and the third is aimed to develop the parameter estimation and performance analysis.

2.1. **Analytical predesign process.** As a first design approximation, the electrical machine is designed using analytical equations. This geometry is used as an initial seed for the optimization process. By using the correct relations, this step improves the optimization performance, thus reducing time and increasing the accuracy of the solution.

2.2. **Predesign FEA validation.** A FEA analysis is conducted to validate the first candidate and check the predesign correctness.

2.3. Once the design is validated through FEA, there are the so called **optimization seeds**.

2.4. **The electrical machine magneto-static FEA modeling.**

2.5. **The optimization algorithm model.**

2.6. **Parameter estimation and performance analysis algorithms development** to characterize and complement the standard test once the electrical machine is designed.

3. Optimization stage.

Having the electrical machine seed, the FEA model and the optimization algorithm, the design optimization is run. This stage is divided in three tasks.

3.1. **Integration of models, variables, constraints and objectives.**

3.2. **Electrical machine optimization.**

3.3. **Optimal electrical machine selection.**

4. Validation stage.

The validation stage, is aimed **to manufacture, test and characterize the optimal electrical machine** obtained during the optimization stage.

4.1. **Electrical machine manufacturing.** During this process manufacturing aspects must be considered.

4.2. **Electrical machine test and characterization.** With the available instrumentation, the simulation results will be reproduced.

4.3. **Results validation.** By performing standard tests, the electrical machine performance is validated.

5. Parameter estimation and performance analysis validation stage.

5.1. **Parameter estimation test.** The manufactured machine is characterized, thus identifying the model parameters and validating its performance through the performance analysis algorithm.

5.2 **Results validation.**

4. Design Optimization Methodology

Electrical machines design and optimization is an active and wide area. Last trends focus on developing fast and reliable design algorithms using finite element analysis. As mentioned in the hypotheses section, the main objective is to design an electrical machine starting from the required characteristics found in the torque-speed-efficiency map. This chapter shows the methodology considering this main objective. The design optimization methodology is first validated with public experimental data from the Toyota Prius 2004 and Camry 2007 PMSMs. In the next chapter this algorithm is adapted for the electrical machine selected to the hydraulic application.

The methodology proposed uses ultra-fast finite element analysis (UF-FEA) by applying magneto-static computations together with a time-space conversion to compute the iron losses. It allows a great reduction of the computational resources and performing the design-optimization in an affordable time frame, while allowing to increase the number of variables to be optimized. The model considers the iron losses by using a time-space transformation together with pseudo rotating analysis, thus being possible to determine the magnetic flux density harmonic content using FEA. The torque-speed-efficiency map is calculated by applying a direct-quadrature ($d-q$) electrical model. The process designs the PMSM by adapting its performance to the predefined control strategy. For the same geometry it is possible to analyze the performance based on different control strategies, i.e., maximum torque per ampere (MTPA), maximum torque per volt (MTPV), maximum efficiency (ME), or flux weakening (FW). The objective function uses a novel image comparison technique, the structural similarity index (SSIM), which allows comparing the similarity of two torque-speed-efficiency maps.

Section 4.1 introduces the design optimization methodology, section 4.2 details the losses computation using magneto-static FEA computations, which have been one of the most difficult parts to develop, section 4.3 exposes the PMSM evaluation method developed to calculate the torque-speed-efficiency maps, section 4.4 shows the design optimization validation, and finally section 4.5 concludes the whole design optimization algorithm validation.

Contents

- 4.1 Design optimization algorithm
- 4.2 Losses computation
- 4.3 PMSM torque-speed-efficiency map evaluation based on magneto static FEA model validation
- 4.4 PMSM torque-speed-efficiency map design and optimization validation
- 4.5 PMSM design optimization conclusions

Nomenclature

\mathbf{B}_{xy}	Magnetic flux density in a defined region [T]
\mathbf{d}_{wire}	Wire diameter [m]
\mathbf{D}_{ir}	Inner rotor diameter [m]
\mathbf{D}_{is}	Inner stator diameter [m]
\mathbf{D}_{or}	Outer rotor diameter [m]
\mathbf{D}_{os}	Outer stator diameter [m]
\mathbf{f}_{obj}	Objective function [-]
\mathbf{g}	Air gap length [m]
\mathbf{h}_{brg}	Rotor bridge height [m]
\mathbf{h}_{PM}	Permanent magnet height [m]
\mathbf{h}_{rib}	Rotor rib height [m]
\mathbf{h}_{so}	Slot opening height [m]
\mathbf{h}_{sy}	Stator yoke height [m]
\mathbf{h}_t	Tooth height [m]
\mathbf{i}_d	Direct axis current [A]
\mathbf{i}_q	Quadrature axis current [A]
\mathbf{i}_s	Current space vector [A]
\mathbf{I}_{max}	Maximum current [A_{RMS}]
\mathbf{L}	Stack lamination length [m]
\mathbf{L}_d	Direct axis inductance [H]
\mathbf{L}_q	Quadrature axis inductance [H]
\mathbf{m}	Number of stator phases [-]
\mathbf{n}	Mechanical angular velocity [rpm]
\mathbf{N}_{ph}	Number of phase turns [-]
\mathbf{P}_U	Output power [W]
\mathbf{P}_{Fe}	Iron losses [W]
\mathbf{P}_{ML}	Mechanical Losses [W]
\mathbf{P}_{Cu}	Copper Losses [W]
\mathbf{p}	Pole pairs [-]
\mathbf{q}	Number of slots per pole and phase [-]
\mathbf{R}_{Fe}	Iron resistance [Ω]
\mathbf{R}_s	Phase winding resistance [Ω]

T	Output torque [N·m]
U_{dc}	DC bus voltage [V]
w_{brg}	Rotor bridge width [m]
w_{PM}	Permanent magnet width [m]
w_{so}	Slot opening width [m]
w_t	Tooth width [m]
w_{web}	Rotor web width [m]
α_{PM}	V-shape permanent magnet angle [rad]
η	Efficiency [p.u.]
θ_e	Electrical angle [rad]
θ_m	Mechanical angle [rad]
ω_e	Electrical angular velocity [rad/s]
Ψ_{abc}	Phase flux linkage [V·s]
Ψ_{PM}	Permanent magnet flux linkage [V·s]
Ψ_{sd}	Direct axis flux linkage [V·s]
Ψ_{sq}	Quadrature axis flux linkage [V·s]

4.1 Design optimization algorithm

This section introduces the design optimization algorithm to compute from a given torque-speed-efficiency map the PMSM geometry. The algorithm is divided in six different steps. The first step sizes the PMSM geometry (pre-design) by applying analytical equations and known values. Next, the geometry is computed in the FEA interface using magneto static computations. From FEA computations the flux linkage, magnetic flux density distribution along the stator and the electromagnetic torque are obtained for different space vector currents and rotor positions. From data acquired, losses can be computed by using analytical expressions either mechanical, iron or joule losses. To compute the efficiency map, the d - q electric model is used. The algorithm uses an image comparison technique called structural similarity index (SSIM) [113] to optimize the objective function, which is commented in detail in this section. Figure 22 details the design optimization algorithm.

4.1.1 Electromagnetic pre-design and geometry computation

The first step aims to size the initial geometry, also called seed geometry, using analytical equations and load rules found in the bibliography [114]. Applying the right sizing laws, the seed geometry will provide an approximation of the optimum performance required. This step has special importance to reduce the optimization time. Once the seed is obtained, the second step consists in evaluating the geometry to validate the correctness and mechanical robustness before FEA simulations are carried out.

4.1.2 Magneto-static study

The third step performs the magneto-static FEA study. As detailed in the state of the art chapter, the geometry is evaluated for different current space vectors and rotor positions. First, the positive direction of the direct axis belonging to the rotor, i.e., where the PM flux is facing outwards, is aligned with the stator reference phase. Once aligned, the different current space vectors are evaluated in the motoring quadrant for different rotor angles. Figure 23 details the algorithm described.

From the magneto static analysis, the flux linkage, magnetic flux density distribution along the stator and the electromagnetic torque are obtained for different space vector currents and rotor positions, thus having full information about these quantities for different operational scenarios.

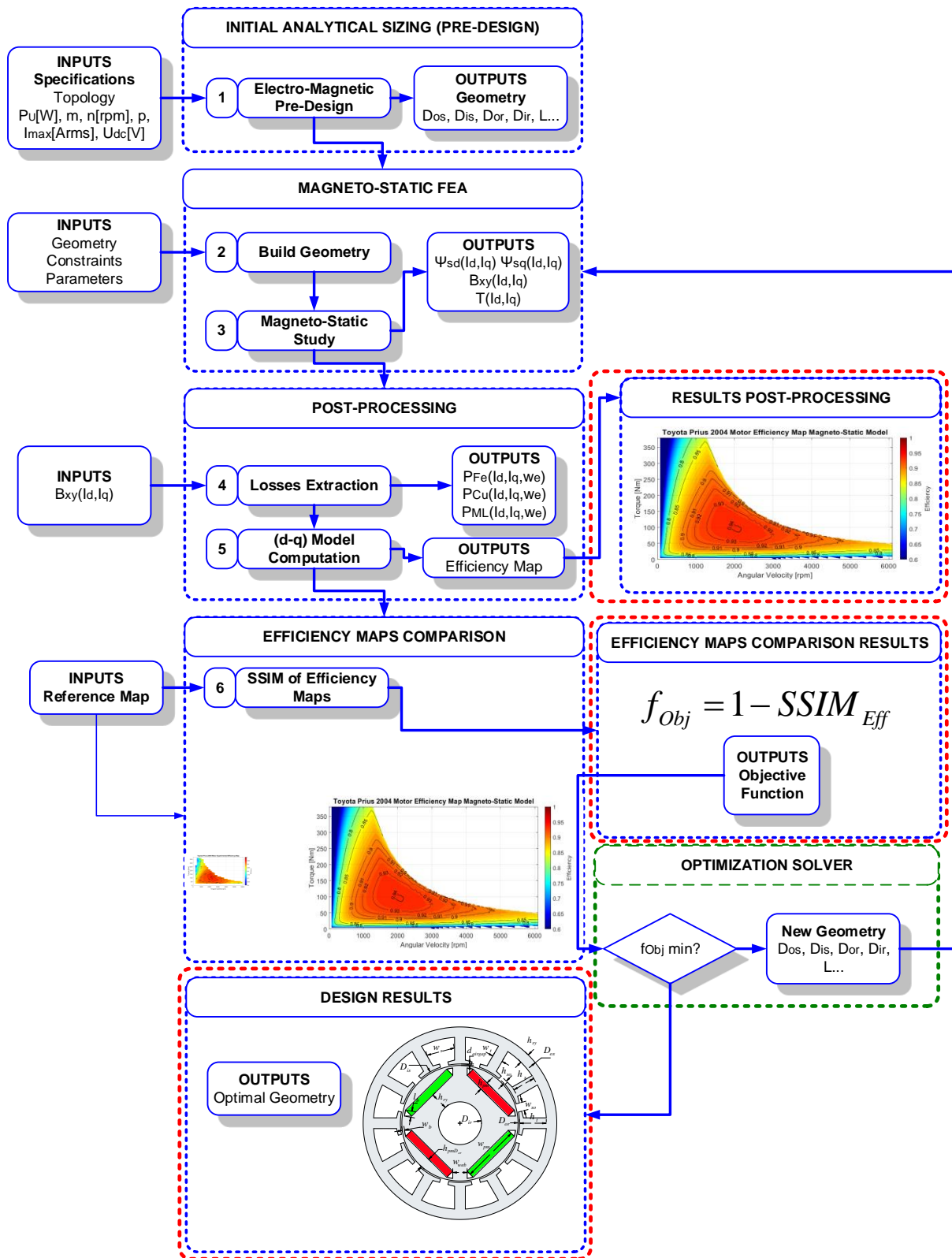


Figure 22: PMSM design optimization algorithm

```

1: Set the Current magnitude and angle steps:
    $i_s = 0 : \Delta i_s : i_{s \max}$ ,  $\theta_e = \pi : \Delta \theta_e : \pi / 2$ 
2: Set the mechanical angle steps:  $\theta_m = 0 : \Delta \theta_m : \tau_s / 2$ 
3: for  $\theta_e = \pi$  to  $\theta_e = \pi / 2$  do
4:   for  $i_s = 0$  to  $i_s = i_{s \max}$  do
5:     for  $\theta_m = 0$  to  $\theta_m = \tau_s / 2$  do
6:       Magneto-Static Analysis
7:     end
8:   end
9: end

```

Figure 23: Magneto static computations algorithm

4.2 Losses computation

When performing the magneto static analysis, the magnetic flux density along the motor for different conditions is available. All these data allow to calculate different losses using novel strategies, which are explained in this subsection.

4.2.1 Copper losses

The copper resistance of each phase is needed to compute the Joule effect losses. FEA software provides a fast method to provide this magnitude. Copper losses are calculated as,

$$P_{Cu} i_d, i_q = \left(\frac{m}{2}\right) \cdot R_s \cdot i_d^2 + i_q^2 \quad (75)$$

4.2.2 Mechanical losses

Mechanical losses for electrical machines depend mainly on vibrations and frictions, including bearings and air friction. These can be calculated using external models [17], [37].

4.2.3 Iron losses

Iron losses calculation in electrical machines using magneto-static FEA is a challenging point. The common model to evaluate iron losses is time-dependent Bertotti equations. They consider the time dependence of the magnetic flux density for every finite element. Magneto-static FEA

gives the magnetic flux density without time dependence. For this reason, this research proposes a new methodology to compute iron losses using magneto-static FEA.

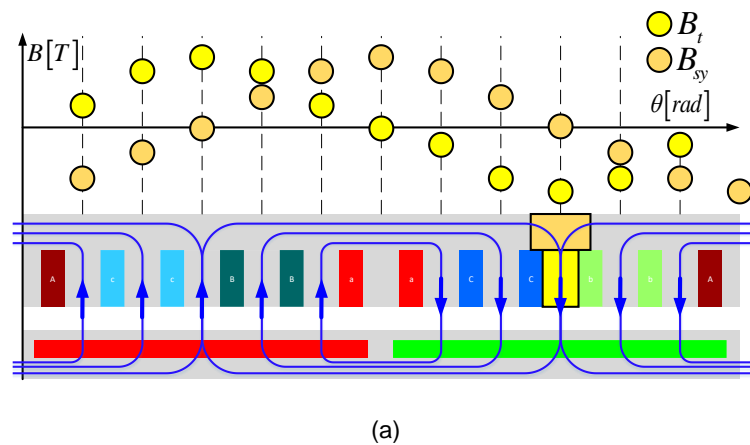
The method considers the magnetic flux density spatial distribution to estimate the time evolution for a given finite element. This approach avoids using the loss function to compute the efficiency maps [115], thus providing high precision. The $B-H$ curve of the corresponding ferromagnetic material is included the FEA software considering the saturation effects.

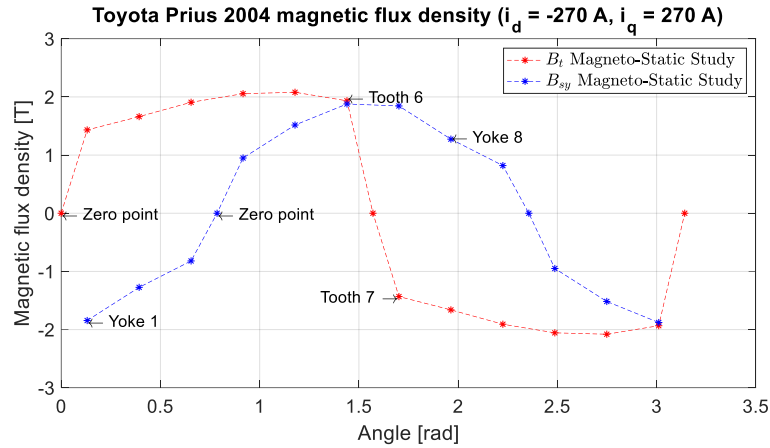
4.2.3.1 Magnetic flux density distribution

Two main regions are considered to evaluate the magnetic flux density distribution along the stator, the tooth and yoke regions. Each region is considered as a repeatable part along the stator. Therefore, for a given time instant, each of the repeatable parts represent a discrete state of the period. To do so, the spatial distribution of each of these elements is monitored. The magnetic flux density is integrated for each domain,

$$\int_s \frac{B_{\Delta}}{s_{\Delta}} \cdot ds \quad (76)$$

Being ds the differential surface, s_{Δ} the finite surface composed by the finite elements mesh and B_{Δ} the mean of magnetic flux density correspondent for each finite surface. Figure 24 shows the discrete magnetic flux density distribution along the commented regions.





(b)

Figure 24: Magnetic flux density discrete distribution over the stator teeth and yoke regions (a). Toyota Prius 2004 magnetic flux density distribution at $i_d = -270$ A and $i_q = 270$ A (b)

The prior hypothesis to approximate the space variation as a representative state of the time variation is because the time variation of the magnetic vector potential is almost negligible due to the small value of the electrical frequencies dealt with. Therefore, the values of magnetic vector potential in the time domain are equivalent to those of the static domain.

$$\frac{1}{\mu} \cdot \left(\frac{\partial^2 A}{\partial x^2} + \frac{\partial^2 A}{\partial y^2} \right) = -J + \frac{\partial A}{\partial t} \cdot \sigma \quad (77)$$

The term $(\partial A / \partial t) \cdot \sigma$ can be neglected due its low contribution. Another aspect to consider when modelling ferromagnetic materials using two dimensional FEA is that eddy currents are not simulated.

4.2.3.2 Harmonic wave decomposition

Considering the space distribution of the magnetic flux density, the equivalent wave is decomposed in harmonic components. The time-space conversion is applied to transform Bertotti equations from time dependent to the equivalent space distribution.

$$\left(\frac{dB}{d\theta_e} \right) = \left(\frac{dB}{dt} \right) \cdot \left(\frac{dt}{d\theta_e} \right) \rightarrow \left(\frac{dB}{dt} \right) = \left(\frac{dB}{d\theta_e} \right) \cdot \omega_e \quad (78)$$

The magnetic flux density integration is merged in Bertotti equations applying the time-space conversion. The modified Bertotti equations to calculate iron losses using magneto static FEA are as follows,

$$P_{Fe-Eddy} = \frac{\sigma \cdot h^2}{12 \cdot T} \cdot \omega_e^2 \cdot \int_0^T \int_{d\forall} \left(\frac{d \int_s \frac{B_\Delta}{s_\Delta} \cdot ds}{d\theta_e} \right)^2 \cdot d\forall \cdot d\theta_e \quad (79)$$

$$P_{Fe-Hyst} = \frac{K_h \cdot \rho}{T} \cdot \int_{d\forall} \left(\int_s \frac{B_\Delta}{s_\Delta} \cdot ds \right)_m^\alpha \cdot \left(1 + \sum_{i=1}^n \frac{\beta}{\left(\int_s \frac{B_\Delta}{s_\Delta} \cdot ds \right)_m} \cdot \left(\Delta \left(\int_s \frac{B_\Delta}{s_\Delta} \cdot ds \right)_i \right) \right) \cdot d\forall \quad (80)$$

$$P_{Fe-Excess} = \frac{K_{exc} \cdot \rho}{T} \cdot \omega_e^{1.5} \cdot \int_0^T \int_{d\forall} \left(\frac{d \left(\int_s \frac{B_\Delta}{s_\Delta} \cdot ds \right)}{d\theta_e} \right)^{1.5} \cdot d\forall \cdot d\theta_e \quad (81)$$

4.2.4 d - q Electrical model computation

The d - q electrical model is used to compute the PMSM torque-speed-efficiency. Figure 25 shows the electrical representation.

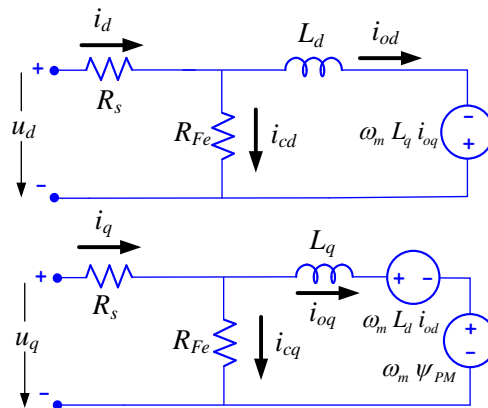


Figure 25: (d - q) electrical model representation

Considering the components in Figure 25, the transient equations can be derived from this model. For the purpose of representing the torque-speed-efficiency map, the quasi static equations are used [42]. The main advantage of using d - q modeling is the possibility to evaluate different control strategies, being a huge advantage over other available models [116].

First, from magneto static FEA computations, the d - q flux linkages are obtained,

$$\begin{cases} \psi_d = \psi_{PM} + L_d i_{od} \\ \psi_q = L_q i_{oq} \end{cases} \quad (82)$$

Then, from these magnitudes together with the electrical angular speed, the back electromotive force (BEMF) can be obtained as,

$$\begin{cases} u_{od} = -\omega_e \cdot L_q \cdot i_{oq} = -\Psi_q \cdot \omega_e \\ u_{oq} = \omega_e \cdot (L_d \cdot i_{od} + \Psi_{PM}) = \Psi_d \cdot \omega_e \end{cases} \quad (83)$$

Each of the current space vector evaluated during the magneto static FEA computation determines the i_{oq} and i_{od} values.

The iron losses are modeled by means of a parallel resistance.

$$R_{Fe} = \frac{m \cdot (u_{od}^2 + u_{oq}^2)}{2 \cdot P_{Fe}} \quad (84)$$

The currents corresponding to the iron losses resistance, i.e., i_{cd} and i_{cq} are calculated as,

$$\begin{cases} i_{cd} = \frac{u_{od}}{R_{Fe}} \\ i_{cq} = \frac{u_{oq}}{R_{Fe}} \end{cases} \quad (85)$$

The total currents i_d and i_q are calculated from i_{cd} , i_{cq} , i_{oq} and i_{od} .

$$\begin{cases} i_d = i_{od} + i_{cd} \\ i_q = i_{oq} + i_{cq} \end{cases} \quad (86)$$

Finally, the voltage equations are as,

$$\begin{cases} u_d = R_s \cdot i_d + L_d \cdot \frac{d}{dt} \cdot i_{od} - \omega_e \cdot L_q \cdot i_{oq} \\ u_q = R_s \cdot i_q + L_q \cdot \frac{d}{dt} \cdot i_{oq} + \omega_e \cdot L_d \cdot i_{od} + \omega_e \cdot \Psi_{PM} \end{cases} \quad (87)$$

Figure 26 details the procedure to compute the torque-speed-efficiency map using a d - q electrical model.

- 1: Extract magneto-static FEA data: $\psi_a(i_d, i_q), \psi_b(i_d, i_q), \psi_c(i_d, i_q), B_{xy}(i_d, i_q), T(i_d, i_q), R_s$
- 2: Extract losses from magneto-static FEA data: $P_{Fe}(i_d, i_q, f), P_{ML}(f), P_{Cu}(i_d, i_q)$
- 3: Torque-speed domain discretization: $T = 0: \Delta T: T_{\max}, \omega_e = 0: \Delta \omega_e: \omega_{e\max}$
- 4: Control strategy selection (MTPA, ME or MTPV)
- 5: Compute BEMF for all $\omega_e: u_{oq} = \psi_d \cdot \omega_e, u_{od} = \psi_q \cdot \omega_e$
- 6: Compute iron resistance R_{Fe} for all $\omega_e: R_{Fe} = m \cdot (u_{od}^2 + u_{oq}^2) / (2 \cdot P_{Fe})$
- 7: Compute d - q iron currents i_{cd}, i_{cq} for all $\omega_e: i_{cd} = u_{od} / R_{Fe}, i_{cq} = u_{oq} / R_{Fe}$
- 8: Compute d - q currents i_d, i_q for all $\omega_e: i_d = i_{od} + i_{cd}, i_q = i_{oq} + i_{cq}$
- 9: Compute copper losses for all $\omega_e: P_{Cu} = (m/2) \cdot R_s \cdot (i_d^2 + i_q^2)$
- 10: Selection of the magnitudes from control strategy

Figure 26: (d - q) electrical model algorithm to compute the torque-speed-efficiency map considering the control strategy

4.2.5 Torque-speed efficiency maps comparison

From previous steps, the PMSM geometry is evaluated by using magneto-static FEA computations. Later, losses are derived to compute the d - q electrical modeling and thus, torque speed efficiency map is computed. Now, the solver needs to compare the torque-speed-efficiency map evaluated against the reference one. To do so, the structural similarity index is used [113], [117].

4.2.5.1 Structural similarity index SSIM

The SSIM returns a normalized value between 0 and 1 to indicate the similarity between two matrices. The SSIM considers three main parameters: Intensity, standard deviation and data structure. Each of the commented aspects provides different information about the images x and y .

The mean value of the reference matrix x is defined as,

$$\mu_x = \frac{1}{N} \sum_{i=1}^{N_i} \sum_{j=1}^{N_j} x_{ij} \quad (88)$$

Being N the total number of component s of the matrix $N=N_i \cdot N_j$ and x_{ij} the (i,j) component of the matrix.

The intensity is defined as,

$$l_{x,y} = \frac{2 \cdot \mu_x \cdot \mu_y + C_1}{\mu_x^2 + \mu_y^2 + C_1} \quad (89)$$

x and y are the comparison matrices and C_1 and constant used to avoid computational instabilities when $\mu_x^2 + \mu_y^2 \approx 0$.

The standard deviation is defined as,

$$\sigma_x = \left(\frac{1}{N-1} \cdot \sum_{i=1}^{N_i} \sum_{j=1}^{N_j} (x_{ij} - \mu_x)^2 \right)^{\frac{1}{2}} \quad (90)$$

The indicator which compares the standard deviation of matrices,

$$c_{x,y} = \frac{2 \cdot \sigma_x \cdot \sigma_y + C_2}{\sigma_x^2 + \sigma_y^2 + C_2} \quad (91)$$

Last indicator evaluates the normalized matrices analyzing the data structure. It is defined as,

$$s_{x,y} = \frac{\sigma_{xy} + C_3}{\sigma_x \cdot \sigma_y + C_3} \quad (92)$$

σ_{xy} is the correlation coefficient between matrices.

$$\sigma_{xy} = \frac{1}{N-1} \cdot \sum_{i=1}^{N_i} \sum_{j=1}^{N_j} (x_{ij} - \mu_x) \cdot (y_{ij} - \mu_y) \quad (93)$$

Finally, the structural similarity index SSIM is defined as,

$$SSIM = l(x,y) \cdot c(x,y) \cdot s(x,y) \quad (94)$$

4.2.6 Optimization solver

After calculating the SSIM, the objective function is computed. As the objective is to minimize the difference between the two images, the objective function is defined as,

$$f_{obj} = 1 - SSIM \quad (95)$$

Based on this objective function, the solver modifies the geometric parameters in order to approach as much as possible to the required solution. The solver selected for this study is *pattern search* solver from Matlab®. It is suitable for non-continuous and non-differentiable objective functions.

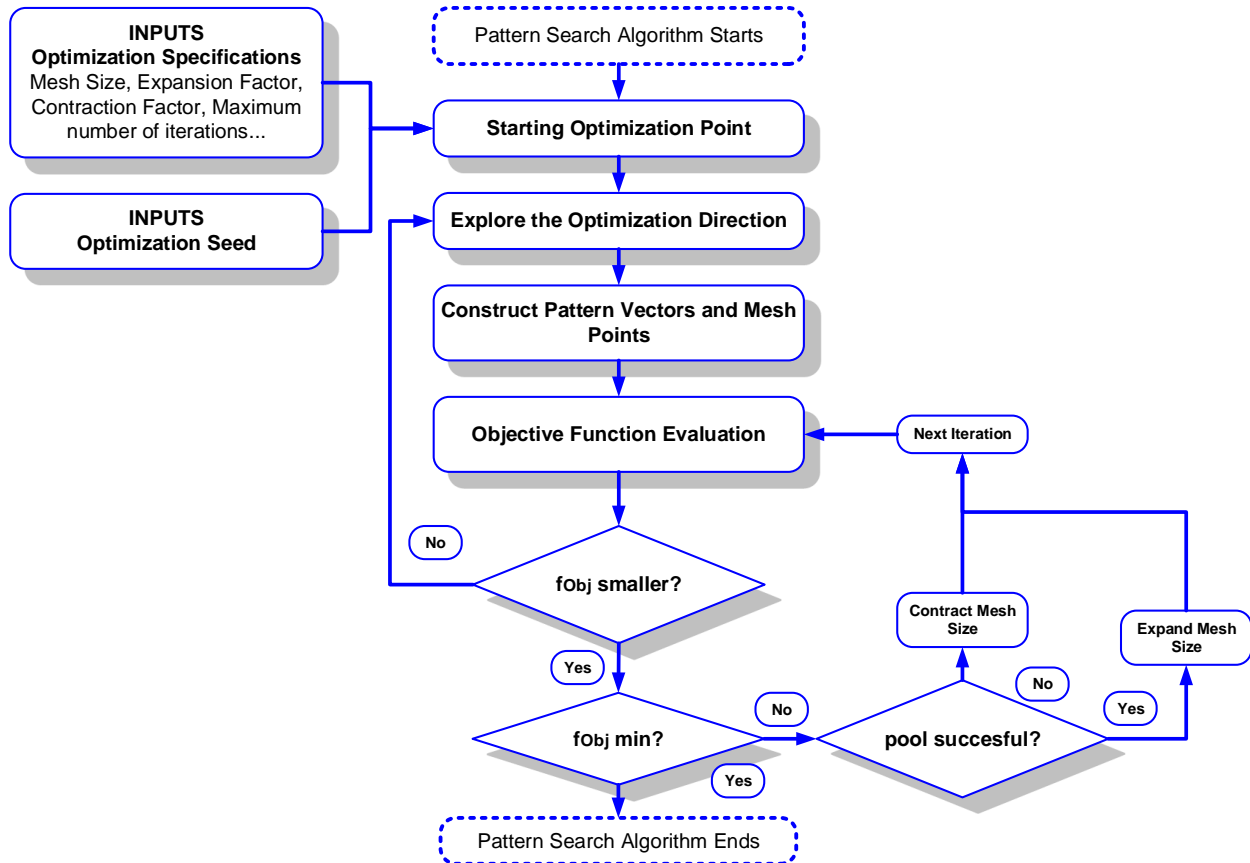
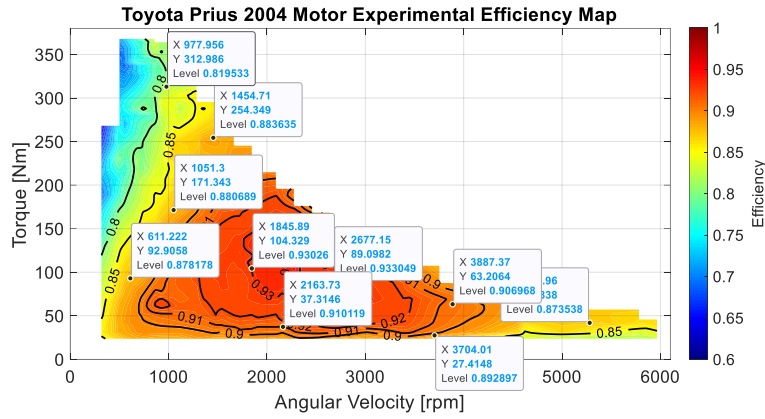


Figure 27: Pattern search optimization solver algorithm description

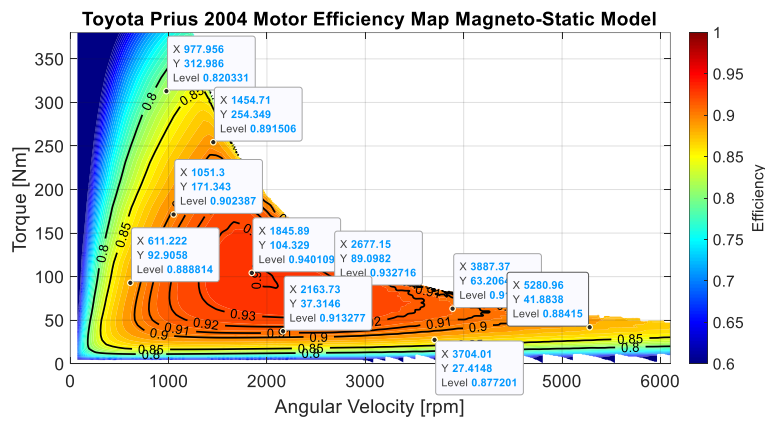
4.3 PMSM torque-speed-efficiency map evaluation based on magneto static FEA model validation

The experimental data of PMSM of Toyota Prius 2004 [118] is used to validate the magneto static FEA together with the d - q electrical model (geometric dimensions, currents, voltages, materials, power losses, temperature, etc.). The experimental torque-speed-efficiency map [118] is used as a reference. Then, introducing the original PMSM geometry to the magneto-static FEA model, the torque-speed-efficiency map obtained is compared against the original map obtained experimentally in [118]. Thus validating the magneto-static FEA model as an evaluation tool.

Ten operational points are selected to compare the efficiency values obtained using the magneto static FEA model with the losses model, which are exposed in Table 6. Figure 28 shows the PMSM Toyota Prius 2004 torque-speed-efficiency map obtained through experiments in [118] (a) and obtained using the magneto static model proposed in this thesis (b).



(a)



(b)

Figure 28: PMSM Toyota Prius 2004 experimental efficiency map (a). PMSM Toyota Prius 2004 magneto static model torque-speed-efficiency map.

Table 6: PMSM Toyota Prius 2004 torque-speed-efficiency

Regime Characteristics		Isostatic model	Experimental	Relative error (%)
Angular velocity (rpm)	Torque (Nm)	Efficiency (p.u)	Efficiency (p.u)	
611.2	92.91	0.8888	0.8780	1.23
1051	171.3	0.9024	0.8807	2.46
978	313	0.8203	0.8195	0.10
1455	254.3	0.8915	0.8836	0.89
1846	104.3	0.9401	0.9303	1.05
2164	37.31	0.9133	0.9101	0.35
2677	89.1	0.9327	0.9330	0.03
3704	27.41	0.8772	0.8929	1.75
3887	63.21	0.9144	0.9070	0.82
5281	41.88	0.8842	0.8735	1.22

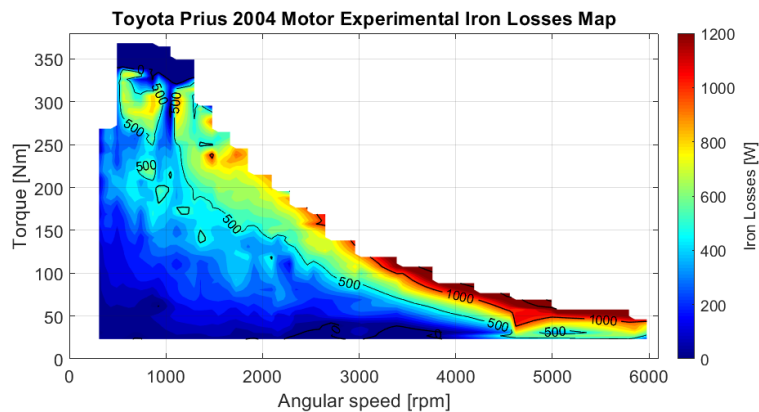
According to the values exposed in Table 6, the relative error between the efficiencies measured by [118] and those obtained through magneto static FEA method is below 2% for every operational point. As explained previously, the SSIM index compares the similitude between two matrices, in this case between both torque-speed-efficiency maps (Figure 28 (a) and (b)) the SSIM is 0.958. As mentioned previously, iron losses are the most complex magnitude to estimate when using magneto static FEA computations. For this reason, the losses model is compared against time-dependent FEA. To carry out the comparison ten points are chosen to determine the difference between them. Table 7 summarizes the values.

Table 7 PMSM Toyota Prius 2004 iron losses magneto static method vs time dependent FEA

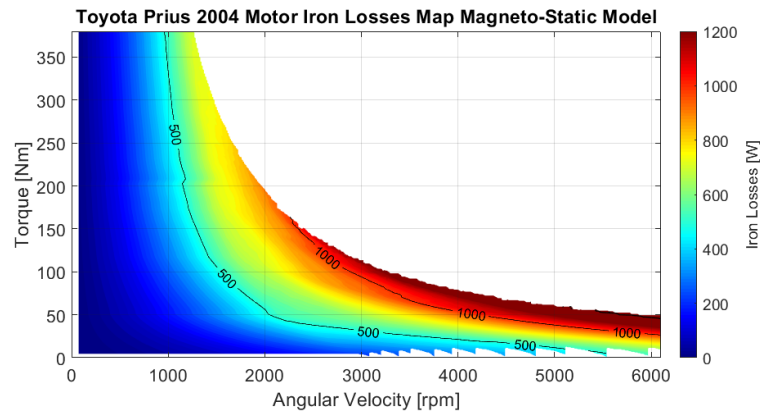
Regime Characteristics			Magneto Static ML Model (W)	Time Dependent ML Model (W)	Relative error (%)
Angular velocity (rpm)	<i>d</i> -axis current (A)	<i>q</i> -axis current (A)			
431.3	-101.1	106.1	38.61	36.31	6.33
1479	-28.47	45.88	128.74	121.16	6.26
4005	-69.25	23.97	597.43	585.73	2.00
4005	-132.1	27.65	947.82	921.47	2.86
5792	-114.3	18.28	1584.14	1680.78	5.75
6038	-79.28	16.59	1299.93	1348.71	3.62

As can be observed in Table 7, the relative error between both approaches is below 6.33 %, this maximum error corresponding to low speed operation. Finally, in order to validate the iron losses taking as a reference the Toyota Prius 2004 PMSM, transformations are needed in order to decouple experimental iron losses from experimental data.

$$P_{Fe} = P_U / \eta - P_U - P_{Cu} - P_{ML} \quad (96)$$



(a)



(b)

Figure 29: PMSM Toyota Prius 2004 torque-speed-iron losses map, experimental (a) vs magneto static FEA model (b)

Figure 29 shows great similarity between experimental and magneto static FEA model. Thus, the iron losses model is validated.

The magneto static FEA together with $d-q$ electrical model applying iron losses model, show high accuracy analyzing PMSMs geometries and calculating its performance characteristics. Therefore, the evaluation tool can be incorporated into an optimization environment providing a fast and accurate of the machine.

4.4 PMSM torque-speed-efficiency map design and optimization validation

PMSMs Toyota Prius 2004 [118] and Camry 2007 [119] public experimental data are used to validate the entire design optimization process using magneto static FEA together with a $d-q$ electrical model. First, a seed geometry is defined. Due to space constraints, the outer stator diameter is constant during the optimization process, whereas the shaft diameter remains constant due to the defined torque requirements. Some other parameters remain constant during the pre-design stage in order to provide mechanical robustness and winding process feasibility (h_{brg} , h_{rib} , h_{so} , w_{so} , w_{brg}). Moreover, these parameters have low impact in the PMSM performance characteristics.

Table 8 shows the predesign constant parameters against the reference geometric variables of the Toyota Prius 2004/Camry 2007 PMSMs predesign parameters. The optimization parameters range is defined by the designer considering the application, space constraints and manufacturing tolerances.

Table 8: PMSM Toyota Prius 2004/Camry 2007 predesign parameters

Geometry Parameter	Seed values	Optimized values Prius/Camry	Reference values
	Prius/Camry		Prius/Camry
h_{brg} [mm]	1.5/2.0	1.5/2.0	1.65/2.04
h_{rib} [mm]	2.5/0	2.5/0	2.8/0
h_{so} [mm]	1.0/1.0	1.0/1.0	1.1/1.02
w_{brg} [mm]	2.0/3.5	2.0/3.5	2.09/3.8
w_{so} [mm]	2.0/2.0	2.0/2.0	1.93/1.88
w_{web} [mm]	0/1.5	0/1.5	0/1.65

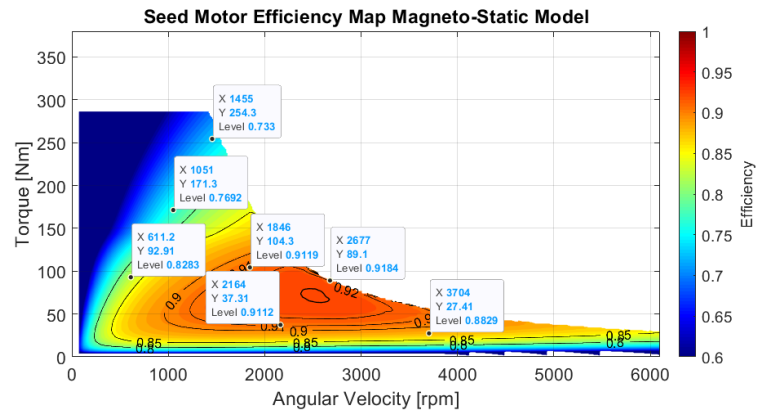
4.4.1 PMSM Toyota Prius 2004 validation

Table 9 summarizes the predesign seed parameter values, the optimized geometry parameters, the original Toyota Prius 2004 PMSM geometry values and the relative error between the real and optimized values.

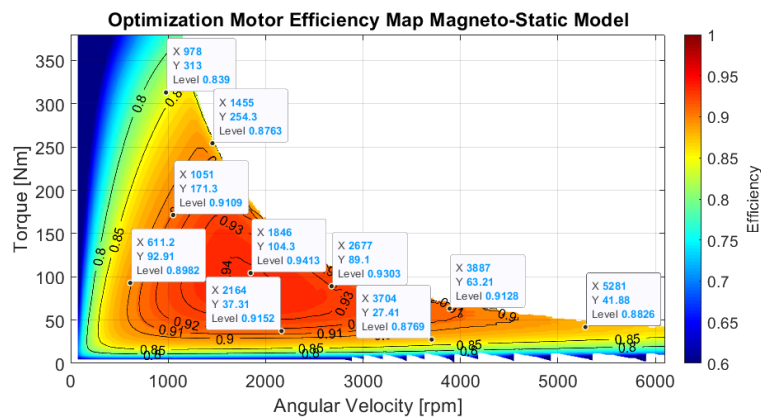
Table 9: PMSM Toyota Prius 2004 geometric parameters comparison

Parameter	Seed value	Lower/upper optimization bounds	Optimized geometry	Toyota Prius geometry	Error (%)
g [mm]	1	0.2/1.5	0.747	0.75	0.40
D_{or} [mm]	190	115/230	161.38	160.5	0.55
h_t [mm]	20	5/60	32.84	33.5	1.97
w_t [mm]	4	2/10	7.51	7.6	1.18
h_{sy} [mm]	18.6	5/60	20.32	20.1	1.09
h_{PM} [mm]	8	3/10	6.77	6.5	4.15
w_{PM} [mm]	15	10/25	17.61	18	2.17
L [mm]	60	1/300	81.59	83.6	2.40
N_{ph}	100	8/200	80	72	11.11
d_{wire} [mm ²]	0.85	0.5/1.5	0.89	0.91	2.20
α_{PM} [°]	95.3	90/180	135.75	145	6.38

As observed in the previous table, the geometry obtained through the design optimization methodology reproduces with high fidelity the original PMSM Toyota Prius 2004 geometry. The highest parameter divergence is observed in the number of turns per phase, which the model converges with one conductor per slot more with respect to the original winding. Nevertheless, this conductor per slot has low effect on the torque-speed-efficiency maps because the optimization compensates this extra conductor per slot by decreasing the magnet size and stack length, thus obtaining similar torque-speed characteristics.



(a)



(b)

Figure 30: PMSM Toyota Prius 2004 seed torque-speed-efficiency map (a) and design optimization geometry (b)

Table 10 compares the torque-speed-efficiency values in different operating points of the optimized machine against the original geometry. The relative errors validate the design optimization accuracy not only evaluating PMSMs geometries but providing the original geometry by giving the torque-speed-efficiency map.

The SSIM between the torque-speed-efficiency map seed and experimental motors is 0.701, whereas after the optimization is 0.929.

Table 10: PMSM Toyota Prius 2004 experimental and design optimization magneto static efficiency map comparison

Regime characteristics		Optimized geometry efficiency (p.u)	Experimental efficiency (p.u)	Relative error (%)
Angular velocity (rpm)	Torque (Nm)			
611.2	92.91	0.8982	0.8780	2.30
1051	171.3	0.9109	0.8807	3.43
978	313	0.8390	0.8195	2.38
1455	254.3	0.8763	0.8836	0.83
1846	104.3	0.9413	0.9303	1.18
2164	37.31	0.9152	0.9101	0.56
2677	89.1	0.9303	0.9330	0.29
3704	27.41	0.8769	0.8929	1.79
3887	63.21	0.9128	0.9070	0.64
5281	41.88	0.8826	0.8735	1.04

4.4.2 PMSM Toyota Camry 2007 validation

Following the same procedure as previously exposed, PMSM Toyota Camry 2007 experimental data are used to validate on second hand the design optimization algorithm giving the torque-speed-efficiency map. Table 11 shows the seed values of the optimization parameters including the geometry solution after the optimization process.

Table 11: PMSM Toyota Camry 2007 geometric parameters comparison

Parameter	Seed value	Lower/upper optimization bounds	Optimized geometry	Toyota Camry geometry	Error (%)
g [mm]	1	0.2/1.5	0.738	0.75	1.60
D_{or} [mm]	190	115/230	162.203	160.5	1.06
h_t [mm]	20	5/60	28.97	30.9	6.25
w_t [mm]	4	2/10	7.613	7.6	0.17
h_{sy} [mm]	18.6	5/60	21.2	20.1	5.47
h_{PM} [mm]	8	3/10	6.477	6.6	1.86
w_{PM} [mm]	15	10/25	18.42	19.1	3.56
L [mm]	40	1/300	62.311	60.6	2.82
N_{ph}	80	8/200	56	56	0.00
d_{wire} [mm ²]	0.63	0.5/1.5	0.881	0.812	8.50
α_{PM} [°]	95	90/180	141.59	145	2.35

As can be observed in the previous table, the geometry obtained after the design-optimization process matches with the original PMSM Toyota Camry 2007 geometry.

Figure 31 (a) shows the PMSM Toyota Camry 2007 torque-speed-efficiency map obtained using public data. (b) shows the torque-speed-efficiency map evaluating the original geometry using time-dependent FEA. Finally, (c) shows the torque-speed-efficiency map obtained through the design optimization algorithm using magneto static analysis together with d - q modelling.

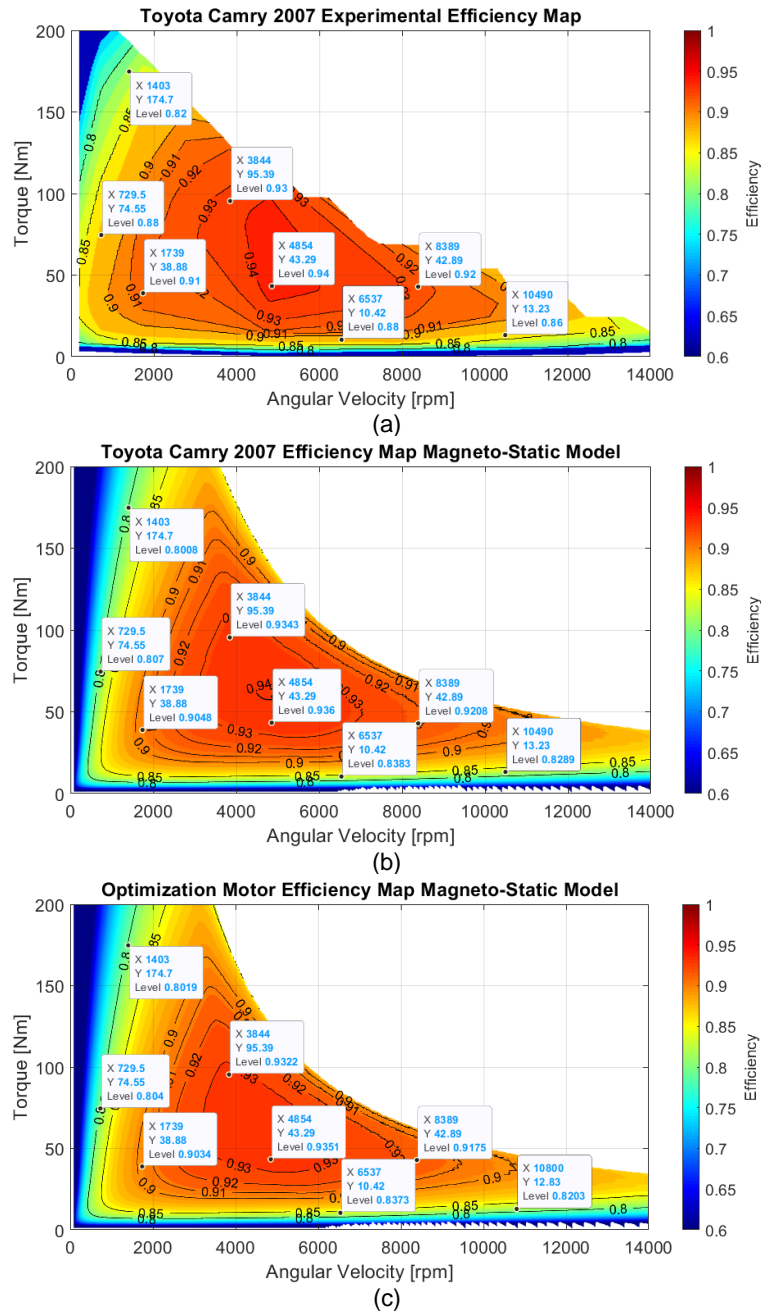


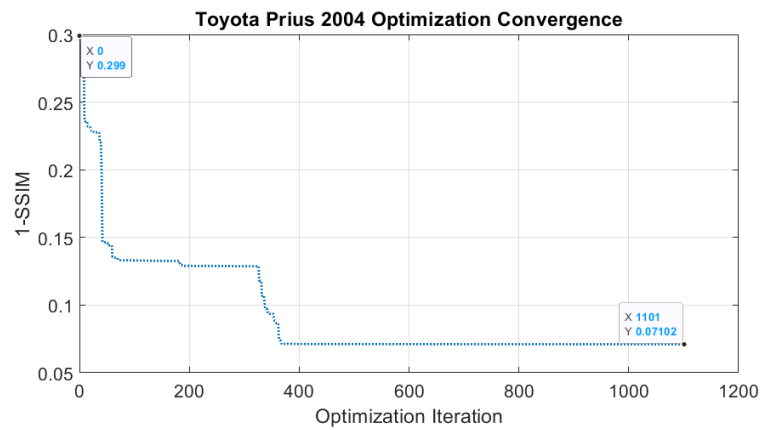
Figure 31: PMSM Toyota Camry 2007 torque-speed-efficiency map (a) Obtained through experimental data (b) Obtained using original geometry through time-dependent FEA model (c) Obtained through design optimization algorithm using magneto-static FEA model

Analyzing the figure above, the SSIM between the torque-speed-efficiency map obtained with experimental data and the one obtained using time dependent FEA is 0.9695, whereas against the design optimization algorithm using magneto static FEA is 0.9571. These values inform about the accuracy when finding the original geometry from the torque-speed efficiency map.

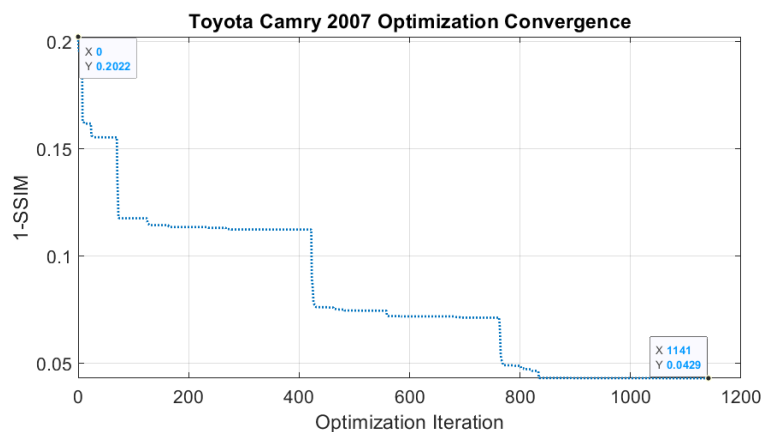
4.4.3 Target completion of PMSMs Toyota Prius 2004 / Camry 2007

For the design optimization algorithm, a target degree of 5% when computing the objective function 1-SSIM is defined.

For Toyota Prius 2004 PMSM, the SSIM between the geometry obtained using the design optimization algorithm and the experimental map is 0.929, thus obtaining a relative deviation of 3.03%. In the case of Toyota Camry 2007 PMSM the deviation is less than 1.28%.



(a)



(b)

Figure 32: *Patternsearch* optimization convergence (a) PMSM Toyota Prius 2004 (b) PMSM Toyota Camry 2007

As can be observed in Figure 32 the optimization solver required around 1100 iterations to converge.

4.4.4 Computational burden

The design optimization algorithm requires 30 to 40 seconds to perform one optimization evaluation. This time depends on the saturation conditions of the iron material. *Patternsearch* algorithm optimizer available in Matlab® required 5 days to find the optimum solution. The number of function evaluations is limited to 10000. The available resources are Intel® Core™ i9-7940X 3.10 GHz processor with 64 GB RAM memory.

The time required is reasonable, since the algorithm allows to obtain the correct PMSM geometry by giving beforehand the torque-speed-efficiency map with high precision. Moreover, if the algorithm is used as a design tool, the time is considered competitive avoiding several design iterations to manufacture the prototype, saving time labor and cost.

4.5 PMSM design optimization conclusions

A methodology for designing and optimizing permanent magnet synchronous motors (PMSM) by combining magneto-static FEA and direct-quadrature (d - q) electrical modeling has been developed. This method presented huge advantages as decreasing computational burden compared to conventional methods FEA methods. The input of the optimization algorithm is the target torque-speed-efficiency map. The design-optimization process searches the motor geometry fitting its torque-speed-efficiency map to the target. Maps comparison is performed using an image comparison technique known as structural similarity index (SSIM). To calculate the torque-speed-efficiency map, a magneto-static FEA combined with (d - q) electrical modeling algorithm is developed considering iron, mechanical and copper losses. For Iron losses calculation, it is considered the magnetic flux density spatial harmonic components.

To validate the methodology, public experimental data of Toyota Prius 2004 PMSM was used. The torque-speed-efficiency map is calculated using the original PMSM geometry, and then it is compared with the experimental one. According to the values presented, the relative error of the experimental efficiencies and those obtained by means of the proposed method is below 2% in the whole torque-speed plane. Results show high accuracy of the algorithm when reproducing the PMSM characteristics of a verified geometry.

Finally, once the magneto-static FEA model was validated, the accuracy of the whole design-optimization algorithm method was assessed by using the experimental torque-speed-efficiency

maps of the Toyota Prius 2004 and Toyota Camry 2007 PMSMs as target objectives. It was found that the geometries obtained in both cases through the optimization process were very similar to these of the original machines, thus confirming the accuracy of the proposed design-optimization method.

For Toyota Prius 2004 PMSM the SSIM index resulting from the comparison of the seed torque-speed-efficiency map and the experimental one is 0.701, whereas the SSIM index between the torque-speed-efficiency map of the optimized motor and the experimental one is 0.929. For Toyota Camry 2007 PMSM. The SSIM index between the seed torque-speed-efficiency map and the experimental one is 0.7978, whereas the SSIM index between the torque-speed-efficiency map of the optimized motor and the experimental one is 0.9571.

5. Water Pumping design application

This chapter presents the PMSM design optimization methodology focused on hydraulic applications and concretely, for the industrial application of this project. Due to its features, PMSM is the main topology to work with in this study as explained at the beginning of this chapter. The methodology presented and validated in the previous chapter is adapted for water pumping applications.

This research work develops a methodology to design and optimize PMSMs by defining the desired torque-speed-efficiency map adapting its performance to the water pump (WP) hydraulic characteristics. Once the hydraulic efficiency is known, the approach presented in this paper offers the designer plenty of freedom to customize the design of the PMSM by defining the target efficiency map in the torque-speed plane, while ensuring the desired performance of the WP-PMSM system. Finally, the proposed methodology is validated experimentally by designing and testing a PMSM adapted to a real WP.

Section 5.1 introduces the electrical machine topology and concentrated double-layer winding selection including the number of poles and slots, section 5.2 details the PMSM design for water pumping applications based on efficiency maps, section 5.3 shows the PMSM characteristics, section 5.4 exposes the PMSM time dependent FEA validation, section 5.5 gives information related to the computational burden, and finally section 5.6 exposes the conclusions.

Contents

- 5.1 Electrical machine topology selection
- 5.2 PMSM-WP design methodology with efficiency maps
- 5.3 PMSM Characteristics
- 5.4 PMSM validation by means of Time Dependent FEA Validation
- 5.5 Optimization Convergence and Computational Burden
- 5.6 PMSM design and optimization methodology. Conclusions

Nomenclature

B_{xy}	Magnetic flux density [T]
D_{ir}	Inner diameter of the rotor [m]
D_{is}	Inner diameter of the stator [m]
D_{or}	Outer diameter of the rotor [m]
D_{os}	Outer diameter of the stator [m]
f_{obj}	Objective function [-]
g	Air gap length [m]
h_{PM}	Permanent magnet height [m]
h_{sy}	Height of the stator yoke [m]
h_t	Height of the tooth [m]
H_{pump}	Pump pressure [mH ₂ O]
i_d	Direct axis current [A]
i_q	Quadrature axis current [A]
i_s	Current space vector [A]
I_{max}	Maximum stator current [A_{RMS}]
L	Length of the stack laminations [m]
L_d	Inductance in the direct axis [H]
L_q	Inductance in the quadrature axis [H]
m	Phases number [-]
n	Rotor angular speed [1/min]
N_{ph}	Turns per phase [-]
p	Pairs of poles [-]
P_{Cu}	Copper losses [W]
P_{Fe}	Iron losses [W]
P_{ml}	Mechanical losses [W]
P_{pump}	Pump input power [W]
q	Slots per pole and phase [-]
Q_{pump}	Volumetric flow rate [L/h]
R_{Fe}	Resistance of the iron [Ω]
R_s	Resistance of the stator windings per phase [Ω]
T	Output mechanical torque [N·m]
U_{dc}	Voltage of the DC bus [V]

w_{PM}	Width of the permanent magnets [m]
w_t	Width of the stator tooth [m]
η	Energy efficiency [p.u]
η_{pump}	Pump efficiency [p.u]
θ_e	Electrical angular position [rad]
θ_m	Mechanical angular position [rad]
ω_m	Electrical angular speed [rad/s]
τ_s	Slot pitch angle [rad]
Ψ_{abc}	Flux linkage in the stator [V·s]
Ψ_{PM}	Flux linkage of the permanent magnets [V·s]
Ψ_{sd}	Flux linkage in the direct axis [V·s]
Ψ_{sq}	Flux linkage in the quadrature axis [V·s]

5.1 Electrical machine topology selection

This section exposes the process followed to select the electrical machine topology. The selection process has been done considering multiple incoming aspects from the available resources, company needs and research trends in water pumping field.

5.1.1 Product requirements

The product requirements were introduced by the company based on the market trends and features of competitor's products.

Table 12: Product requirements

DC bus voltage	200 V
Maximum power	600 W
Maximum speed	6000 rpm
Rated speed	4500-5000 rpm
Maximum torque ripple	10 %
Maximum pole pairs	8
Number of phases	3
Maximum stator diameter	90 mm
Maximum stack length	60 mm
Winding type	concentrated
Refrigeration type	Water
Noise	Low noise

As can be seen, the rated speed is not defined, because it is a design variable. The efficiency requirements of the electrical machine and the whole system respectively are defined in Table 13.

Table 13: Efficiency requirements

Angular speed (rpm)	Torque (Nm)	System Efficiency (p.u.)	PMSM Efficiency (p.u.)
5200	1.00	-	0.84
4700	0.70	0.50	-

As can be seen in the previous table, there are two important points to be considered when designing the electrical machine. At 5200 rpm and 1 Nm, i.e., 545 W, the PMSM is aimed to accomplish IE4 premium efficiency standard. Moreover, in order to improve the whole product efficiency and provide energy saving system over competing products, the system efficiency is aimed to be 50 % at 4700 rpm.

5.1.2 Synchronous machine topology selection

Due to the requirements of the application, i.e., high efficiency, low ratio between the maximum angular speed and the rated angular speed and on the other hand considering the motor drives available for this product, the preferable synchronous machine topology is the permanent magnet synchronous machine.

5.1.3 Poles and slots for winding selection

The correct selection of poles and slots to implement a concentrated fractional slot winding is of major importance because it presents multiple advantages, such as reduction of end winding losses, reduction of torque ripple by reducing the periodicity between the number of slots and pole pairs, reduction of mutual coupling between phases, etc. [120].

5.1.3.1 Poles and slots combinations options

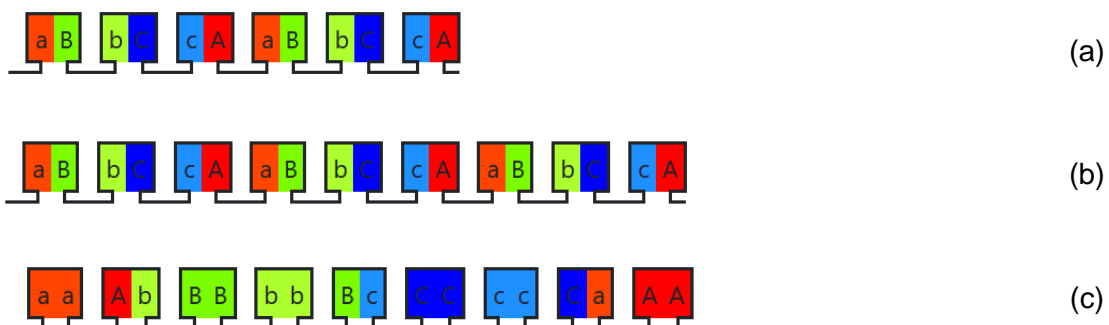
Considering the manufacturing aspect, the type of winding to be used is a double layer concentrated winding, because it is easier to manufacture than the single layer concentrated type.

Different options are considered on first hand, with 4, 6, 8 and 10 poles respectively, taking into account the first harmonic winding factor.

Table 14: Fundamental winding factor for 4, 6, 8 and 10 poles / 6, 9 and 12 slots

Slots\Poles	4	6	8	10
6	0.866	-	0.866	0.5
9	0.617	0.866	0.945	0.945
12	1	-	0.866	0.933

Five different options arise from this first selection. First, the winding layouts for each of the candidates are shown.



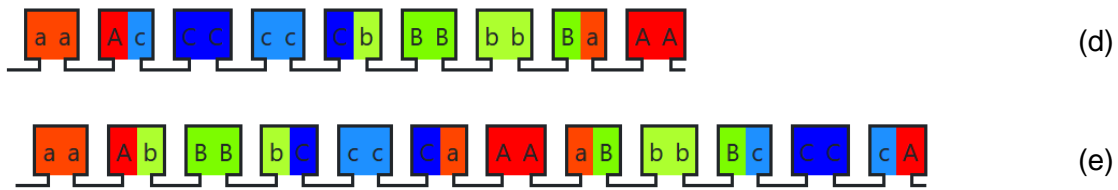


Figure 33: Double layer winding layout candidates (a) 4 poles 6 slots, (b) 6 poles 9 slots, (c) 8 poles 9 slots, (d) 10 poles 9 slots and (e) 10 poles 12 slots [121].

5.1.3.2 Star of slots

This formulation to analyze double layer concentrated windings will provide information about the harmonic order content as well as the sequence of phasors [120]. To do so, some properties are defined.

- **Machine periodicity:** The machine periodicity t corresponds to the identical parts in which the machine can be divided. It is defined as the greatest common divisor between the number of slots and the pole pairs.

$$t = G.C.D. Q, p \quad (97)$$

- **Winding feasibility:** A winding is feasible when, the following relation is an integer value.

$$\frac{Q}{m \cdot t} \quad (98)$$

- **Spokes:** The spokes are the number of slots contained in one machine periodicity or the number of arrays containing the star of slots.

$$\frac{Q}{t} \quad (99)$$

- **Angle between phasors:** This is the angle between two phasors in electrical degrees.

$$\alpha_s^e = p \cdot \frac{2 \cdot \pi}{Q} \quad (100)$$

- **Angle between two spokes:**

$$\alpha_{ph} = \frac{2 \cdot \pi}{Q/t} \quad (101)$$

5.1.3.2.1 4 poles 6 slots:

Table 15: Star of slots properties for 4 poles and 6 slots

Machine periodicity, $t = \text{G.C.D}\{Q,p\}$	2
Winding Feasibility, Q/mt	1
Spokes, Q/t	3
Angle between phasors, α_s^e	$2\pi/3$
Angle between two spokes, α_{ph}	$2\pi/3$

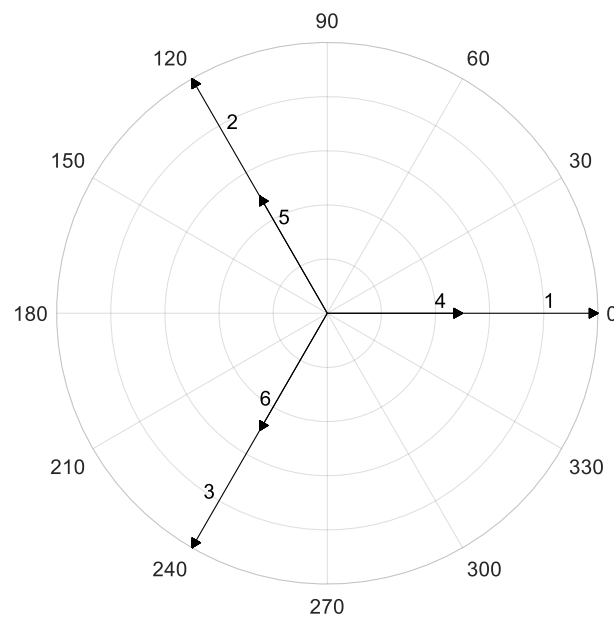


Figure 34: 4 poles 6 slots machines star of slots for three phases

Being the relation Q/t an odd number, this winding produces odd and even magneto motive force harmonics by an order of $t=2$. The following table shows the harmonic magneto motive force components.

Table 16: MMF harmonic content of 4 poles 6 slots for double layer concentrated winding

Harmonic	1	2	3	4	5	6	7	8	9	10	11
MMF [p.u]	0.866	0.433	-	0.217	0.173	-	0.124	0.108	-	0.087	0.079

5.1.3.2.2 6 poles 9 slots:

Table 17: Star of slots properties for 6 poles and 9 slots

Machine periodicity, $t = \text{G.C.D}\{Q,p\}$	3
Winding Feasibility, Q/mt	1
Spokes, Q/t	3
Angle between phasors, α_s^e	$2\pi/3$
Angle between two spokes, α_{ph}	$2\pi/3$

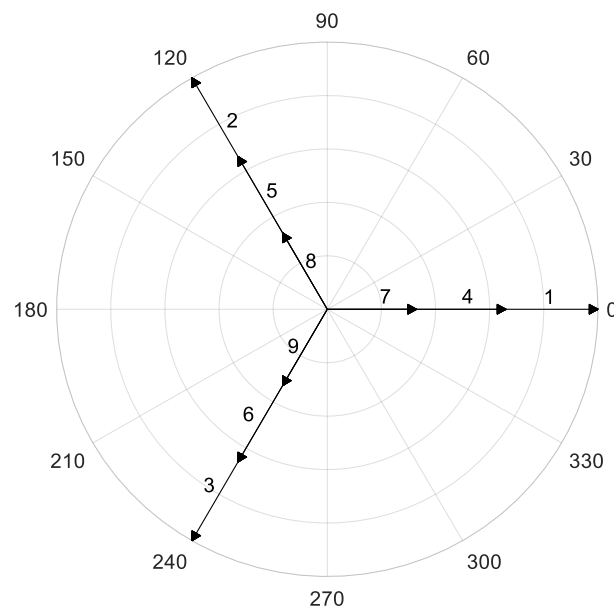


Figure 35: 6 poles 9 slots machines star of slots for three phases

Being the relation Q/t an odd number, this winding produce odd and even magneto motive force harmonics by an order of $t=3$. The following table shows the harmonic magneto motive force components.

Table 18: MMF harmonic content of 6 poles 9 slots for double layer concentrated winding

Harmonic	1	2	3	4	5	6	7	8	9	10	11
MMF [p.u]	0.866	0.433	-	0.217	0.173	-	0.124	0.108	-	0.087	0.079

5.1.3.2.3 8 poles 9 slots:

Table 19: Star of slots properties for 8 poles and 9 slots

Machine periodicity, $t = \text{G.C.D}\{Q,p\}$	1
Winding Feasibility, Q/mt	3
Spokes, Q/t	9
Angle between phasors, α_s^e	$8\pi/9$
Angle between two spokes, α_{ph}	$2\pi/9$

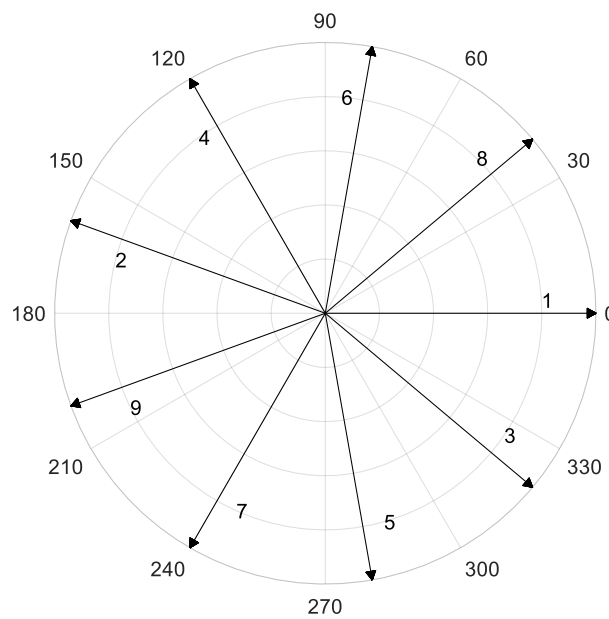


Figure 36: 8 poles 9 slots machines star of slots for three phases

Being the relation Q/t an odd number, this winding produce odd and even magneto motive force harmonics by an order of $t=1$. Nevertheless, this combination produces super harmonics multiples of 0.25 of the fundamental frequency.

The following tables show the harmonic magneto motive force components.

Table 20: MMF super harmonic content of 8 poles 9 slots for double layer concentrated winding

Harmonic	0.25	0.5	1.25	1.75	2.5	2.75	3.25	3.5	4.25	4.75	5.5	5.75
MMF [p.u]	0.243	0.28	0.756	0.08	0.024	0.051	0.291	0.27	0.014	0.013	0.172	0.164
Harmonic	6.25	6.5	7.25	7.75	8.5	8.75	9.25	9.5	10.25	10.75	11.5	11.75
MMF [p.u]	0.022	0.009	0.019	0.122	0.016	0.007	0.007	0.015	0.092	0.013	0.005	0.012

Table 21: MMF harmonic content of 8 poles 9 slots for double layer concentrated winding

Harmonic	1	2	3	4	5	6	7	8	9	10	11
MMF [p.u]	0.945	0.03	-	0.035	0.028	-	0.009	0.118	-	0.095	0.006

5.1.3.2.4 10 poles 9 slots:

Table 22: Star of slots properties for 10 poles and 9 slots

Machine periodicity, $t = \text{G.C.D}\{Q,p\}$	1
Winding Feasibility, Q/mt	3
Spokes, Q/t	9
Angle between phasors, α_s^e	$10\pi/9$
Angle between two spokes, α_{ph}	$2\pi/9$

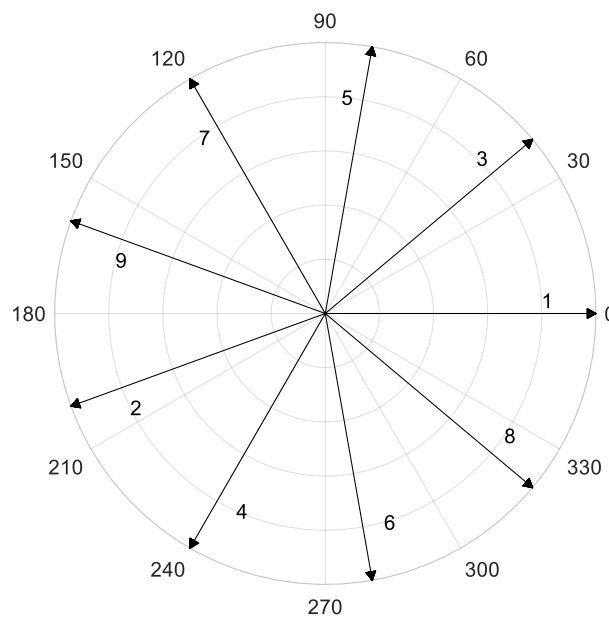


Figure 37: 10 poles 9 slots machines star of slots for three phases

Being the relation Q/t an odd number, this winding produce odd and even magneto motive force harmonics by an order of $t=1$. On the other hand, this combination produces super harmonics of order 0.2 of the fundamental frequency.

The following tables show the harmonic magneto motive force components.

Table 23: MMF super harmonic content of 8 poles 9 slots for double layer concentrated winding

Harmonic	0.2	0.4	0.8	1.4	1.6	2.2	2.6	2.8	3.2	3.4	3.8	4.4
MMF [p.u]	0.303	0.35	1.182	0.1	0.038	0.064	0.364	0.334	0.044	0.018	0.016	0.215
Harmonic	4.6	5.2	5.6	5.8	6.2	6.4	6.8	7.4	7.6	8.2	8.6	8.8
MMF [p.u]	0.205	0.012	0.011	0.024	0.152	0.148	0.021	0.008	0.018	0.115	0.016	0.007
Harmonic	9.2	9.4	9.8	10.4	10.6	11.2	11.6	11.8	12.2	12.4	12.8	13.4
MMF [p.u]	0.007	0.015	0.096	0.013	0.006	0.012	0.081	0.080	0.011	0.005	0.005	0.071

Table 24: MMF harmonic content of 8 poles 9 slots for double layer concentrated winding

Harmonic	1	2	3	4	5	6	7	8	9	10	11
MMF [p.u]	0.945	0.03	-	0.035	0.028	-	0.009	0.118	-	0.095	0.006

5.1.3.2.5 10 poles 12 slots:

Table 25: Star of slots properties for 10 poles and 12 slots

Machine periodicity, $t = \text{G.C.D}\{Q,p\}$	1
Winding Feasibility, Q/mt	4
Spokes, Q/t	12
Angle between phasors, α_s^e	$10\pi/12$
Angle between two spokes, α_{ph}	$2\pi/12$

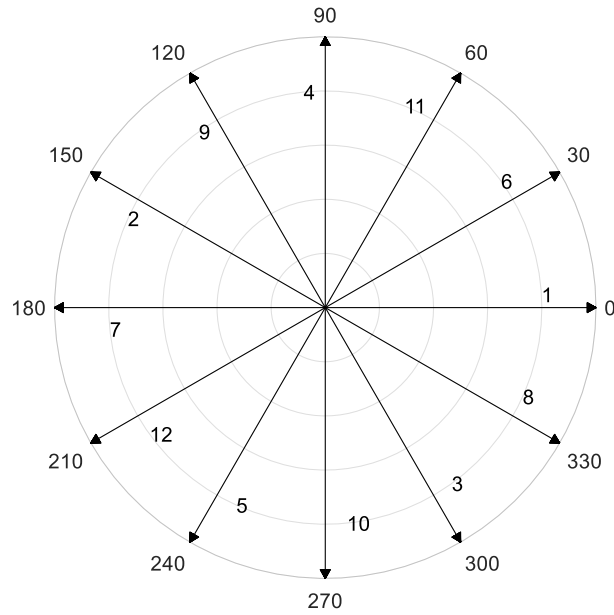


Figure 38: 10 poles 12 slots machines star of slots for three phases

In this case the relation Q/t is an even number, this winding produce even magneto motive force harmonics by an order of $t=1$. This winding does not produce odd magneto motive force harmonics due there is always two opposite coils with reverse orientation, the harmonics of even number produced in two opposite coils are compensated mutually. Nevertheless, this winding produces super harmonics multiples of 0.2 of the fundamental frequency.

The following tables show the harmonic magneto motive force components.

Table 26: MMF super harmonic content of 8 poles 12 slots for double layer concentrated winding

Harmonic	0.2	1.4	2.2	2.6	3.4	3.8	4.6	5.8	6.2	7.4	8.2	8.6
MMF [p.u.]	0.335	0.666	0.03	0.026	0.274	0.246	0.015	0.161	0.15	0.009	0.114	0.108
Harmonic	9.4	9.8	10.6	11.8	12.2	13.4	14.2	14.6	-	-	-	-
MMF [p.u.]	0.007	0.007	0.088	0.006	0.005	0.070	0.005	0.005				

Table 27: MMF harmonic content of 8 poles 12 slots for double layer concentrated winding

Harmonic	1	2	3	4	5	6	7	8	9	10	11
MMF [p.u.]	0.933	-	-	-	0.013	-	0.010	0.085	-	-	0.085

5.1.3.3 Poles and slots combination selection

Considering the analysis of each of the combinations selected and based on the harmonic content, the combination of 6 poles and 9 slots is selected. The reasons of discarding the other options are listed below.

- **4 poles 6 slots:** Despite having the same MMF harmonic content than the selected combination, and the same fundamental winding factor, there are different drawbacks. The first is related to the magnet size, since a 4-poles combination requires larger magnets for each pole for the same torque density. Therefore, the magnet associated with one pole is larger in size, increasing the manufacturing process complexity, because larger magnets are more difficult to insert in the rotor slots, thus increasing the probability of breaking them. Another aspect to consider, is the possibility of reducing the iron core material in the yoke in a 6-poles machine compared to a 4-poles machine.
- **8 poles 9 slots:** This combination has the main drawback in the MMF harmonic content, specially the MMF of 0.756 at 1.25 times the fundamental frequency. This MMF super harmonic is 80% of the fundamental MMF component. This would lead into unstable and potentially harmful operation.
- **10 poles 9 slots:** This combination, as the previous has the main drawback in the MMF harmonic content, specially the MMF of 1.182 at 0.8 times the fundamental frequency. This MMF super harmonic is 125% of the fundamental MMF component. This would lead into unstable and potentially harmful operation. In addition, 10 pole combinations have higher iron losses contributions, because for the same rotational speed the fundamental frequency is higher.
- **10 poles 12 slots:** This combination, as the two last options, has the main drawback in the MMF harmonic content, specially the MMF of 0.666 at 1.4 times the fundamental frequency. This MMF super harmonic is 71% of the fundamental MMF component. This would lead into unstable and potentially harmful operation. Furthermore, 10 pole combinations have higher iron losses contributions, because for the same rotational speed the fundamental frequency is higher.

5.2 PMSM-WP design methodology with efficiency maps

This section introduces the PMSM design optimization methodology for water pumping applications using torque-speed-efficiency maps using the methodology explained in the previous chapter.

The methodology to apply the design optimization algorithm to water pumping applications is divided in five steps, which are exposed in Figure 39. The algorithm starts from the hydraulics characteristics. The characteristics are WP efficiency (η_{pump}), pressure (H_{pump}) and mechanical pump power (P_{pump}). Using these curves, the WP torque-speed-efficiency map is obtained. This transformation allows to express the hydraulic characteristics within torque-speed plane. As exposed in the previous section, the PMSM design optimization starts defining the desired torque-speed-efficiency map. This efficiency distribution is meant to be customized by the designer based on the required PMSM performance in a selected torque-speed area.

PMSM rated characteristics, power envelope and losses distribution are defined in the initial stage. The objective is to provide the designer with plenty of freedom to design the motor according to the hydraulic application requirements.

According to the hypothesis section, the process starts with the hydraulic characteristics [122], efficiency (η_{pump}), pressure (H_{pump}) and power (P_{pump}) over the volumetric flow rate (Q_{pump}) for different angular speeds.

As introduced in the hypothesis section, from the pump power demand P_{pump} for every angular speed n , the torque demand can be calculated for all analyzed points as equation (1).

$$T_{pump}(Q_{pump}, n) = \frac{P_{pump}(Q_{pump}, n)}{n} \quad (1)$$

Knowing the torque demands for all operational points $T_{pump}(Q_{pump}, n)$ and having the associated hydraulic efficiency $\eta_{pump}(Q_{pump}, n)$, magnitudes are rearranged to express hydraulic efficiency over torque and rotational speed $\eta_{pump}(n, T_{pump})$. This conversion was introduced in the hypothesis section (equation (2)).

$$T_{pump}(Q_{pump}, n), \eta_{pump}(Q_{pump}, n) \rightarrow \eta_{pump}(n, T_{pump}) \quad (2)$$

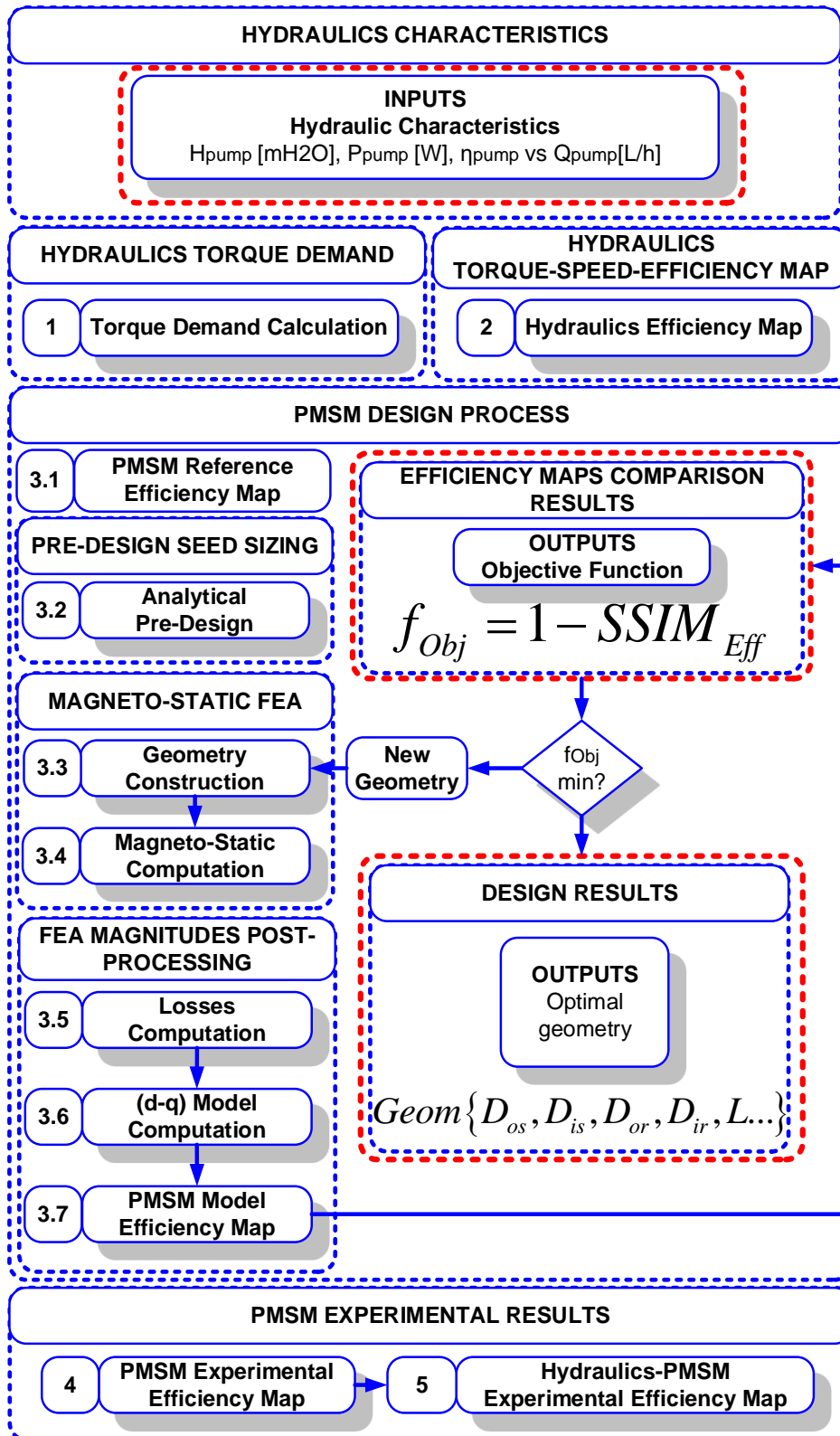


Figure 39: PMSM design methodology for WP applications using torque-speed-efficiency maps

Figure 4 showed the experimental WP torque-speed-efficiency map. If this map is known, it is possible to select an area of interest in order to design the motor. By knowing the WP efficiency characteristics, the PMSM efficiency can be defined before starting the design process. This ensures the required system efficiency for the selected application.

The proposed method is divided in seven steps following the design-optimization process (3.1 to 3.7 from Figure 39). Step 3.1, the target torque-speed-efficiency map is defined. This first step is the most important design stage, because the designer sets the desired motor performance within the torque-speed plane and the algorithm performs the designs taking into account these characteristics. After this, the geometry of an initial PMSM is calculated by means of analytical equations (step 3.2). This was used in previous study to calculate the optimization seed in order to find PMSMs Toyota Prius 2004 and Camry 2007 solutions. The objective, in this case, is the same, i.e., to provide a seed geometry for the optimization process. Once the seed geometry is calculated, a magneto-static electromagnetic analysis is performed (3.3 and 3.4 from Figure 39). Motor losses are calculated from data (3.5), the torque-speed-efficiency map is computed using a $d-q$ circuit model (3.6 and 3.7 from Figure 39). This map is compared with the reference efficiency map defined in Section 3.1. To do this comparison, the structural similarity index SSIM [113] is used to compute the objective function. The SSIM index calculates the similarity degree between two different matrices, the matrices in this case are two torque-speed-efficiency maps. SSIM returns a normalized output within 0 and 1, being 0 the minimum and 1 the maximum similarity respectively. The optimization algorithm minimizes the objective function, i.e., $f = 1 - SSIM$ changing the geometrical parameters at each iteration.

5.2.1 PMSM Reference Torque-Speed-Efficiency Map

A PMSM reference torque-speed-efficiency map is defined as a first design step. The aim is to provide the motor performance for the application. The designer has full freedom to define the efficiency values and the distribution along the torque-speed map. This step is of major importance because the PMSM to be designed strictly depends on the efficiency map defined. The algorithm aims to achieve the motor characteristics which matches as much as possible to the defined performance.

5.2.2 Analytical Pre-Design and Geometry Construction

Once the torque-speed-efficiency map is defined, following the same procedure than with the Toyota Prius 2004 and Camry 2007, a seed geometry is needed to start the design-optimization process. This initial geometry is calculated using analytical equations and general design rules,

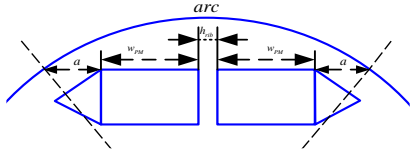
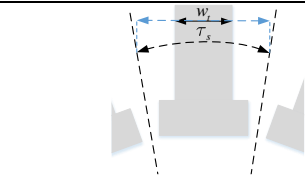
thus ensuring a solution nearby the optimum [114], [123]. Table 28 shows the design optimization geometric parameters.

Table 28: Design-optimization geometric parameters

Parameters	Information
d_{wire}	Diameter of the conductors [m]
D_{ir}	Inner diameter of the rotor [m]
D_{is}	Inner diameter of the stator [m]
D_{or}	Outer diameter of the rotor [m]
D_{os}	Outer diameter of the stator [m]
g	Length of the air gap [m]
h_{brg}	Height of the bridges in the rotor [m]
h_{PM}	Height of the permanent magnets [m]
h_{rib}	Height of the rotor ribs [m]
h_{so}	Height of the slots opening [m]
h_{sy}	Height of the stator yoke [m]
h_t	Height of the tooth [m]
L	Length of the stack laminations [m]
N_{ph}	Turns per phase [-]
w_{brg}	Width of the rotor bridges [m]
w_{PM}	Width of the permanent magnets [m]
w_{so}	Width of the slot openings [m]
w_t	Width of the tooth [m]
w_{web}	Width of the rotor web [m]

A total of 19 parameters are optimized. Due to the defined equality and inequality rules (see Table 29), the number of parameters is reduced to 16.

Table 29: PMSM geometric rules

Linear Equality Rules	
The inner stator diameter must be equal to the outer rotor diameter plus two times the airgap length	$D_{or} + 2 \cdot g = D_{is}$
The inner stator diameter plus two times the tooth height plus two times the stator yoke height must be equal to the outer stator diameter	$D_{is} + 2 \cdot h_t + 2 \cdot h_{sy} = D_{os}$
Linear Inequality Rules	
The outer rotor diameter has to be always bigger than the inner rotor diameter.	$D_{or} > D_{ir}$
The outer stator diameter has to be always bigger than the inner stator diameter.	$D_{os} > D_{is}$
The height of the stator tooth is bigger than the slot opening height.	$h_t > h_{so}$
The rotor bridge and rib height will never be smaller than 0.5 mm to guarantee physical robustness.	$1\text{mm} \geq h_{brg} \geq 0.5\text{mm}$ $1\text{mm} \geq h_{rib} \geq 0.5\text{mm}$
Stack length L has to be greater than zero and always as maximum as D_{os} .	$0 < L \leq D_{os}$
Non-Linear Equality Rules	
The permanent magnet width plus the rib height plus the rotor bridges projected in the same line have to be equal than the projection of the pith arc.	
Non-Linear Inequality Rules	
The stator tooth width has to be always smaller than slot pith arc projected in the line. The values are taken for the mid-height of the tooth.	
The ratio between the wire section taking into account the isolation times the number of wires corresponding per slot over the total slot section has to be less or equal than 0.5	

Once the geometric parameters are obtained, either the seed geometry or the geometry found during the optimization process, and the correctness of the geometry is verified, the geometry can be built into the FEA environment.

Table 30 shows the materials used in the PMSM. The $B-H$ curve of the laminations is included in the COMSOL Multiphysics® FEA software.

Table 30: Design optimization materials

Stator laminations	M400-50A
Rotor laminations	M400-50A
Permanent magnets	Nd35H
Winding	Copper

Some parameters are settled considering manufacturing reliability and simplicity. These parameters are exposed in Table 31.

Table 31: Design optimization fixed parameters

Number of pole pairs	3
Number of stator slots	9
Winding typology	Concentrated
Number of layers	2
Rotor topology	Interior PMSM

5.2.3 PMSM design optimization results

The PMSM design-optimization algorithm is validated for a specific hydraulic application.

Figure 40 shows the experimental hydraulic torque-speed-efficiency map of the water pump application. This map, as explained in the hypothesis and introduction sections, is extracted using equations (1) and (2).

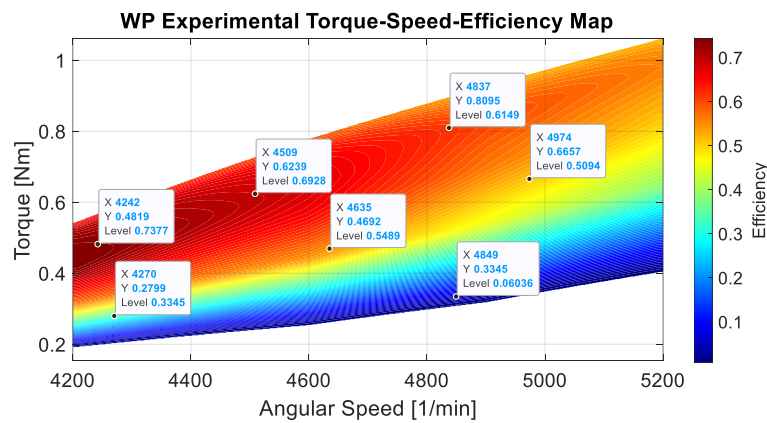


Figure 40: Water pump experimental torque-speed-efficiency map

Table 32 summarizes the operational points of the water pump efficiency map highlighted in Figure 40.

Table 32: Water pump efficiency map data labels

Angular velocity (1/min)	Torque (Nm)	Efficiency (p.u.)
4242	0.4819	0.7377
4270	0.2799	0.3345
4509	0.6239	0.6928
4635	0.4692	0.5489
4849	0.3345	0.0603
4837	0.0895	0.6149
4974	0.6657	0.5094
5158	0.9861	0.5606

5.2.4 Reference PMSM torque-speed-efficiency map

Once the hydraulic torque-speed-efficiency map is known, the PMSM reference efficiency map distribution is designed. In this study, five initial torque-speed-efficiency points of the WP-PMSM system are imposed. Table 33 shows the two imposed system efficiencies.

Table 33: Reference efficiency distribution levels

Angular velocity (1/min)	Torque (Nm)	System Efficiency (p.u.)	WP Efficiency (p.u.)	PMSM Efficiency (p.u.)
5200	1.06	0.43	0.512	0.84
5100	1.00	0.45	0.542	0.83
5000	0.90	0.48	0.578	0.83
4900	0.80	0.49	0.598	0.82
4700	0.70	0.50	0.626	0.80

The first requirement is to have a system efficiency of 0.5 at 4700 rpm and 0.7 Nm. The second requirement is to accomplish with the IE4 PMSM standard [124] efficiency at 5200 rpm and 1.06 Nm, leading to a system efficiency of 0.43. The other operational points are interpolated. It results in four levels of PMSM efficiency, i.e., 0.84, 0.83, 0.82 and 0.80 respectively.

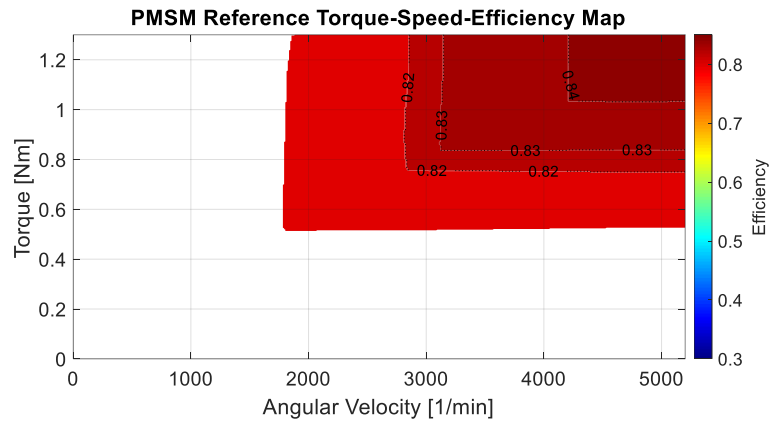
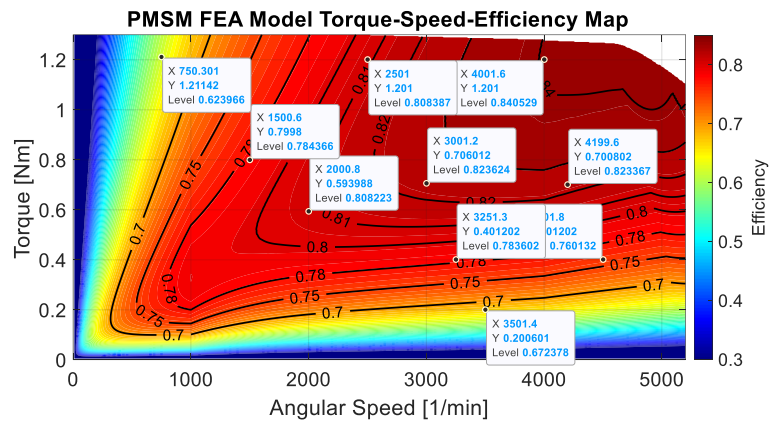


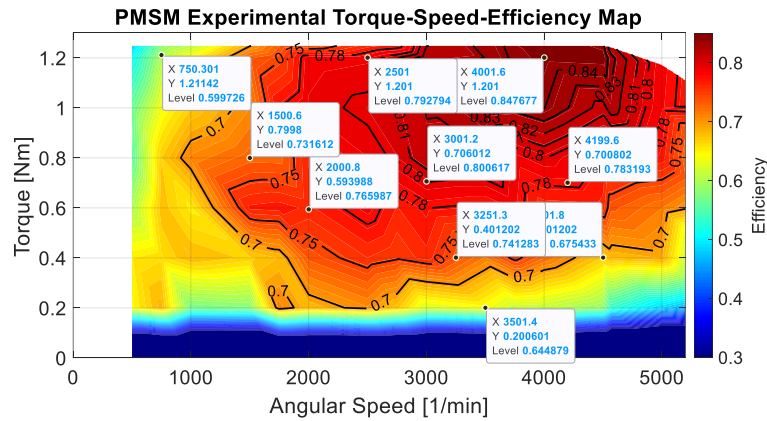
Figure 41: PMSM design optimization reference torque-speed-efficiency map

5.2.5 PMSM torque-speed-efficiency map

A PMSM is designed applying the design optimization algorithm introduced in this section starting from the torque-speed-efficiency map defined in Figure 41. Once designed the motor is manufactured and tested to experimentally validate the torque-speed-efficiency map.



(a)



(b)

Figure 42: PMSM torque-speed-efficiency map with design optimization FEA model (a) and experimental test (b)

The torque-speed-efficiency maps shown in Figure 42 have high degree of similarity.

Table 34: PMSM torque-speed-efficiency map

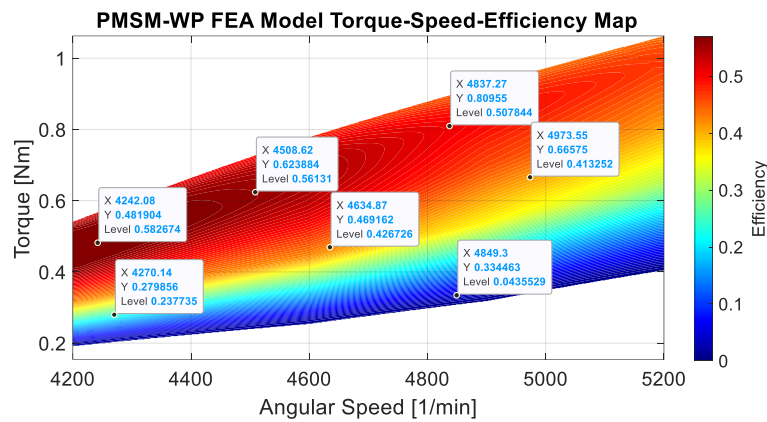
Angular velocity (1/min)	Torque (Nm)	PMSM Model Efficiency (p.u.)	PMSM Experimental Efficiency (p.u.)
750.3	1.2110	0.6240	0.5997
1501	0.7998	0.7844	0.7316
2001	0.5940	0.8082	0.7660
2501	1.2010	0.8084	0.7928
3001	0.7060	0.8236	0.8006
3251	0.4012	0.7836	0.7413
3501	0.2006	0.6724	0.6449
4002	1.2010	0.8405	0.8477
4200	0.7008	0.8234	0.7832
4502	0.4012	0.7601	0.6754

The SSIM between reference and the design optimization FEA algorithm torque-speed-efficiency map is 0.983. That means that the algorithm converges with a relative error of 1.7 %. The SSIM between design optimization FEA algorithm and experimental maps is 0.96, therefore the relative error between both maps is 4%.

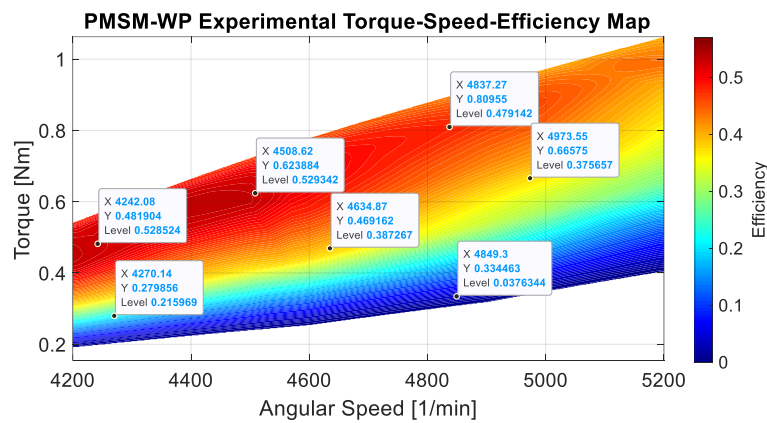
5.2.6 Torque-speed-efficiency map of the system

System (PMSM-WP) efficiency map obtained with design-optimization FEA model can be compared with the experimental one. Figure 43 (a) and (b) show the system (PMSM-WP) torque-

speed-efficiency map achieved through the design-optimization model and the one obtained through experimental validation respectively.



(a)



(b)

Figure 43: PMSM-WP FEA torque-speed-efficiency map (a) design optimization FEA model (b) experimental

The SSIM between both maps is 0.99, i.e., the FEA model and experimental system torque-speed-efficiency maps have a relative error of 1%.

Table 35 shows the data labels of Figure 43, which are the efficiency values for different operating conditions. Analogously, Table 36 shows the comparison against the reference torque-speed-efficiency targets.

Analyzing the experimental values, it is observed an overall efficiency decrement for the experimental values. This results deviation shows the importance of taking into account other parameters when designing PMSMs, such as the mechanical tolerances, increment of iron losses due the manufacturing process or changes in the winding resistance, among others. Besides this,

the absolute errors remain low enough, i.e., around 2% of the rated power (19.6 W, 14.6 W, 14.8 W, 12.4 W, 14 W) validating the design-optimization process.

Table 35: PMSM-WP system torque-speed efficiency map values comparison

Angular velocity (1/min)	Torque (Nm)	Hydraulic-PMSM Model Efficiency (p.u.)	Hydraulic-PMSM Experimental Efficiency (p.u.)
4242	0.4819	0.5827	0.5285
4270	0.2799	0.2377	0.2160
4509	0.6239	0.5613	0.5293
4635	0.4692	0.4267	0.3873
4849	0.3345	0.0436	0.0376
4837	0.0895	0.5078	0.4791
4974	0.6657	0.4133	0.3757
5158	0.9861	0.4683	0.4375

Table 36: PMSM-WP efficiency labels comparison against reference map

Angular velocity (1/min)	Torque (Nm)	Efficiency (p.u.)	Efficiency Model (p.u.)	Efficiency Experimental (p.u.)
5200	1.06	0.43	0.4306	0.3967
5100	1.00	0.45	0.4534	0.4261
5000	0.9	0.48	0.4875	0.4561
4900	0.8	0.49	0.4939	0.4638
4700	0.7	0.50	0.5302	0.4893

5.3 PMSM Characteristics

The characteristics of the PMSM are presented in this section. Some geometric variables are discussed, as well as the performance under rated conditions. Figure 44 shows the PMSM prototype and the PMSM-WP assembly.

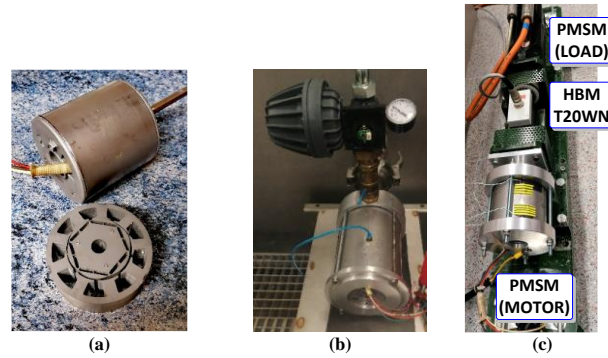


Figure 44: (a) PMSM prototype assembly (b) PMSM-WP system (c) PMSM test bench

The outer stator diameter D_{os} was fixed due a direct size limitation of the application. Based on this parameter restriction and the geometric rules, the design optimization algorithm finds the PMSM geometry attaining the performance defined by the designer. Table 37 summarizes the PMSM geometric variables.

Table 37: PMSM geometry values

Geometry Parameter	Values
g [mm]	0.29
D_{or} [mm]	54
D_{os} [mm]	90
L [mm]	30
h_{PM} [mm]	2.7
N_{ph}	210
d_{wire} [mm]	0.6

Table 38 summarizes the general characteristics of the PMSM.

Table 38: PMSM characteristics

Characteristics	Value
Number of phases	3
Rated power [W]	585
Rated Voltage [V_{RMS}]	200
Rated Current [I_{RMS}]	2
Rated Torque [N·m]	1.24
Rated Speed [rpm]	4501
Rated Efficiency [%]	84.2
Pole Pairs	3
Number of Slots	9
d-axis Inductance L_d [mH]	4.2
q-axis Inductances L_q [mH]	11.2

As shown in Table 38, the rated power of the motor is 585 W. Considering the IEC 60034-30-1 standard for electrical machines, the premium efficiency class (IE4) for machines with rated power of 600 W is 84 %. Therefore, the PMSM designed by means of the design-optimization algorithm fulfills the requirements of the premium efficiency standard.

Figure 45 shows the experimental setup used to validate the PMSM performance.

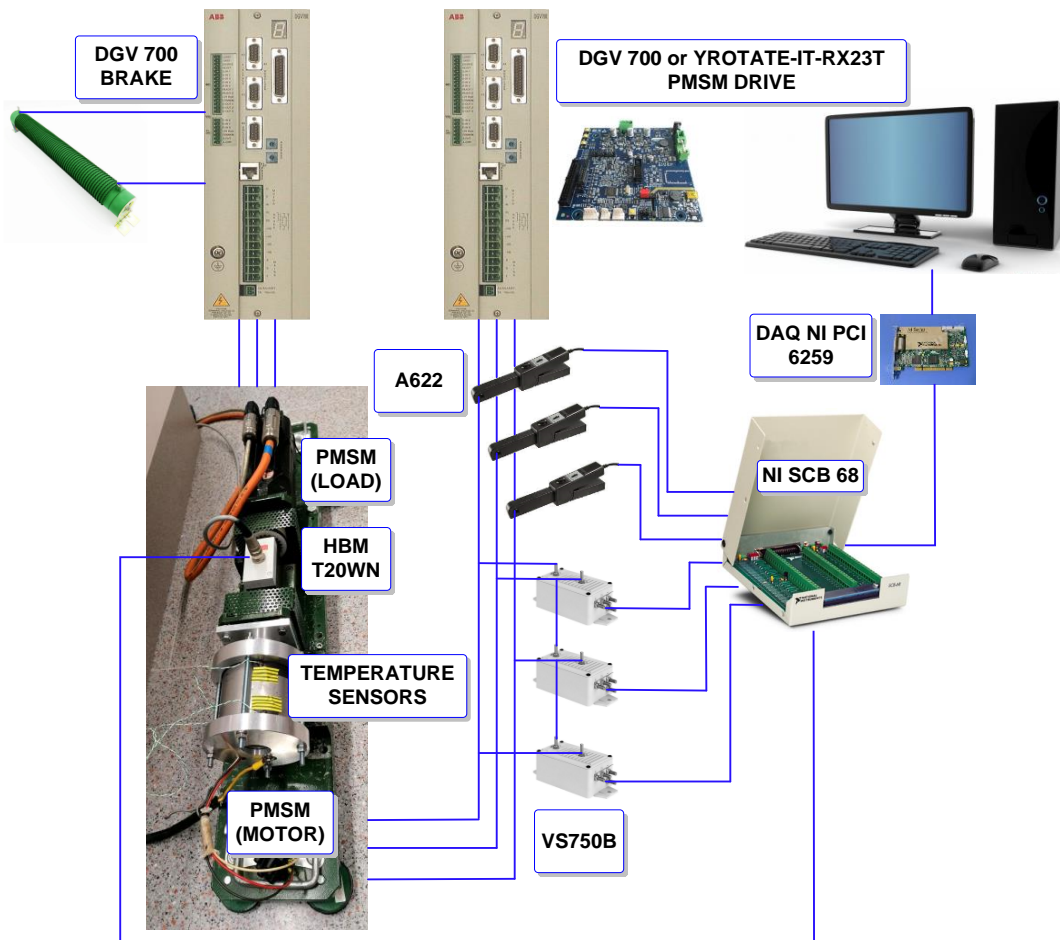
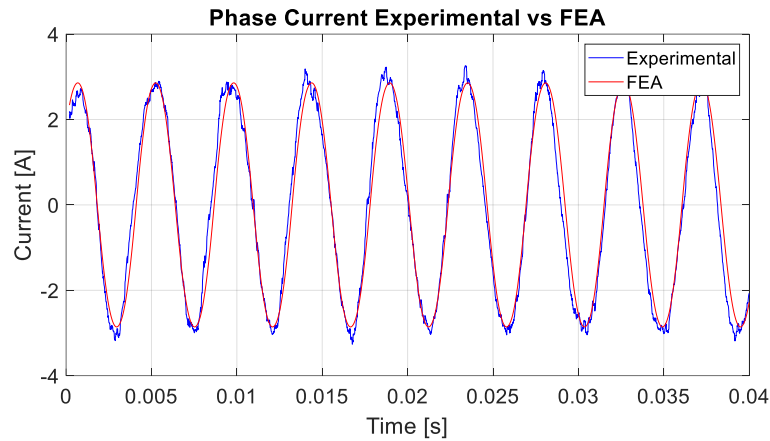


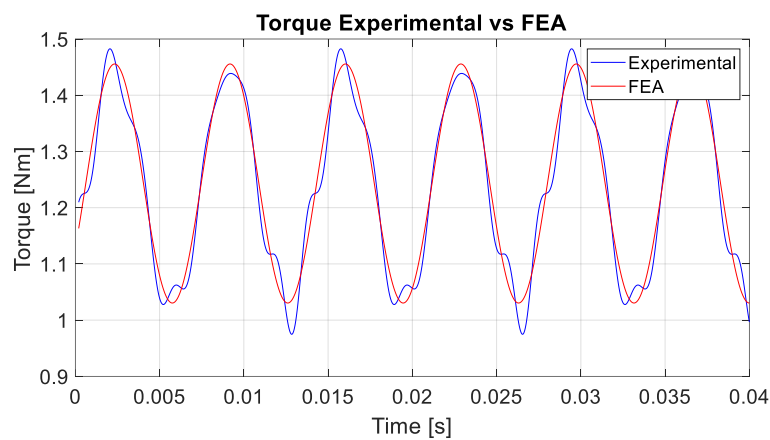
Figure 45: PMSM experimental setup for evaluating motor performance

5.4 PMSM validation by means of Time Dependent FEA Validation

Time-dependent FEA study is performed to validate the PMSM design under rated conditions. Results are compared against experimental acquisitions. Time-dependent FEA simulation is performed using 200 V_{RMS} pure sinusoidal voltage sources. The same operational point is evaluated using the RENESAS YROTATE-IT-RX32T converter, which applies sinusoidal pulse width modulation (SPWM). Figure 46 shows the time evolution of the phase current and mechanical torque.



(a)



(b)

Figure 46: (a) PMSM phase current at rated conditions experimental versus FEA (b) Torque at rated conditions experimental versus FEA

Figure 46 (a) shows the experimental and FEA time evolution of the experimental and FEA phase currents, respectively. The experimental acquisition includes winding unbalance effects. The RMS values of the experimental and FEA currents are 2.09 and 2.02 A, respectively. Analogously Figure 46 (b) shows the experimental and FEA torque waveform. The difference observed is mainly because the torque transducer is detecting the torque ripple of the PMSM as well as the torque ripple of the load PMSM, which adds some distortion. The mean experimental and FEA torques are 1.237 and 1.240 Nm, respectively.

5.5 Optimization Convergence and Computational Burden

Target completion for optimization convergence is 2% using the structural similarity index SSIM, therefore the objective function is $f_{obj} = 1 - \text{SSIM} = 0.02$. The *Patternsearch* optimization solver

from MATLAB® is used. The design optimization algorithm converges with a relative difference of 1.7%, thus accomplishing the defined target value.

PMSM design-optimization process required 4 days and 8 hours with an Intel® Core™ i9-7940X 3.10 GHz processor with 64 GB of RAM memory. Every optimization iteration required between 24-40 seconds, being strictly dependent on the iron saturation. To limit the design-optimization time, the number of optimization iterations were limited to 10000. The time required to design the PMSM is affordable and avoids manufacturing costs, saving time and resources.

5.6 PMSM design and optimization methodology. Conclusions

A design-optimization methodology to design and optimize PMSMs has been developed. The core idea of the process starts by defining the desired torque-speed-efficiency map by adapting its performance to the hydraulic characteristics of a specific WP application. It allows the designer to have full freedom to define the efficiency levels and distribution along the torque-speed map, including implicitly the distribution of power losses and power rating. The algorithm calculates the PMSM characteristics matching the required performance defined by the designer at the beginning of the design process. The methodology is validated by designing and testing a PMSM adapted to a water pumping application. Two main points of the whole system are designed according to the initial specifications. The values imposed by the designer are the torque, speed and system efficiency. After locating these main conditions, extra operating points were defined in order to increase the resolution of the objective torque-speed-efficiency map. By knowing the reference map, the design-optimization process starts. The PMSM was designed using the methodology proposed, the torque-speed-efficiency map obtained, and the efficiency targets were attained for the torque-speed-area, The SSIM between the reference and the design optimization map was 0.983, thus the algorithm converges with 1.7% of similarity error. Next, the prototype was manufactured and tested. The torque-speed-efficiency map obtained shows high fidelity between the FEA and experimental values. The relative similarity error between both maps is 4 %. Once the PMSM performance was validated, the system efficiency was compared with FEA and experimental values, obtaining a relative error of 1% in the target efficiencies.

6. PMSM Parameter Estimation

During last decades, special attention has been put in parameter estimation methods for electrical machines, today becoming an active topic. Such methods allow a better characterization, thus enabling to improve motor design and control. PMSMs have been of special interest with respect other electrical machines due to their superior capabilities, such as torque density, position precision, high efficiency, etc.

This chapter presents a novel PMSM parameter estimation method. The PMSM designed through the design-optimization methodology is used. First, the method characterizes the motor parameters by considering its performance on the entire torque-speed range, thus, allowing to find the parameter variations as a function of the load conditions. Moreover, as a main novelty, the identification method finds the values of the d - q inductances from the differential power factor due to the harmonic distortion. This method calculates the d - q inductances as a function of the space vector current and angle, thus providing superior accuracy compared to most of the approaches found in the literature. The proposed method finds the vector magnitudes and angles without requiring any position sensor, motor geometry information or prior knowledge of the applied FOC strategy. This approach uses a d - q electrical model considering the harmonics of the electrical magnitudes, and does not apply any optimization algorithm for the identification, thus reducing computational requirements. By considering the harmonics, the d - q inductances are characterized, allowing an enhanced characterization of the machine.

The method starts from electrical and mechanical measurements (voltages, currents, torque and speed), the d - q inductances of the PMSMs are inferred in the entire torque-speed map as a function of the operating point. These parameters are usually obtained by means of FEM models, so they are not directly measured. In case of being measured, a test bench equipped with an accurate position sensor on the motor shaft is required, thus carrying out a set of tests for each rotor angular position. The method presented in this research avoids the need for such a position sensor.

The proposed method is first validated experimentally by comparing the d - q current space vector against that acquired by using the position provided by a resolver connected to an ABB DGV700 converter that applies a 90° current control without flux weakening capability. The method is further validated by using the designed PMSM connected to a Renessa's YROTATE-IT-RX23T motor control platform, which applies a sensorless 90° current control with flux weakening capability. The d - q inductances are validated for all experimental operational points.

This chapter is divided in five sections. First section 6.1 overviews the PMSM parameter estimation methodology, section 6.2 introduces the PMSM testing procedure detailing the experimental setup and measurement issues, section 6.3 details the parameter estimation algorithm, section 6.4 exposes the validation results and section 6.5 exposes the conclusions.

Contents

- 6.1 PMSM parameter estimation methodology overview
- 6.2 PMSM testing procedure
- 6.3 Parameter estimation algorithm to identify inductances and FOC strategy
- 6.4 Parameter estimation results
- 6.5 Parameter estimation methodology conclusions

Nomenclature

A_{DAQ}	DAQ accuracy [V]
A_t	Total measurement accuracy [V]
A_{Trans}	Transducer accuracy [V]
$\cos(\varphi)$	Power factor [-]
$e_{\text{pm-1st}}$	1 st Harmonic permanent magnet stator back-electromotive force [V]
E_s	Stator back-electromotive force [V]
I_{abc}	Stator phase currents [A]
i_d	Direct axis current [A]
i_q	Quadrature axis current [A]
i_s	Current space vector [A]
$i_{s\text{-nth}}$	n-th harmonic of the current space vector [A]
I_s	Rated stator current [A]
L_d	Direct axis inductance [H]
L_q	Quadrature axis inductance [H]
m	Phases number [-]
n	Rotor angular speed [rpm]
n_{max}	Maximum rotor angular speed [rpm]
p	Pairs of poles [-]
$P_{\text{Fe-mec}}$	Iron and mechanical losses sum [W]
P_{Rs}	Copper losses [W]
P_U	Useful mechanical power [W]
q	Number of slots per pole and phase [-]
R_{Fe}	Iron resistance [Ω]
R_s	Stator windings per phase resistance [Ω]
R_{so}	Phase stator resistance at ambient temperature [Ω]
T	Output mechanical torque [N·m]
T_{amb}	Ambient temperature [$^{\circ}\text{C}$]
T_{w1}	Winding temperature (front coil head) [$^{\circ}\text{C}$]
T_{w2}	Winding temperature (rear coil head) [$^{\circ}\text{C}$]
U_{abc}	Stator phase voltages [V]
u_d	Direct stator voltage [V]
u_q	Quadrature stator voltage [V]

\mathbf{u}_s	Voltage space vector [V]
\mathbf{u}_{s-nth}	n-th harmonic of the stator voltage space vector [V]
$\mathbf{u}(\mathbf{x}_i)$	Standard uncertainty
$\mathbf{u}_c(\mathbf{y})$	Combined standard uncertainty
$\mathbf{u}^2(\mathbf{x}_i)$	Estimated variance
$\mathbf{u}_c^2(\mathbf{y})$	Combined estimated variance
\mathbf{U}_{dc}	Voltage of the DC bus [V]
\mathbf{U}_s	Rated stator voltage [V]
α	Angle between the 1 st harmonic of the stator flux linkage and the current [rad]
β	Angle between the 1 st harmonic of the stator voltage and the back-electromotive force
η	Energy efficiency [p.u.]
θ_e	Electrical angular position [rad]
θ_{is-1st}	First harmonic current space vector angle [rad]
θ_m	Mechanical angular position [rad]
θ_{res}	Resolver angular position [rad]
θ_{us-1st}	First harmonic voltage space vector angle [rad]
φ	First harmonic power factor angle [rad]
ω_m	Electrical angular speed [rad/s]
Ψ_{abc}	Stator flux linkage [V·s/rad]
Ψ_d	Direct axis flux linkage [V·s/rad]
Ψ_{pm}	Permanent magnets flux linkage [V·s/rad]
Ψ_{pm-1st}	1 st harmonic permanent magnets flux linkage[V·s/rad]
Ψ_q	Quadrature axis flux linkage [V·s/rad]
Ψ_{s-1st}	1 st harmonic stator flux linkage [V·s/rad]

6.1 PMSM parameter estimation methodology overview

This subsection shows the parameter estimation methodology. Figure 47 shows the process diagram, which is divided in two main stages, i.e., the experimental tests and the parameter estimation stage. The parameters to be known before starting the identification are the rated magnitudes, such as the line voltage, phase current, rated speed and maximum speed, rated torque, number of phases and number of poles. All this data is usually found in the motor nameplate provided by the manufacturer. Next, some optional tests can be performed to obtain the permanent magnet flux linkage and phase resistance if these values require to be updated. Then, these values are taken as seed values for the solution, and they will be corrected when identifying the PMSM parameters. After this, the motor is tested and the phase currents, line voltages, load torque, angular speed, resolver or encoder position if available and the winding temperature are acquired. Finally, the parameter estimation algorithm is applied to identify the FOC strategy and the electromagnetic parameters over the whole torque-speed range.

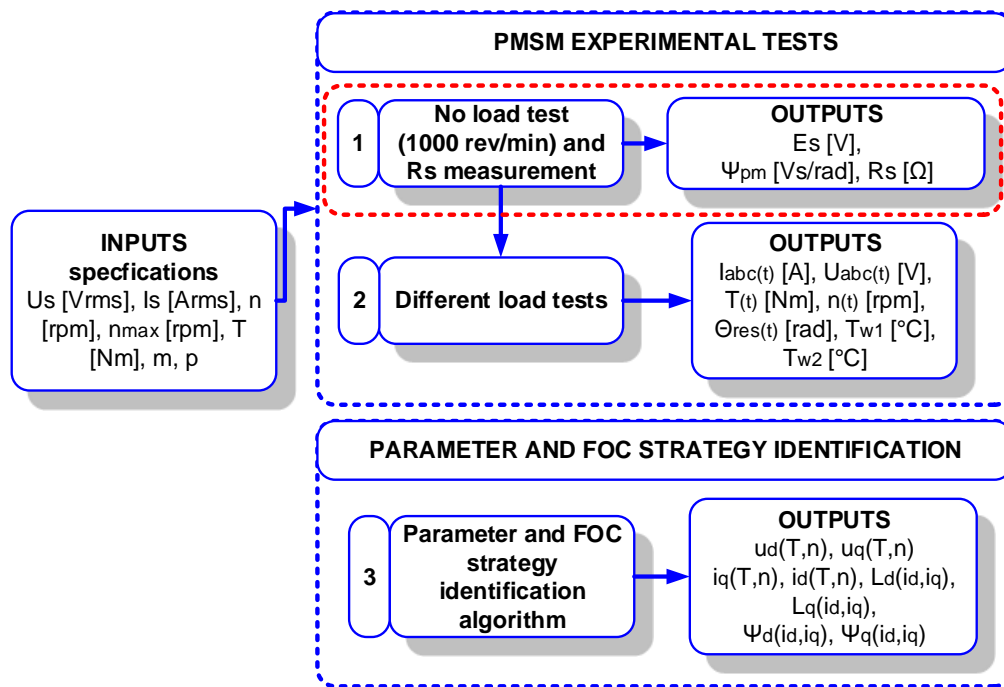


Figure 47: PMSM parameter estimation methodology overview

6.2 PMSM testing procedure

This subsection details the experimental procedure to extract the experimental data. Most of the input data are usually available in the motor nameplate. Some other parameters can be obtained

and updated, because they can change due to different reasons as tolerances, manufacturing process, aging or faults among others. Figure 48 summarizes the PMSM testing process.

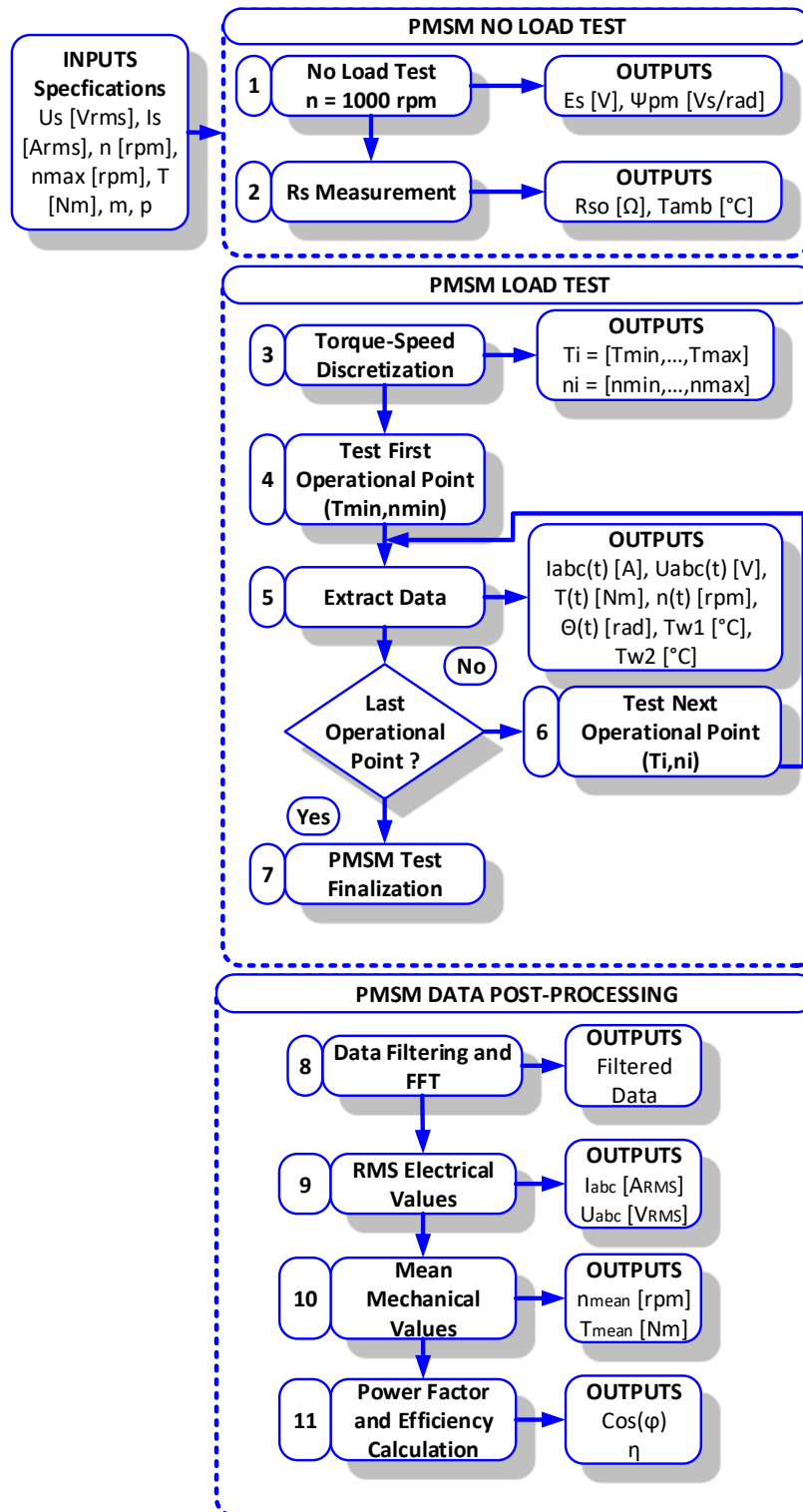


Figure 48: PMSM parameter estimation testing process

6.2.1 No load test for PMSM

The no load test is first performed at 1000 rpm to acquire the time dependent back-electromotive force (steps 1 and 2), and the harmonic components are extracted. The winding resistance is also measured at ambient temperature. These values are updated during the estimation process.

6.2.2 Load test for PMSM

The PMSM is connected to the load motor, which in this case is a SPMSM. The load test consists in testing different operating points within the torque-speed plane (steps 3 to 7).

6.2.2.1 Torque-speed discretization

To test the PMSM, the torque-speed plane is discretized considering the rated torque and the rated and maximum angular speeds. The maximum power envelope is considered to limit the maximum speed for each torque value.

6.2.2.2 Operating point test and data acquisition

Once discretized the torque-speed map, time-dependent measurements are performed. Data includes phase currents, line voltages, dynamic torque, dynamic angular speed, motor resolver position and winding temperature. On the other hand, if a position sensor is available, it is used to validate the accuracy of the current space vector angle estimation.

Table 39 shows the measurement and acquisition details for the instrumentation selected.

Table 39: Measurement and acquisition devices details

Magnitude	Sampling Frequency	Number of samples	DAQ Input Range	DAQ Sensitivity	DAQ Accuracy	Transducer Accuracy
Angular speed sensor	200 kS/s	200 kS	±5 V	56 μV	1.01 mV	0.15 V
Current sensors			±1 V	12.8 μV	0.22 mV	5 mV
Torque sensor			±10 V	112 μV	1.92 mV	0.02 V
Voltage sensors			±5 V	56 μV	1.01 mV	3 mV
Temperature sensors	1 S/s	1 S	±1 V	12.8 μV	0.22 mV	88 μV

6.2.3 PMSM data processing

The data acquired is post-processed (steps 8 to 11). This stage includes different steps which are described below.

6.2.3.1 Data filtering and calculations

Table 39 indicates the sampling frequency (200 kS/s) during 1 second for each operational point. The PMSMs has six pole extensions, its maximum angular speed is 6000 rpm, so the maximum fundamental harmonic frequency is 300 Hz, corresponding to 66 samples per period, thus this system allows acquiring up to the 83th harmonic. The data is filtered by using a first-order low-pass filter with a stopband attenuation of 60 dB. The cut-off frequency is set to the frequency of the 7th electrical harmonic, the highest relevant harmonic for a proper operation.

6.2.3.2 Fast Fourier Transformation (FFT)

After the data is acquired and filtered, a harmonic analysis is performed extracting the amplitude and phase of the first, third and fifth harmonics.

6.2.4 Experimental setup

Figure 49 exposes the experimental setup used to apply the parameter estimation methodology. It is worth to mention that this configuration is the same as the experimental setup used to evaluate the motor performance following the standard procedure. Therefore, this method is aimed to complement and expand the measured parameters.

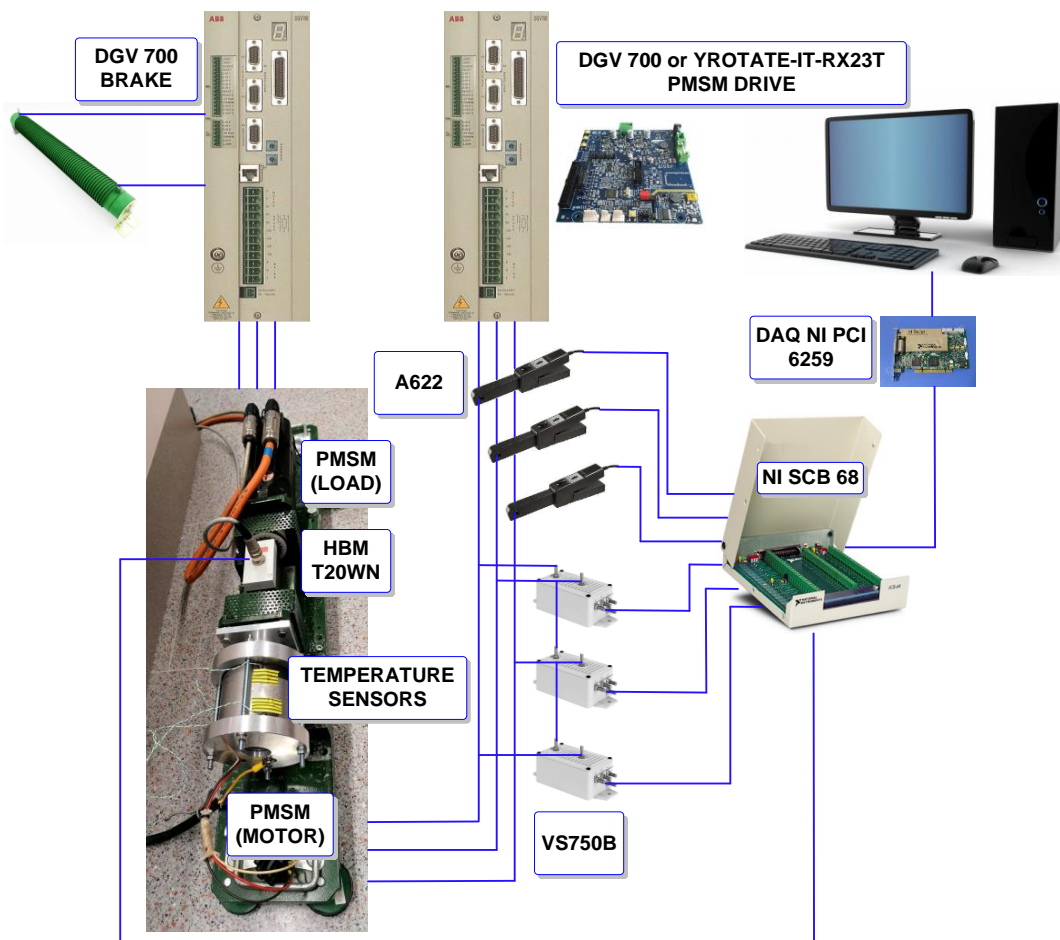


Figure 49: PMSM setup for parameter estimation

Table 40 summarizes the instrumentation used in the experimental part.

Table 40: PMSM parameter estimation instrumentation

Converter	ABB - DGV 700 / YROTATE-IT-RX23T
Angular speed sensor	ABB-DGV700 (A I/O: $\pm 15V$, 1%)
Current sensors	Tektronix A622 (10 mV/A o 100 mV/A, sensitivity: 0.06 mV/A)
Torque sensor	HBM T20WN/20NM (Torque: 0-10 V, ± 0.2 %)
Voltage sensors	ABB VS750B (750 V, 0.3-0.9 %)
Temperature sensors	Type K Thermocouple, (0.75 %)
Data acquisition device	DAQ NI PCI-6259 - NI SCB 68 ($\pm 5V$, 56 μV), 16 bits
Acquisition software	Python

6.2.5 Standard uncertainty and combined standard uncertainty analysis

Standard uncertainty analysis is performed in this section. To perform the analysis, the accuracy of each transducer is considered to be overlapped with the accuracy of the DAQ. To illustrate that, Figure 50 shows conceptually the accuracy disposition.

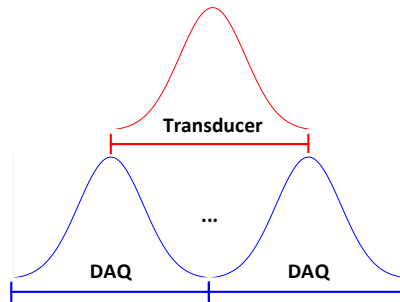


Figure 50: DAQ and transducer accuracy overlap

Making the above assumption the worst case scenario is being considered, therefore the total accuracy is the sum of accuracies.

$$A_i = A_{Trans} + A_{DAQ} \quad (102)$$

Considering a coverage factor of 3, the standard uncertainty is calculated as,

$$u(x_i) = \frac{A_i}{3} \quad (103)$$

The estimated variance is as,

$$u^2(x_i) = (u(x_i))^2 \quad (104)$$

The combined variance of a function of interest is defined as,

$$u_c^2(y) = \sum_{i=1}^N \left[\frac{\partial f}{\partial x_i} \right]^2 \cdot u^2(x_i) \quad (105)$$

The combined standard uncertainty is used to calculate the accuracy of estimated values, being the square root of the combined variance,

$$u_c(y) = \sqrt{u_c^2(y)} \quad (106)$$

Table 41 shows the standard uncertainty for the measurement devices considering its overlapping region with DAQ accuracy.

Table 41: Standard uncertainty considering the measurement devices

Magnitude	DAQ Accuracy	Transducer Accuracy	Total Accuracy	Standard Uncertainty (Acquisition magnitude)	Standard Uncertainty (Physical magnitude)
Angular speed sensor	1.01 mV	0.15 V	151 mV	50.30 mV	20.12 rpm
Current sensors	0.22 mV	5 mV	5.22 mV	1.74 mV	0.0087 A
Torque sensor	1.92 mV	0.02 V	21.9 mV	7.30 mV	0.0146 Nm
Voltage sensors	1.01 mV	3 mV	3.01 mV	1.003 mV	0.15 V
Temperature sensors	0.22 mV	88 μ V	0.31 mV	0.103 mV	0.18 $^{\circ}$ C

6.3 Parameter estimation algorithm to identify inductances and FOC strategy

This subsection details the parameter estimation algorithm aimed to identify the PMSM inductances over d-q currents and the FOC strategy for each operational point.

6.3.1 Space vector current discretization and harmonic decomposition

The first step is the discretization of the current space vector. The discretization is carried out within the motoring quadrant, which for PMSMs is the second quadrant. Considering this discretization together with the available data, it is possible to extract the magnitudes to identify by applying some calculus.

Figure 51 shows a generic *d-q* vector diagram for PMSM, where can be seen magnitudes as voltage, currents and flux linkages. The harmonic components of voltages and currents are determined, i.e., the fundamental frequency, amplitudes and phase angles. As explained later, the third and fifth harmonics are used for identification of the inductances for all operating points.

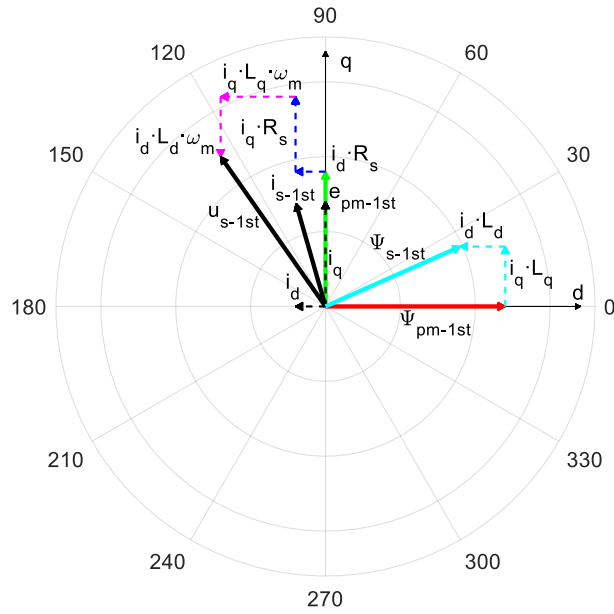


Figure 51: PMSM vector diagram of the fundamental magnitudes.

Figure 52 shows the third and fifth current harmonic vector diagram. Therefore, when identifying the d - q currents, it is necessary to decouple the harmonic components, as well as for the voltage and flux linkage vectors.

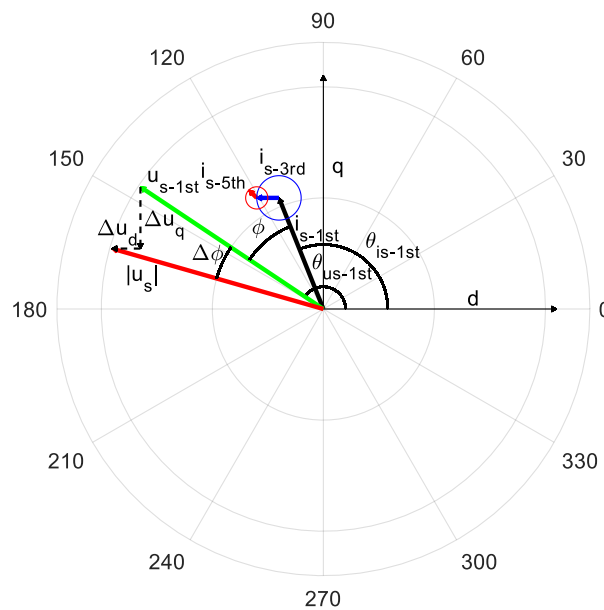


Figure 52: PMSM vector diagram including the harmonic vector representation.

6.3.2 Winding resistance adjustment, iron resistance and stator flux linkage calculation

Knowing the fundamental electrical magnitudes, the winding resistance is corrected according to the acquired temperature.

$$R_s = R_{s_0} \cdot [1 + \alpha_{Cu} \cdot (T_w - T_{amb})] \quad (107)$$

The stator resistance power losses are calculated considering the contribution of the third and fifth harmonics.

$$P_{R_s} = \frac{m}{2} \cdot (i_{s-1st}^2 + i_{s-3rd}^2 + i_{s-5th}^2) \cdot R_s \quad (108)$$

From the power balance, the iron and mechanical power losses in all operational points are determined.

$$P_{Fe-mec} = \left(\frac{P_U}{\eta} - P_U - P_{R_s} \right) \quad (109)$$

The iron and mechanical losses are represented as a parallel resistance in the d - q electrical model,

$$R_{Fe-mec} = \frac{m}{2 \cdot P_{Fe-mec}} \cdot \left((u_{s-1st} - R_s \cdot i_{s-1st})^2 + (u_{s-3rd} - R_s \cdot i_{s-3rd})^2 + (u_{s-5th} - R_s \cdot i_{s-5th})^2 \right) \quad (110)$$

R_s , u_{s-1st} , i_{s-1st} , u_{s-3rd} , i_{s-3rd} , u_{s-5th} and i_{s-5th} are obtained by averaging the magnitudes of each of the m phases. Voltages and currents are expressed in peak values.

The first harmonic of the back electromotive force is as,

$$e_{s-1st} = u_{s-1st} - i_{s-1st} \cdot R_s \quad (111)$$

Once the back electromotive force and the electrical angular velocity are known, the absolute stator flux linkage can be determined as,

$$\psi_{s-1st} = e_{s-1st} / \omega_m \quad (112)$$

6.3.3 Differential voltage due to the current harmonics and angles determination

After having the harmonic decomposition, the phase angles for every component are obtained.

The first harmonic power factor averaged over m phases is calculated as,

$$\cos \phi = \frac{1}{m} \cdot \sum_{i=1}^m \cos(\theta_{u_{s-1st,i}} - \theta_{i_{s-1st,i}}) \quad (113)$$

$\theta_{u_{s-1st,i}}$ and $\theta_{i_{s-1st,i}}$ are the angles of voltage and current vectors respectively for phase i .

Considering the harmonic contribution, the total power factor is as,

$$\cos(\phi + \Delta\phi) = \frac{1}{m} \sum_{i=1}^m \frac{\text{mean}(u_i(t) \cdot i_i(t))}{U_{i-RMS} \cdot I_{i-RMS}} \quad (114)$$

The differential power factor angle $\Delta\phi$ is calculated as,

$$\Delta\phi = \frac{1}{m} \sum_{i=1}^m (\theta_{u_s,i} - \theta_{u_{s-1st,i}}) \quad (115)$$

The angle between i_{s-1st} and Ψ_{s-1st} is calculated in this stage. Figure 53 shows the angles which will remain fixed during the identification process. ϕ is the angle between the first harmonic of the stator current and voltage, β is the angle between the first harmonic of the stator voltage and the back-electromotive force and α the angle between the first harmonic of the stator flux linkage and current. Using the sinus theorem, angle β is calculated as,

$$\sin \beta = \sin \phi \cdot \frac{i_{s-1st} \cdot R_s}{e_{s-1st}} \quad (116)$$

The angle between the stator flux linkage and the current is,

$$\alpha = \frac{\pi}{2} - \beta - \phi \quad (117)$$

These angles fix the relative position of all space vectors, allowing only one degree of freedom when finding the control angle.

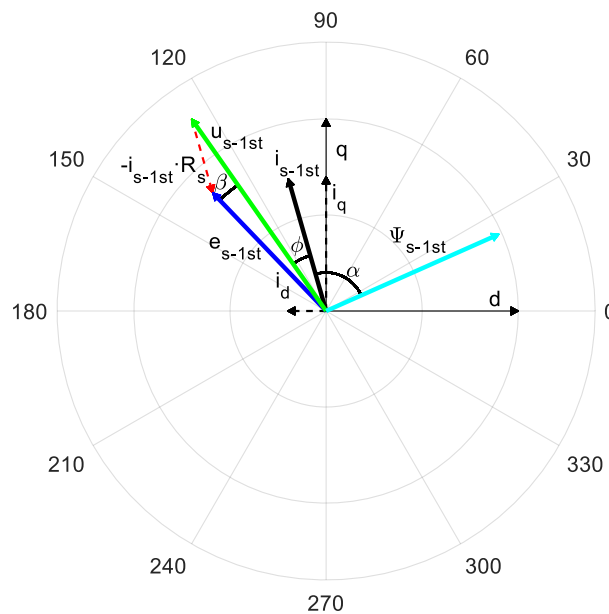


Figure 53: PMSM current, voltage and flux linkage 1st harmonic Blondel diagram

6.3.4 Inductance calculation

First, the current space vector is decomposed in the d - q plane.

$$\begin{cases} i_d = i_{s-1st} \cdot \cos(\theta_{i-1st}) \\ i_q = i_{s-1st} \cdot \sin(\theta_{i-1st}) \end{cases} \quad (118)$$

Next, knowing the angle between the stator flux linkage and the current, the stator flux linkage is obtained as follows.

$$\begin{cases} \psi_d = \psi_{s-1st} \cdot \cos(\theta_{i-1st} - \alpha) \\ \psi_q = \psi_{s-1st} \cdot \sin(\theta_{i-1st} - \alpha) \end{cases} \quad (119)$$

Unstable values are obtained when calculating the inductance from the first current harmonic components. Critical values are reached when the d - q current has a small value, i.e., when the current angle is nearby the q -axis ($\theta_{is} \approx \pi/2$) or with the d -axis ($\theta_{is} \approx \pi$). An alternative way to calculate the d - q inductances is proposed in this thesis, which considers the third and fifth harmonics of the current and the differential power factor angle $\Delta\phi$.

The differential d - q voltages are calculated as,

$$\begin{cases} \Delta u_d = |u_s| \cdot \cos(\theta_{i-1st} + \phi + \Delta\phi) - u_{s-1st} \cdot \cos(\theta_{i-1st} + \phi) \\ \Delta u_q = |u_s| \cdot \sin(\theta_{i-1st} + \phi + \Delta\phi) - u_{s-1st} \cdot \sin(\theta_{i-1st} + \phi) \end{cases} \quad (120)$$

Next, the inductances using the methodology proposed in this thesis are calculated as,

$$\begin{cases} L_d = \frac{\Delta u_q + \Delta u_d}{\frac{\Delta u_d}{|\Delta u_d|} \cdot 2 \cdot (3 \cdot \omega_m \cdot i_{s-3rd} + 5 \cdot \omega_m \cdot i_{s-5th})} \\ L_q = \frac{\Delta u_q - \Delta u_d}{\frac{\Delta u_q}{|\Delta u_q|} \cdot 2 \cdot (3 \cdot \omega_m \cdot i_{s-3rd} + 5 \cdot \omega_m \cdot i_{s-5th})} \end{cases} \quad (121)$$

Once the d - q inductances are known, the d - q flux linkages are compared with the calculated ones.

$$\begin{cases} \psi_{d-calc} = \psi_{pm-1st} + L_d \cdot i_d \\ \psi_{q-calc} = L_q \cdot i_q \end{cases} \quad (122)$$

$$\begin{cases} \varepsilon_{\psi_d} = \frac{\psi_{d-calc} - \psi_d}{\psi_d} \\ \varepsilon_{\psi_q} = \frac{\psi_{q-calc} - \psi_q}{\psi_q} \end{cases} \quad \varepsilon_{\psi_s} = \frac{1}{2} \cdot \varepsilon_{\psi_d} + \frac{1}{2} \cdot \varepsilon_{\psi_q} \quad (123)$$

The angle θ_{is-1st} providing the minimum flux linkage error is considered as the nearest solution of the real control angle.

Once the optimal angle θ_{is-1st} is found, the first harmonic components are calculated and compared against experimental data.

$$\begin{cases} u_{d-calc} = R_s \cdot i_d - \omega_m \cdot \psi_q \\ u_{q-calc} = R_s \cdot i_q + \omega_m \cdot \psi_d \end{cases} \quad (124)$$

$$u_{s-calc} = \sqrt{u_{d-calc}^2 + u_{q-calc}^2} \quad (125)$$

The power factor is extracted from the d - q voltages and the current vector as,

$$\cos(\phi_{calc}) = \cos(\theta_{u_{s-calc-1st}} - \theta_{i_{s-1st}}) \quad (126)$$

The torque generating currents i_{od} and i_{oq} are calculated as,

$$\begin{cases} i_{od} = i_d + \frac{\omega_m \cdot \psi_q}{R_{Fe-mec}} \\ i_{oq} = i_q - \frac{\omega_m \cdot \psi_d}{R_{Fe-mec}} \end{cases} \quad (127)$$

Finally, the torque is calculated as,

$$T = \left(\frac{m}{2}\right) \cdot p \cdot (\psi_d \cdot i_{oq} - \psi_q \cdot i_{od}) \quad (128)$$

Relative errors are calculated as,

$$\begin{cases} \mathcal{E}_T = \frac{|T - T_{ref}|}{T_{ref}} \\ \mathcal{E}_{u_s} = \frac{|u_{s-calc} - u_{s-1st}|}{u_{s-1st}} \\ \mathcal{E}_{\cos(\rho)} = \frac{|\cos \phi_{calc} - \cos \phi|}{\cos \phi} \end{cases} \quad (129)$$

Figure 54 summarizes the parameter estimation algorithm to identify inductances and FOC strategy.

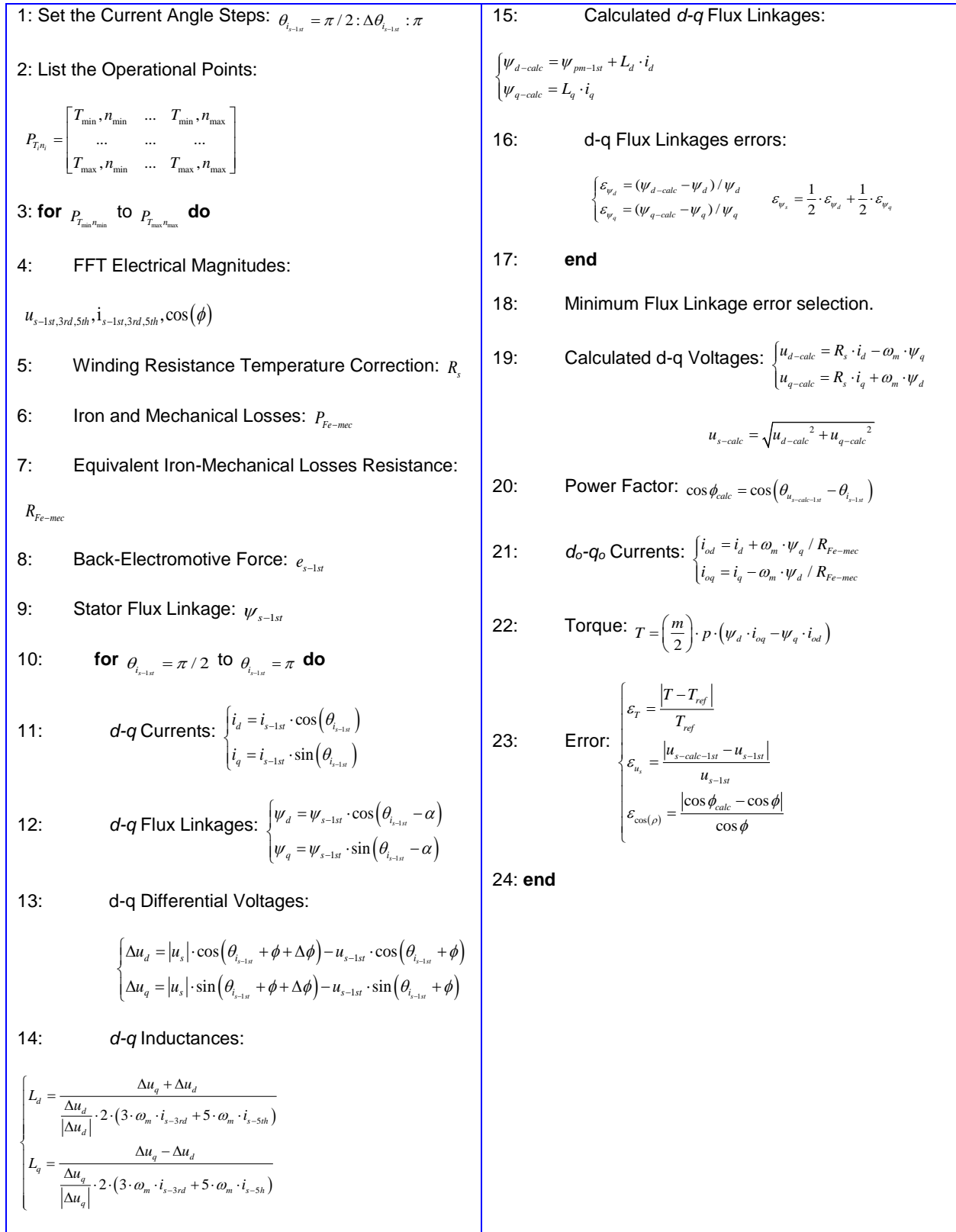


Figure 54: PMSM parameter estimation algorithm overview

6.4 Parameter estimation results

This subsection summarizes the results obtained using the parameter estimation. The method is validated at the first instance, using an ABB PMSM driven by a DGV700 ABB converter, which has a resolver, thus allowing to acquire the rotor position for validation purposes. The method is further validated using a PMSM from Midtal Talentos S.L driven by a RENESAS® sensorless FOC control platform YROTATE-IT-RX23T with flux weakening capability.

6.4.1 ABB PMSM

Table 42 summarizes the ABB PMSM characteristics.

Table 42: ABB PMSM characteristic

Manufacturer	ABB
Converter model	DGV 700
Rated Voltage [V_{RMS}]	380
Rated Current [A_{RMS}]	2.9
Rated Torque [N·m]	2.3
Rated Speed [1/min]	6000

The model is applied to the ABB PMSM. Figure 55 compares in a Blondel diagram the values of the d - q currents estimated by the model against the experimental values acquired from resolver position.

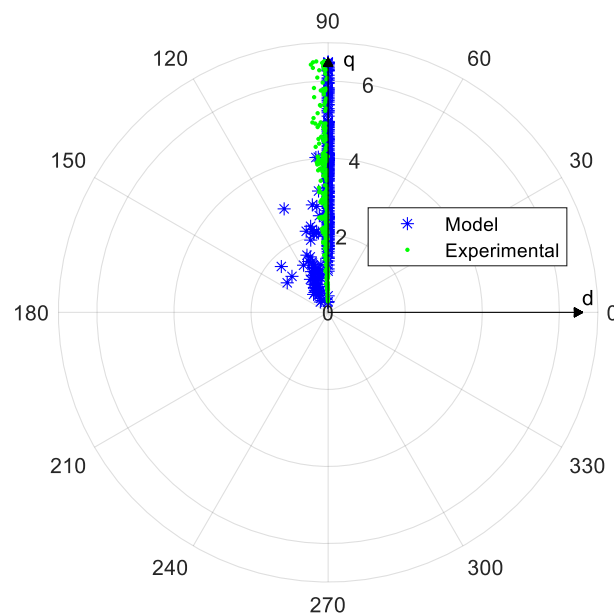


Figure 55: ABB PMSM d-q Blondel current diagram, estimated versus experimental

As can be seen in Figure 55, the model calculates correctly the control angle. The ABB PMSM drive applies a 90-degree current angle control without flux weakening capability.

6.4.2 GNC PMSM

A PMSM driven by a RENESAS sensorless FOC control platform YROTATE-IT-RX23T with flux weakening capability is studied as a second validation stage.

Table 43 summarizes the basic characteristics of the GNC PMSM.

Table 43: GNC PMSM characteristics

Manufacturer	Midal Talentos S.L
Converter model	RENESAS YROTATE-IT-RX32T
Rated Voltage [V_{RMS}]	200
Rated Current [A_{RMS}]	3
Rated Torque [N·m]	1
Rated Speed [1/min]	4600

Figure 56 shows the d - q space vector currents estimated by the algorithm. As can be seen, the major part of the working points are aligned with the quadrature axis. On the other hand, by validating the drive strategy control, the flux weakening operating points can be located.

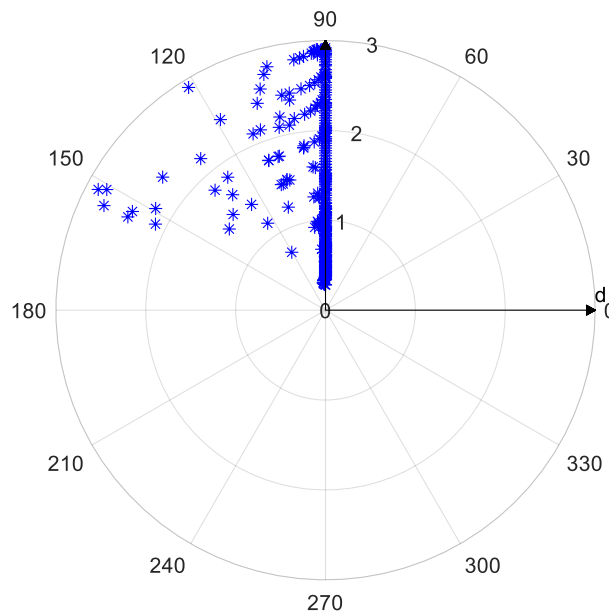


Figure 56: GNC PMSM d - q Blondel diagram parameter estimation values of current

6.4.3 Reference method for inductance measurement

The identified values of the inductance are compared with those obtained from a reference experimental method described in [125], using a DC biased AC source. The reference method allows measuring the d - q inductances under different load conditions. The AC signal peak value is small compared with the DC voltage bias. In this case the peak-to-peak is 1 V, whereas the DC component is changed from 5 to 15 V. The DC component represents the d - q voltage component.

Figure 57 shows the experimental setup required for the reference experimental method.

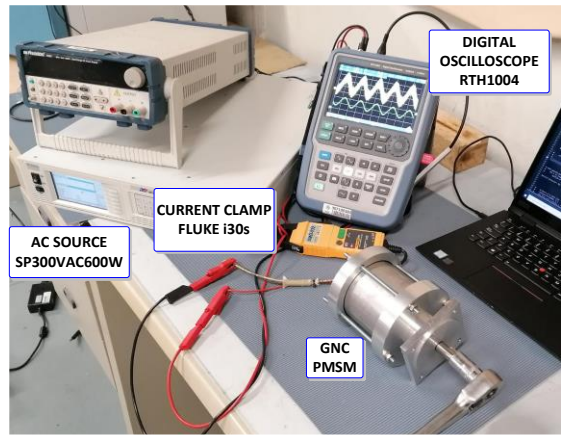


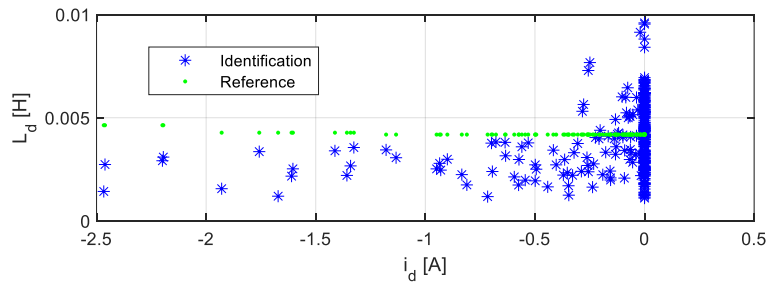
Figure 57: Experimental setup required to measure the reference inductances

Table 44 summarizes the instrumentation used to test the reference method.

Table 44: Instrumentation used for reference inductance method

AC Source	APM SP300VA600W ($I_{max}=5.6A$, $P_{out}=600 W$, 0.5 %)
Current Transducer	Fluke i30s ($\pm 30A$, 100 mV/A, 1%)
Oscilloscope	ROHDE & SCHWARZ RTH1004 $\pm(0.05\% +0.03\%)$

Once applied the reference method, Figure 58 and Figure 59 show the d - q inductance values for all operational tested points. The obtained inductance values are compared point by point.



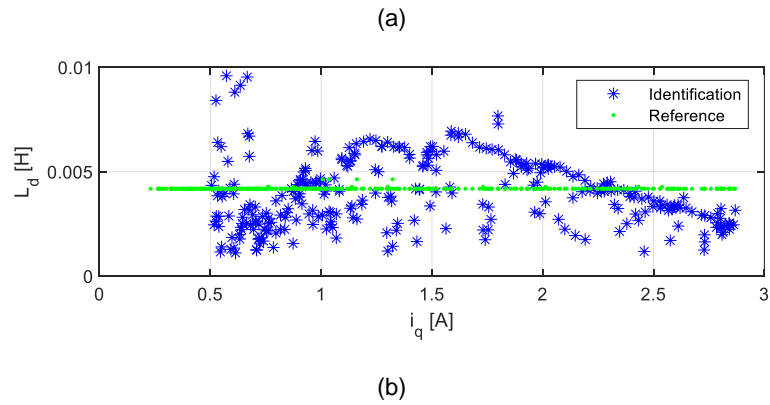


Figure 58: L_d estimation versus reference method. (a) L_d versus i_d (b) L_d versus i_d .

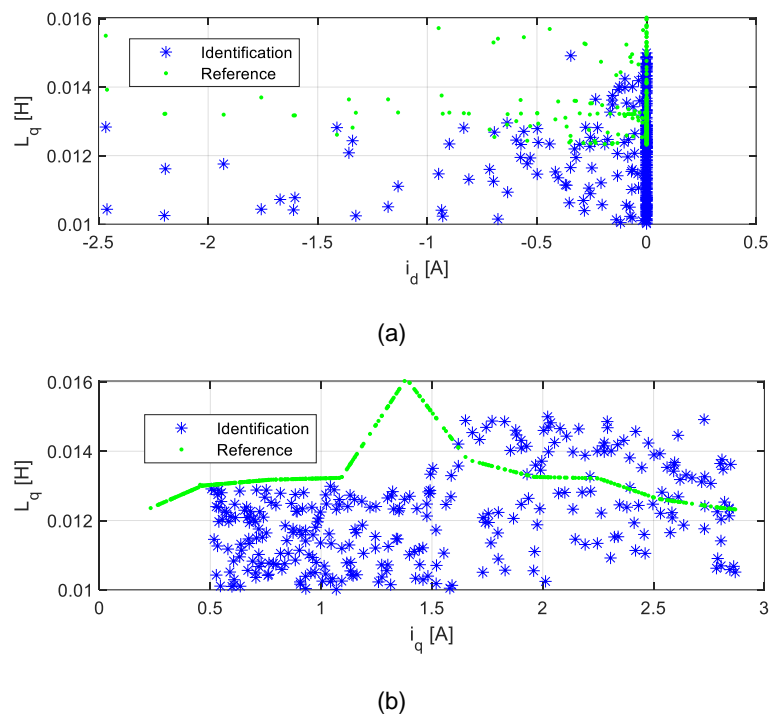


Figure 59: L_q estimation versus reference method. (a) L_q versus i_d (b) L_q versus i_d .

The reference method averages the inductance over one period of the current waveform. Moreover, during the tests it is required to block the rotor, so the measured inductance values depend on the rotor position. A characteristic of the method proposed in this thesis is that it calculates the inductance for every working condition when the motor is running in normal operation. Considering this difference, the mean value is compared with that of the reference method.

Table 45 compares the reference values of the inductances and the PM flux linkage against the ones obtained by applying the proposed methodology.

Table 45: Inductance and PM flux linkage parameters mean values comparison, parameter estimation method versus reference method

Magnitudes	Identified values	Experimental
Direct inductance L_d [mH]	3.91 (mean value)	4.18
Quadrature inductance L_q [mH]	12.10 (mean value)	13.40
Permanent magnet flux linkage Ψ_{PM-1st} [V·s/rad]	0.080	0.083

As can be seen in Table 45, the mean values obtained with the thesis methodology show a great similarity with the mean values of the reference method allowing to validate the parameters identified.

6.4.4 Accuracy of the estimated parameters

The accuracy of the estimated parameters is studied in this subsection using the combined standard uncertainty. The combined standard variance of the d - q inductances u_{c-Ld}^2 and u_{c-Lq}^2 is calculated as,

$$\left\{ \begin{array}{l} u_{c-Ld}^2 = \left(\frac{\partial L_d}{\partial \Delta u_d} \right)^2 \cdot u^2(\Delta u_d) + \left(\frac{\partial L_d}{\partial \Delta u_q} \right)^2 \cdot u^2(\Delta u_q) + \left(\frac{\partial L_d}{\partial \omega_m} \right)^2 \cdot u^2(\omega_m) + \\ \left(\frac{\partial L_d}{\partial i_{s-3rd}} \right)^2 \cdot u^2(i_{s-3rd}) + \left(\frac{\partial L_d}{\partial i_{s-5th}} \right)^2 \cdot u^2(i_{s-5th}) \\ u_{c-Lq}^2 = \left(\frac{\partial L_q}{\partial \Delta u_d} \right)^2 \cdot u^2(\Delta u_d) + \left(\frac{\partial L_q}{\partial \Delta u_q} \right)^2 \cdot u^2(\Delta u_q) + \left(\frac{\partial L_q}{\partial \omega_m} \right)^2 \cdot u^2(\omega_m) + \\ \left(\frac{\partial L_q}{\partial i_{s-3rd}} \right)^2 \cdot u^2(i_{s-3rd}) + \left(\frac{\partial L_q}{\partial i_{s-5th}} \right)^2 \cdot u^2(i_{s-5th}) \end{array} \right. \quad (130)$$

The d - q inductances are found from the d - q voltages, angular speed and the 3rd and 5th current harmonic components. The expressions differentiated result as,

$$\left\{ \begin{array}{l} u_{c-Ld}^2 = \left(\frac{1/2}{\omega_m \cdot (3 \cdot i_{s-3rd} + 5 \cdot i_{s-5th})} \right)^2 \cdot u^2(\Delta u_d) + \\ \left(\frac{1/2}{\omega_m \cdot (3 \cdot i_{s-3rd} + 5 \cdot i_{s-5th})} \right)^2 \cdot u^2(\Delta u_q) + \left(\frac{-(\Delta u_q + \Delta u_d) \cdot 1/2}{(3 \cdot i_{s-3rd} + 5 \cdot i_{s-5th}) \cdot \omega_m^2} \right)^2 \cdot u^2(\omega_m) + \\ \left(\frac{-(\Delta u_q + \Delta u_d) \cdot 3/2}{\omega_m \cdot (3 \cdot i_{s-3rd} + 5 \cdot i_{s-5th})^2} \right)^2 \cdot u^2(i_{s-3rd}) + \left(\frac{-(\Delta u_q + \Delta u_d) \cdot 5/2}{\omega_m \cdot (3 \cdot i_{s-3rd} + 5 \cdot i_{s-5th})^2} \right)^2 \cdot u^2(i_{s-5th}) \end{array} \right. \quad (131)$$

$$\begin{aligned}
 u_{c-L_d}^2 = & \left(\frac{1/2}{\omega_m \cdot (3 \cdot i_{s-3rd} + 5 \cdot i_{s-5th})} \right)^2 \cdot u^2(\Delta u_d) + \\
 & \left(\frac{-1/2}{\omega_m \cdot (3 \cdot i_{s-3rd} + 5 \cdot i_{s-5th})} \right)^2 \cdot u^2(\Delta u_q) + \left(\frac{-(\Delta u_q - \Delta u_d) \cdot 1/2}{(3 \cdot i_{s-3rd} + 5 \cdot i_{s-5th}) \cdot \omega_m^2} \right)^2 \cdot u^2(\omega_m) + \\
 & \left(\frac{-(\Delta u_q - \Delta u_d) \cdot 3/2}{\omega_m \cdot (3 \cdot i_{s-3rd} + 5 \cdot i_{s-5th})} \right)^2 \cdot u^2(i_{s-3rd}) + \left(\frac{-(\Delta u_q - \Delta u_d) \cdot 5/2}{\omega_m \cdot (3 \cdot i_{s-3rd} + 5 \cdot i_{s-5th})} \right)^2 \cdot u^2(i_{s-5th})
 \end{aligned} \tag{132}$$

The terms $u^2(\Delta u_d)$, $u^2(\Delta u_q)$, $u^2(\omega_m)$, $u^2(i_{s-3rd})$ and $u^2(i_{s-5th})$ are replaced by the values exposed in Table 45. The standard variance of the electrical angular speed, $u^2(\omega_m)$, is directly obtained from the FFT analysis and taking into account the fundamental frequency, which has an accuracy of 1.0 Hz. The standard uncertainty is the square root of (131) and (132). The accuracy is calculated multiplying the standard uncertainty by a coverage factor of 3 to ensure a 99% confidence level. In (131)-(132) the current components are dividing, therefore, low currents have a large contribution in the combined variance, this contribution being increased at lower speed operations.

Figure 60 and Figure 61 show the accuracy values for all operational points.

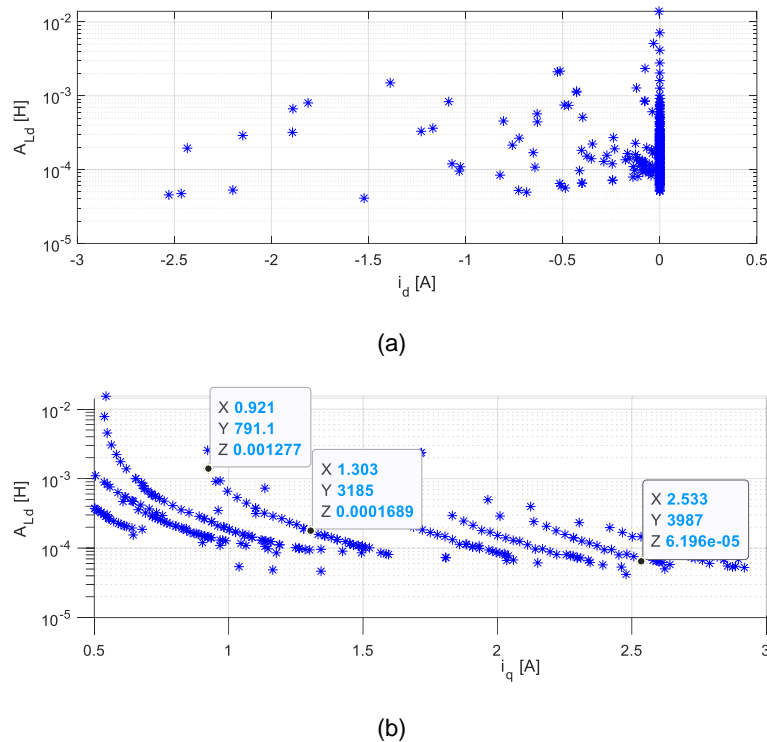


Figure 60: L_d axis accuracy (A_{Ld}), (a) A_{Ld} versus i_d (b) A_{Ld} versus i_q .

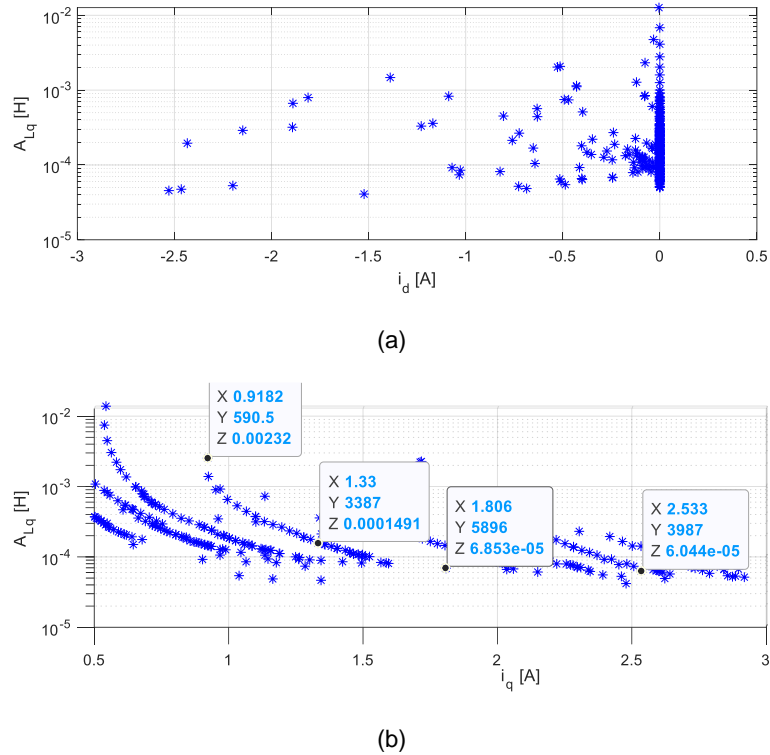


Figure 61: L_q axis accuracy (A_{Lq}), (a) A_{Lq} versus i_d (b) A_{Lq} versus i_q .

The accuracy is reduced at lower currents and lower angular speeds. Therefore, the accuracy increases with the angular speed (Y values of data labels in Figures).

Table 46 shows the mean accuracy of the estimated d - q inductances by applying (131)-(132). The accuracy is calculated with a coverage factor of 3, ensuring a confidence level of 99%.

Table 46: Accuracy mean values for d - q inductances estimation

Magnitudes	Absolute accuracy [mH]
Direct inductance accuracy A_{Ld} [mH]	0.56 mH (mean value)
Quadrature inductance accuracy A_{Lq} [mH]	0.56 mH (mean value)

6.4.5 Computational burden

The parameter estimation method requires 0.66 seconds to calculate all points displayed in Figure 58 and Figure 59 using an Intel® Core™ i9-7940X 3.10 GHz processor with 64 GB RAM memory.

6.5 Parameter estimation methodology conclusions

A parameter estimation method to estimate the PMSM inductances and current control magnitude and angle has been developed. The method estimates these magnitudes from its performance test on the entire torque-speed range, thus, finding parameter variations as a function of the load conditions. The main novelty on the identification of inductances is related to the use of the differential power factor due to the harmonic distortion. The method does not require geometry information, knowledge of the control strategy or a position sensor. It uses a $d-q$ electrical model with harmonic decomposition and avoids applying any optimization solver, thus greatly reducing the computational burden. The method is considered off-line, however, although it can be applied on-line to identify parameters from a unique operating point. The algorithm has been validated using two different PMSMs. Results show an accurate identification of current space vector magnitudes and angle and inductances values. The computational burden is low, and thus, the estimation is performed in an affordable time.

7. PMSM Performance Evaluation

The limitations when testing the performance of PMSMs arise when using current strategies. The complexity increases when the whole torque-speed-map is tested, due to the number of experiments to carry out, set up the correct discretization, prepare the experimental setup, etc. Moreover, most of the instrumentation needed is expensive, especially if high precision measurement devices are required. For all the exposed reasons, a new methodology to evaluate the performance of PMSMs is developed, easing the whole process and reducing the requirements of the instrumentation required.

This chapter presents a novel PMSM performance estimation method based on the blocked rotor test. The method does not require to know the geometry of the PMSM. This method avoids the use of expensive measurement devices and does not require a complex experimental setup. Moreover, as the parameters are identified as a function of the load conditions, this method allows to reproduce the PMSM performance by applying different control strategies using a $d-q$ electrical model. The method does not require any optimization algorithm, thus simplifying and speeding up the process to reproduce the performance. The method is validated experimentally by comparing the performance of the PMSM designed for hydraulic applications. The torque-speed-efficiency map and electromagnetic parameters are validated using finite element analysis (FEA) simulations and they are compared with the performance evaluated in Chapter 5.

This chapter exposes the methodology to reproduce the performance of a PMSM by applying a parameter estimation approach based on a stand still test. First, section 7.1 exposes the methodology, section 7.2 shows the experimental results validation and finally, section 7.3 concludes the methodology results.

Contents

- 7.1 PMSM blocked rotor test and performance analysis methodology
- 7.2 Parameter estimation and performance evaluation results
- 7.3 PMSM performance evaluation from parameter estimation conclusions

Nomenclature

e_s	Stator back electromotive force [V]
i_d	Direct axis current [A]
i_q	Quadrature axis current [A]
i_s	Stator phase current [A]
i_{cd}	Iron losses direct axis current [A]
i_{cq}	Iron losses quadrature axis current [A]
i_{od}	Effective direct axis current [A]
i_{oq}	Effective quadrature axis current [A]
L_s	Parameter estimation inductance [H]
L_{ls}	Leakage inductance [H]
L_{ms}	Magnetizing inductance [H]
L_d	Inductance in the direct axis [H]
L_{ld}	Leakage inductance in direct axis [H]
L_{md}	Magnetizing inductance in the direct axis [H]
L_q	Inductance in the quadrature axis [H]
L_{lq}	Leakage inductance in quadrature axis [H]
L_{mq}	Magnetizing inductance in the quadrature axis [H]
m	Phases number [-]
n	Rotor angular speed [1/min]
p	Pairs of poles [-]
P_{Cu}	Copper losses [W]
P_{Fe}	Iron losses [W]
P_{ml}	Mechanical losses [W]
R_{Fe}	d - q model resistance of the iron [Ω]
$R_{Fe-test}$	Identification model resistance of the iron [Ω]
R_s	Resistance of the stator windings per phase [Ω]
T	Output mechanical torque [N·m]
u_d	Direct axis voltage [V]
u_q	Quadrature axis voltage [V]
u_s	Stator phase voltage [V]
u_{Ls}	Parameter identification inductance voltage [V]
U_{dc}	Voltage of the DC bus [V]

- θ_e Electrical angular position [rad]
 θ_m Mechanical angular position [rad]
 ω_m Electrical angular speed [rad/s]
 Ψ_{abc} Flux linkage in the stator [V·s]
 Ψ_{PM} Flux linkage of the permanent magnets [V·s]
 Ψ_d Flux linkage in the direct axis [V·s]
 Ψ_q Flux linkage in the quadrature axis [V·s]

7.1 PMSM blocked rotor test and performance analysis methodology

The blocked rotor test and performance analysis methodology for PMSMs is presented in this subsection. As a first step, experiments with blocked rotor are performed. The procedure consists in connecting a single-phase voltage source to a three-phase PMSM. The positive terminal of the AC source is connected to one of the motor phases, which is set as the reference phase by convention, on the other hand, the negative terminal is connected to the two phases remaining. Instantaneous voltage and current are acquired. There are three main changing parameters during the experimental procedure, which are the frequency, RMS voltage and rotor angle. Figure 62 shows the experimental setup, including the instrumentation used and the experimental procedure.

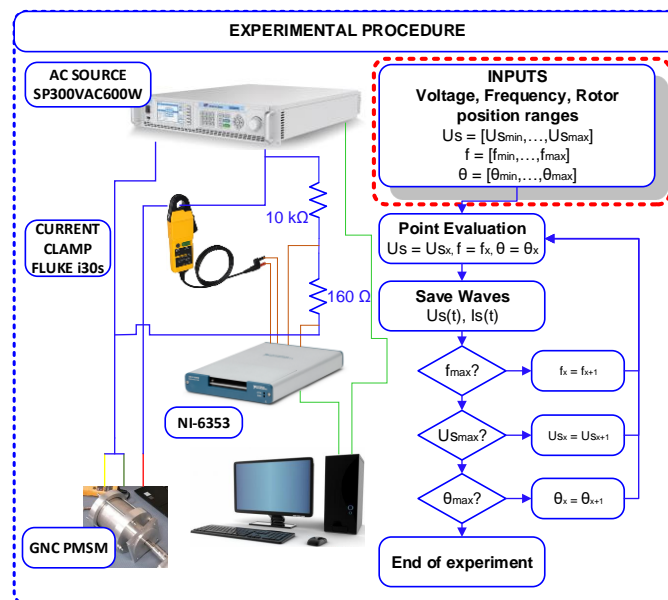


Figure 62: PMSM blocked rotor test experimental setup and procedure algorithm

Once the instantaneous voltage and currents are acquired, these magnitudes are post-processed to identify the electromagnetic parameters and iron losses, which will allow to reproduce the motor performance.

Two electrical models are used, the first electrical model allows extracting the PMSM parameters, whereas the second model allows reproducing the PMSM performance. Figure 63 shows both models respectively. The inductance is split into the leakage and linkage components, respectively.

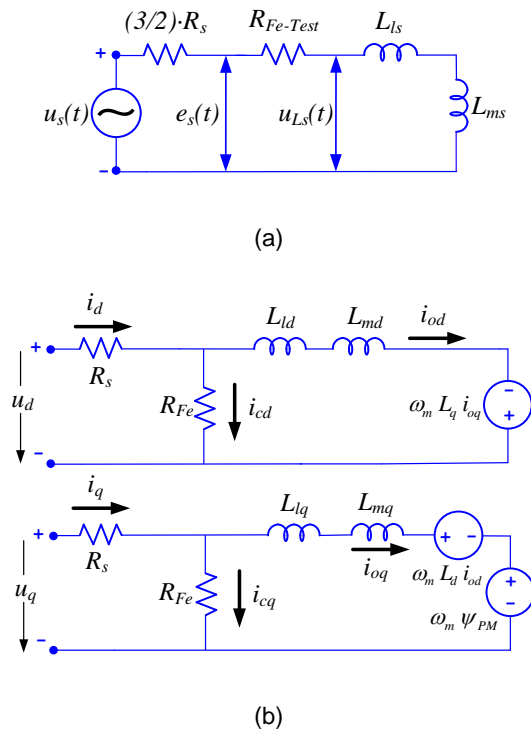


Figure 63: Electrical models used to (a) identify the PMSM parameters and (b) to reproduce the PMSM performance

7.1.1 Parameter estimation electrical model

The magnitudes to be identified are the iron losses and stator inductance as a function of current and supply frequency, which are required in the d - q electrical model. A low-pass filter is applied to the acquired data. This filter is a first-order low-pass with a stopband attenuation of 60 dB and cut-off frequency corresponding to the 11th electrical harmonic frequency.

The voltage drop considering iron losses and inductance is,

$$e_s(t) = u_s(t) - i_s(t) \cdot \frac{m}{2} \quad (133)$$

The instantaneous iron power is computed as,

$$P_{si}(t) = e_s(t) \cdot i_s(t) \quad (134)$$

The mean power of the iron resistor model is calculated as,

$$\bar{P}_{Fe-Test} = \text{mean}(P_{si}(t)) \quad (135)$$

The equivalent series resistor modeling the iron losses for parameter estimation is computed as,

$$R_{Fe-Test} = \frac{\overline{P}_{Fe-Test}}{(i_{s-RMS})^2} \quad (136)$$

The instantaneous iron losses are computed as,

$$P_{Fe-Test}(t) = R_{Fe-Test} (i_s(t))^2 \quad (137)$$

The instantaneous power in the inductor, whose mean value is zero because it ideally does not consume power, is calculated as,

$$P_{Ls}(t) = P_{st}(t) - P_{Fe-Test}(t) \quad (138)$$

The voltage drops across the inductor is determined as,

$$u_{Ls}(t) = e_s(t) - R_{Fe-Test} \cdot i_s(t) \quad (139)$$

The temporal expressions of the voltage drop across the inductor and the current are known, therefore, by solving the differential equation in (111) $L_s(t)$ can be calculated.

$$u_{Ls}(t) = L_s(t) \cdot \frac{di_s(t)}{dt} + i_s(t) \cdot \frac{dL_s(t)}{dt} \quad (140)$$

When the instantaneous values of the inductance are known, the values to be found corresponds to those corresponding to the maximum current instant. In this case $L_s(t) = L_{ls}(t) + L_{ms}(t)$ is defined as the sum of the leakage and linkage terms.

$L_s(t)$ become unstable when the current reaches its maximum, i.e., when the term $di_s(t)/dt$ is zero. For this reason, in order to avoid numerical instabilities, the values to consider are the ones corresponding to 3 electrical degrees before and after the maximum of the current. For instance, considering that within an electrical period the maximum and minimum current values are reached at 90° and 270° , the angles to select the inductance are 87° and 93° .

Then, all values gathered at each peak are averaged to obtain a unique inductance for each studied case, whose value is $L_s(i_d, i_q)$. Next, the values obtained from the parameter estimation process are used to calculate the differential stator flux linkage, i.e., the flux linkage generated by the stator windings as $\Delta\psi_s(i_d, i_q) = L_s(i_d, i_q) \cdot i_s$. Then, considering the electrical angle, this flux linkage is projected along the d - q axis reference, thus obtaining the d - q fluxes generated by the stator windings. The permanent magnet flux linkage is usually found in the machine nameplate. If this magnitude is not provided, an open circuit test can be performed to obtain the first harmonic of the back-electromotive force produced by the permanent magnets. Therefore, the direct axis flux linkage is obtained as the sum of the permanent magnet flux linkage and the differential flux

linkage generated by the stator windings, $\psi_d = \psi_{PM} + \Delta\psi_s(i_d, i_q) \cdot \cos(\theta_e) = \psi_{PM} + L_d(i_d, i_q) \cdot i_d$. The quadrature axis flux linkage is directly the projection of the flux linkage produced by the stator windings along the q axis, $\psi_q = \Delta\psi_s(i_d, i_q) \cdot \sin(\theta_e) = L_q(i_d, i_q) \cdot i_q$.

The values obtained are used to calculate the d - q inductances of the electric model defined in Figure 63 (b). The inductance obtained through the parameter estimation process identifies the magnetizing and leakage inductances together, so the d - q inductances derived from this process consider the leakage and linkage terms with the same magnitude.

Finally, the instantaneous power losses have the shape of a corrected sinusoidal wave. The peaks, are the losses to take into account as a reference for normal operating conditions.

Figure 64 shows the instantaneous iron losses identified applying the procedure previously exposed. Those iron losses are not directly the running operation losses for PMSM but the magnetic losses of the experiment. From this temporal expression the PMSM steady state losses are calculated when running at normal operation.

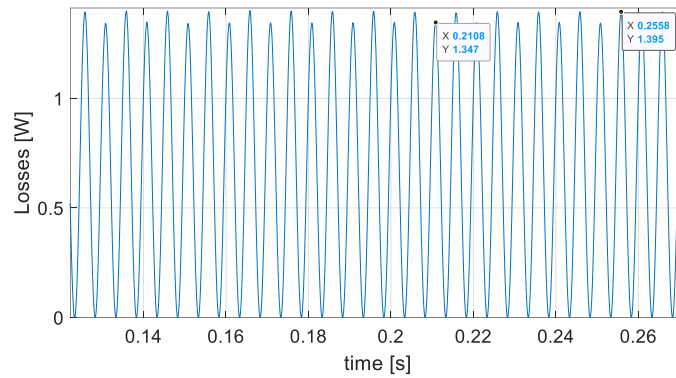


Figure 64: Instantaneous iron losses for parameter identification electrical model

As shown in Figure 64, the peaks of the iron resistance losses are those corresponding to the maximum current space vector. There are two different peaks, the higher peaks corresponding to those contributing to the permanent magnet flux direction. Therefore, the peak values are the values acquired to represent the PMSM losses for the space vector in question for normal operation. The main principle behind this approximation comes from the definition of the magnetic losses, recalling Bertotti equations in time domain.

$$P_{Fe-Eddy} = \frac{\sigma \cdot h^2}{12 \cdot T} \cdot \int_0^T \int_{d\forall} \left(\frac{dB}{dt} \right)^2 \cdot d\forall \cdot dt \quad (141)$$

$$P_{Fe-Hyst} = \frac{K_h \cdot \rho}{T} \cdot \int_{d\forall} B_m^\alpha \cdot \left(1 + \sum_{i=1}^n \frac{\beta}{B_m} \cdot (\Delta B_i) \right) \cdot d\forall \quad (142)$$

$$P_{Fe-Excess} = \frac{K_{ex} \cdot \rho}{T} \cdot \int_0^T \int_{dV} \left(\frac{dB}{dt} \right)^{1.5} \cdot dV \cdot dt \quad (143)$$

Considering equations (111) to (114), the losses are expressed as a function of the time variation of the magnetic flux density. Therefore, for a small time variation dt , the analogy is a current space vector variation by a differential angle $d\theta$ when the PMSM is operating under normal conditions. It is used the space-time conversion. It is noted that B is the magnetic flux density, σ is the electrical conductivity of iron, h the laminations thickness, dV the differential volume, T the time period, K_h the hysteresis constant, dt the differential time, ρ the iron laminations density, α and β the hysteresis exponents, and K_{exc} the excess constant.

$$\left(\frac{dB}{d\theta_e} \right) = \left(\frac{dB}{dt} \right) \cdot \left(\frac{dt}{d\theta_e} \right) \rightarrow \left(\frac{dB}{dt} \right) = \left(\frac{dB}{d\theta_e} \right) \cdot \omega_e \quad (144)$$

The losses obtained are the total magnetic losses, because the algorithm is applying the space-time conversion with a current space vector. Therefore, the process considers the three phases contribution to the losses.

Figure 65 summarizes the parameter identification algorithm.

1: Take $u_s(t)$ and $i_s(t)$ for each voltage, frequency and rotor position combination.

2: Apply a digital low pass filter.

3: Compute iron losses and inductance voltage drop:

$$e_s(t) = u_s(t) - i_s(t) \cdot R_s \cdot \frac{m}{2}$$

4: Compute instantaneous power: $P_{st}(t) = e_s(t) \cdot i_s(t)$

5: Compute mean iron losses power: $\bar{P}_{Fe} = \text{mean}(P_{st}(t))$

6: Compute equivalent iron losses resistor: $R_{Fe} = P_{Fe-\text{mean}} / i_{s-\text{RMS}}^2$

7: Compute instantaneous iron losses: $P_{Fe}(t) = i_s(t)^2 \cdot R_{Fe}$

8: Compute instantaneous reactive power: $P_{Ls}(t) = P_{st}(t) - P_{Fe}(t)$

9: Compute linkage + leakage induction voltage: $U_{Ls}(t) = E_s(t) - I_{s-f}(t) \cdot R_{Fe}$

11: Linkage + leakage inductance calculation:

$$E_s(t) = L_s(t) \cdot \frac{dI_{s-f}}{dt} + I_{s-f}(t) \cdot \frac{dL_s}{dt} \rightarrow L_s(t)$$

12: Stator inductance as a function of the d - q currents: $L_s(t) \rightarrow L_s(i_d, i_q)$

13: Compute the flux linkage gradient using the stator inductance

$L_s(i_d, i_q)$:

$$\Delta\psi_s = L_s(i_d, i_q) \cdot i_s(i_d, i_q)$$

14: Determination of the d - q flux linkage:

$$\begin{cases} \psi_d = \psi_{PM} + \Delta\psi_s \cdot \cos(\theta_e) = \psi_{PM} + L_d(i_d, i_q) \cdot i_d \\ \psi_q = \Delta\psi_s \cdot \sin(\theta_e) = L_q(i_d, i_q) \cdot i_q \end{cases}$$

15: Selection of representative inductance for the space vector current:

$$\begin{cases} \psi_d = \psi_{PM} + \Delta\psi_s \cdot \cos(\theta_e) = \psi_{PM} + L_d(i_d, i_q) \cdot i_d \rightarrow L_d(i_d, i_q), L_q(i_d, i_q) \\ \psi_q = \Delta\psi_s \cdot \sin(\theta_e) = L_q(i_d, i_q) \cdot i_q \end{cases}$$

16: Selection of iron losses for real operating conditions: $P_{Fe}(i_d, i_q, f)$

Figure 65: Parameter identification algorithm to extract inductances and iron losses

7.1.2 Performance analysis using d - q electrical model

As mentioned in previous chapters, the d - q electrical model is useful when representing the PMSM performance along the torque-speed map.

First, the od and oq currents are discretized (Figure 63b) within the second quadrant, i.e., negative d axis and positive q axis. Once having discretized the odq currents, the values of the parameter estimation inductance are calculated.

$$\begin{cases} L_d(i_{od}, i_{oq}) \\ L_q(i_{od}, i_{oq}) \end{cases} \quad (145)$$

Next, the flux linkages can be computed, Considering the d - q currents and inductances calculated in the previous step, the d - q flux linkages are calculated. The permanent magnet flux linkage is a nameplate parameter. If this magnitude is not provided, an open circuit test should be performed in order to obtain the first harmonic of the back-electromotive force produced by the permanent magnets.

$$\begin{cases} \psi_d = \psi_{PM} + L_d \cdot i_{od} \\ \psi_q = L_q \cdot i_{oq} \end{cases} \quad (146)$$

The torque can be computed at this stage using the d - q expression for electromagnetic torque. Then, taking the od and oq current values, the iron losses, which have been previously identified, are extracted,

$$P_{Fe}(i_{od}, i_{oq}, \omega_m) \quad (147)$$

The back electromotive force is computed at this stage for each angular discretized speed. As the magnetic losses are known, the parallel resistance representing that losses is calculated.

$$R_{Fe} = m \cdot (u_{od}^2 + u_{oq}^2) / (2 \cdot P_{Fe}) \quad (148)$$

The currents i_{cd} and i_{cq} are calculated from the iron resistance. Therefore, the total current i_d and i_q can be easily calculated. Then, voltage equations are computed.

Finally, the points are selected as a function of the control strategy defined.

Figure 66 summarizes the PMSM performance reproduction algorithm using the d - q electrical model.

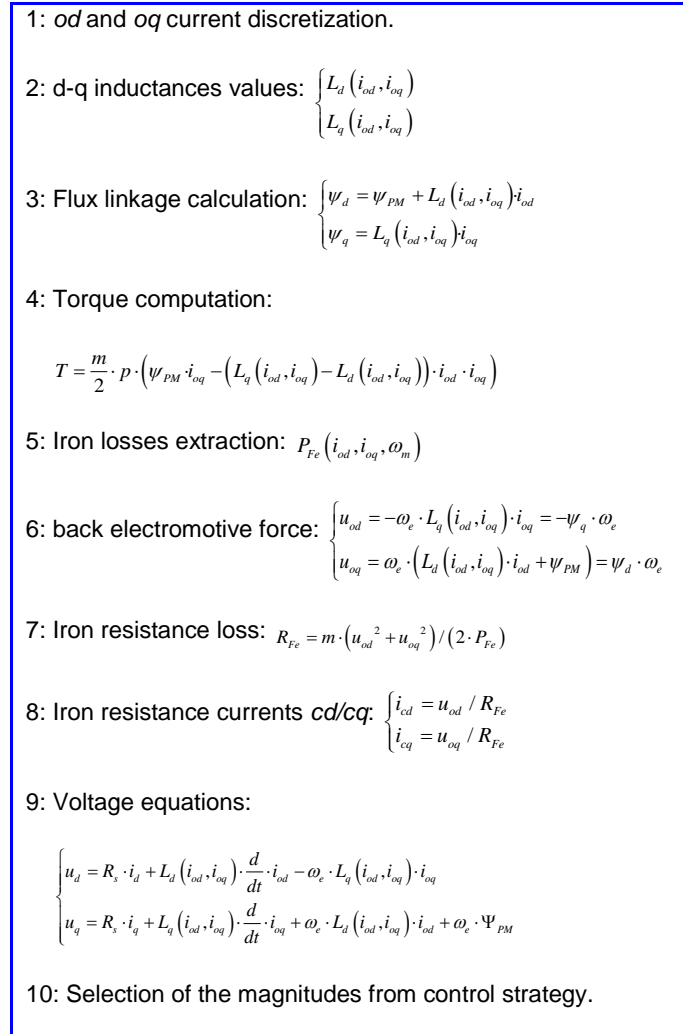


Figure 66: PMSM performance reproduction algorithm using d-q electrical model

7.2 Parameter estimation and performance evaluation results

To verify the parameter estimation feasibility together with the performance evaluation, the PMSM designed in this thesis is used. The results compare the identified parameters and performances with those obtained from experimental tests and FEA analysis.

The magnitudes acquired are the temporal values of the voltage and current for each rotor angle and frequency combination. Then, the process described is applied to extract the d-q flux linkages and the iron losses. To validate the parameter estimation procedure, first the d-q flux linkages as a function of the d-q currents are compared against the results provided by the finite element analysis (FEA). The absolute error between the identified and FEA values are provided point by point. The software used to this purpose is Altair Flux 2019®.

Once the d - q flux linkages are validated against FEA results, the PMSM performance is validated using the iron losses obtained by means of the parameter estimation process. To do so, the torque-speed-efficiency map is calculated using the d - q flux linkages identified previously. Once the torque-speed-efficiency map is obtained using exclusively the parameter estimation process, it is compared against the torque-speed-efficiency map evaluated using the FEA model developed in Comsol Multiphysics® where the copper and iron losses are modelled. In addition, for a deeper analysis, the experimental torque-speed-efficiency map is obtained from a previous study thus obtaining its performance in real conditions. Finally, the computational burden is estimated.

Figure 67 shows the estimated iron losses versus the d - q currents and frequency. As can be observed, the losses follow a quadratic behavior. Lower frequencies, in this case 100 Hz, show wider current range for the experiment because they present lower impedance.

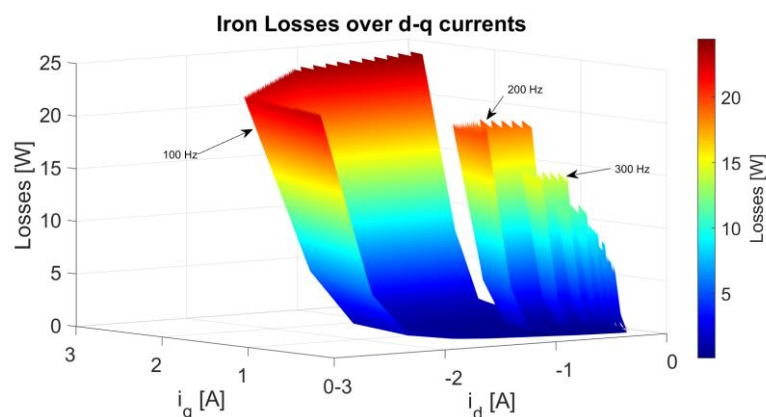
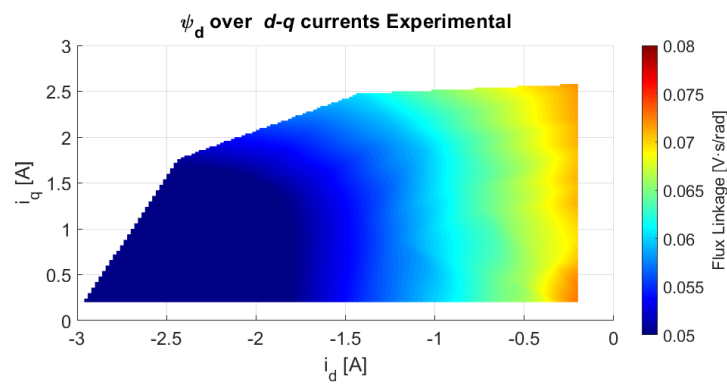


Figure 67: Iron losses estimation versus d-q currents and frequency

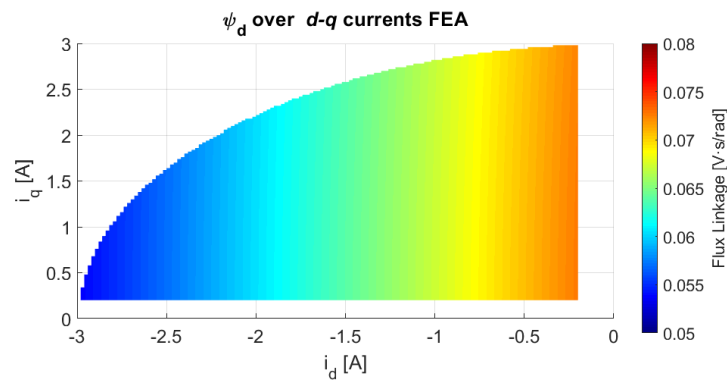
7.2.1 d - q flux linkages comparison

First, the d - q flux linkages can be computed versus the d - q currents. These magnitudes are very important when reproducing performances because the torque and voltage computation directly depend from these magnitudes. In addition, the use of flux linkages simplifies the characterization and computation, providing higher computational stability.

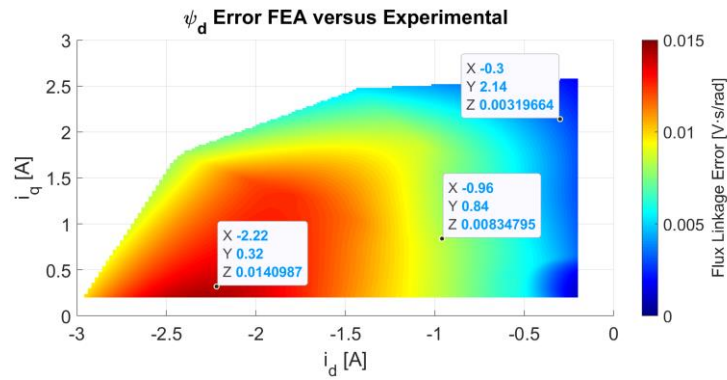
Figure 68 and Figure 69 show the direct and quadrature axis flux linkage versus the d - q currents, respectively. Each figure compares the flux linkage obtained through the parameter estimation methodology and FEA.



(a)



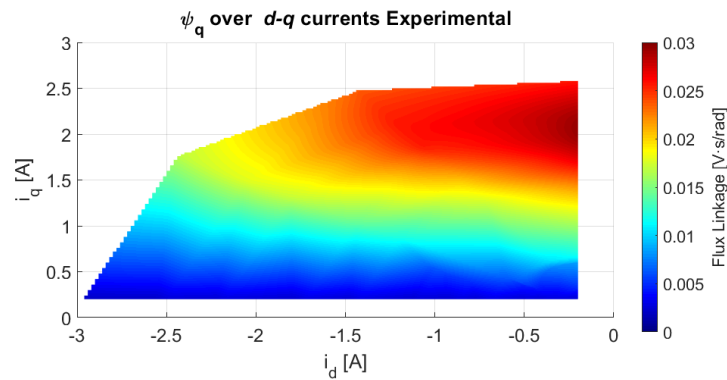
(b)



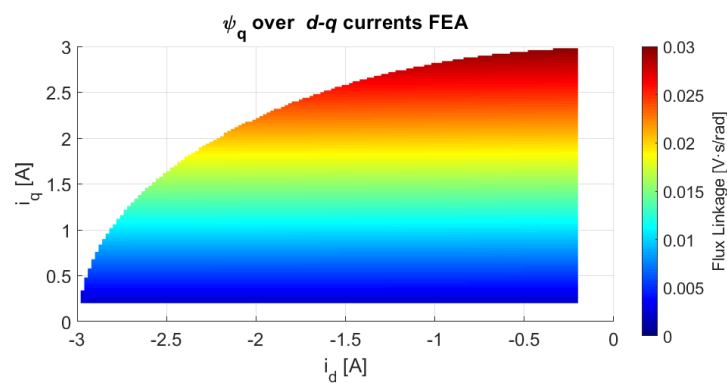
(c)

Figure 68: (a) Parameter estimation d flux linkage map versus d - q currents. (b) FEA d flux linkage map versus d - q currents. (c) Absolute error between FEA and experimental maps.

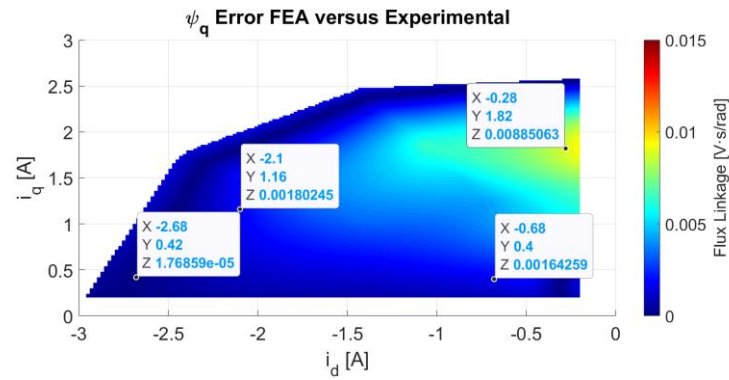
The d axis flux linkage maps are similar. The distribution that can be observed in FEA is more linear in the d axis and constant in the q axis. On the other hand, in the identified parameter, the distribution is quadratic in both axes. These differences can be due to manufacturing tolerances of the iron lamination sheets and magnets.



(a)



(b)



(c)

Figure 69: (a) Parameter estimation q flux linkage map versus d - q currents. (b) FEA q flux linkage map versus d - q currents. (c) Absolute error between FEA and experimental maps.

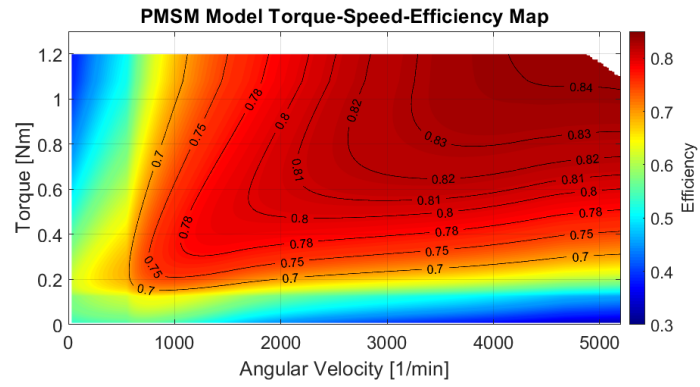
For q axis flux linkage, a great similarity is observed, thus validating the flux linkage identification for both axes.

As observed, the parameter estimation does not cover the whole currents circle. This effect is originated when defining the discretization of frequencies and rotor angles. Therefore, considering more rotor angles, the map obtained will be smoother using the same parameter estimation methodology. In addition, the currents identified in the direct axis have higher magnitude than the values of the current in the quadrature axis. This is because the inductance is higher in the quadrature axis, thus resulting a higher impedance.

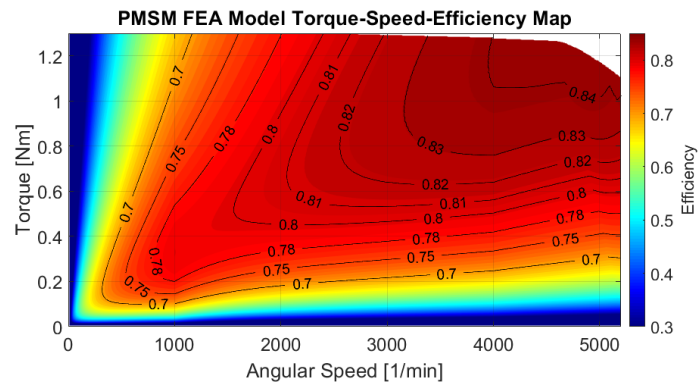
7.2.2 PMSM performance evaluation

The torque-speed-efficiency map of the PMSM is reproduced, as explained in the methodology subsection. A 90-degree current control strategy with flux weakening capability is computed.

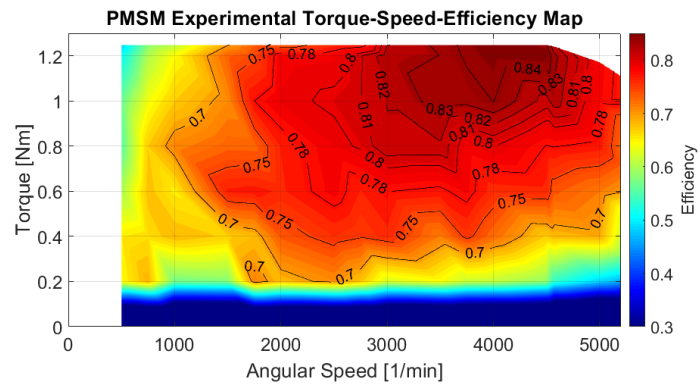
Figure 70 shows the PMSM torque-speed-efficiency map for different evaluation methods. As can be seen, the performance evaluation using the parameter estimation magnitudes matches with high accuracy the PMSM performance.



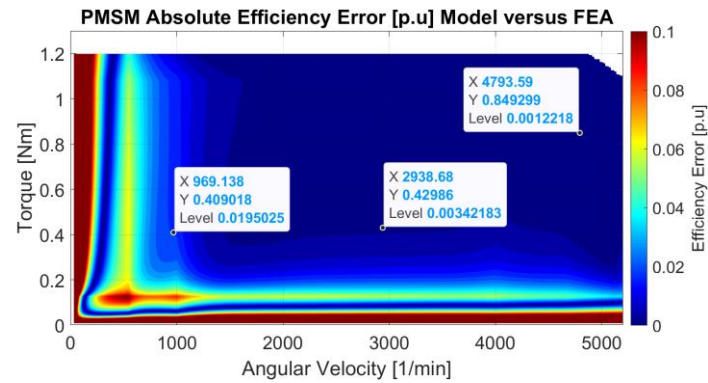
(a)



(b)



(c)



(d)

Figure 70: PMSM torque-speed-efficiency map (a) Parameter estimation performance evaluation, (b) FEA and (c) Experimental. (d) Absolute error between model and FEA maps.

The PMSM torque-speed-efficiency map reproduced using parameter estimation magnitudes matches with high accuracy with the performance reproduced with FEA and directly measured from experimental tests. Thus the parameter estimation magnitudes allow to reproduce with high fidelity the PMSM real performance using the d - q electrical model with losses.

7.3 PMSM performance evaluation from parameter estimation conclusions

In this thesis a new methodology to identify PMSM parameters to reproduce the PMSM performance has been presented. The parameter identification is performed by means of stand-still experiments. The method does not require any geometry knowledge and it reduces the complexity. A d - q electrical model is used to reproduce the PMSM performances considering copper and iron losses.

The method has been validated using the designed PMSM. First, the d - q flux linkages are compared against those obtained through FEA, showing similar values. A second validation is performed calculating the torque-speed-efficiency map. Then, it is compared against FEA and experimental maps. Results show high accuracy when reproducing PMSM performances. Therefore, the parameter estimation method is validated, providing detailed information of the PMSM performance.

8. Thesis Conclusions

In the recent years, due to the wide range of applications where water pumping is required, the operational concept of this system is evolving. So far, water pumping applications have been based on induction motors, usually conceived to operate in a single operating point. Nevertheless, nowadays hydraulic applications are increasingly requiring systems capable to operate efficiently under different pressure and volumetric flow demands. Some of the most demanded applications of water pumping are for domestic residential, collective residential, swimming pools, agriculture, water treatment, construction sector, etc. Moreover, the industry trend for pumping systems requires to reduce the volume of all components, providing compact products for the same applications.

Focusing in the tools available to design electrical machines, finite element analysis (FEA) has become the preferential tool due to the high accuracy and the capability of considering multiphysics. Nevertheless, one of the main drawbacks of this tool is the high computational burden, becoming incompatible everyday use, limiting its usability for industry projects. For this reason, the research must consider to use the most advanced design tools but taking into account the feasibility in terms of time, computational resources and costs, making not only a functional but a practical tool to be used in industry applications.

Furthermore, from an industrial scope so far, the testing methodologies are focused on evaluating point by point the electrical machine performance, being a robust and trustable way to measure and validate the electrical machine characteristics. Nevertheless, this method requires a large time to prepare the experimental setup and to evaluate the whole motor performance. For this reason, there is a special interest on improving parameter estimation and performance evaluation techniques for electrical machines to reduce evaluation time, setup complexity and increase the number of physical magnitudes to measure in order to have deeper information.

All these features of the water pumping industry market and scientific trends justified this work within the industrial doctorate plan.

In the introductory chapter, after exposing the research field and the objectives, three main hypotheses were postulated:

- It is possible to define on first hand, within a region, the electrical machine torque-speed-efficiency map and through an algorithm find a suitable unique geometry which accomplish these characteristics.

- It is possible to implement an optimization algorithm for electrical machines using finite element analysis (FEA) with low computational burden.
- It is possible to implement complementary algorithms and auxiliary tests to expand the information of the electrical machine acquired from standard experimental tests and reduce time when evaluating the motor performance.

These three hypotheses aimed to be the basis of development of this research changing the design and optimization paradigm focusing on defining beforehand the desired performance of the electrical machine in relation with the application system. This approach allows the designer plenty of freedom to study the system, define the desired motor performance and set the sizing, thermal and mechanical limitations from the beginning of the process. Moreover, providing auxiliary tools to deepen the standard test information and complementary tests to validate the motor performance.

The research and development strategy is divided in four stages, i.e., definition, design, optimization and validation stages. The definition stage was aimed to provide scientific background to study the scientific frontiers and clarify the research and development direction of this work. During the definition stage the electrical machine is selected, the modelling and optimization method are defined, the hydraulic application is studied and the parameter estimation and performance analysis techniques are studied to characterize the motor. During the design stage all the models are developed, i.e., the finite element design and optimization tool, the parameter estimation and performance analysis tests procedures and algorithms. The optimization stage is where the motor is designed and optimized based on the hydraulic application in question. Finally, after manufacturing the prototypes, during the validation stage the FEA design and optimization process, the parameter estimation and performance evaluation tools to characterize the motor are validated.

Focusing on the FEA design optimization algorithm, a tool was developed focusing on PMSM motor topologies. A combination of magneto-static FEA and $d-q$ electrical modelling is used greatly reducing the computational burden compared to conventional methods based on time-dependent FEA. Thus the second hypothesis of this thesis is validated. As mentioned in the introduction, the input of the optimization algorithm is the target or objective torque-speed-efficiency map, therefore, the design-optimization process searches the motor geometry. In each iteration the algorithm approaches the torque-speed-efficiency map, i.e., the process uses the entire map to compute the objective function. To do so, an image comparison technique called structural similarity index (SSIM) is used, giving in only one indicator between 0 and 1 the equality

between the optimization and target maps. The design optimization tool takes into account iron, mechanical and copper losses. To perform Iron losses using magneto-static FEA considering harmonic contents, time-space conversion theory is applied. This combination allows having high precision tool with low computational burden. To validate the method before designing the electrical machine aimed for this study, the public experimental data of the Toyota Prius 2004 and Toyota Camry 2007 PMSMs were used. Results presented in this work show the high accuracy evaluating and finding the original geometries of both PMSMs. For Toyota Prius 2004 PMSM the SSIM index resulting from the comparison of the seed torque-speed-efficiency map and the experimental one is 0.701, whereas the SSIM index between the torque-speed-efficiency map of the optimized motor and the experimental one is 0.929. For Toyota Camry 2007 PMSM. The SSIM index between the seed torque-speed-efficiency map and the experimental one is 0.7978, whereas the SSIM index between the torque-speed-efficiency map of the optimized motor and the experimental one is 0.9571. This process validates the second hypothesis.

After validating the design-optimization tool, the model is adapted for water pumping applications, and in particular for the application of study in this work. For the target torque-speed-efficiency map, two main points of the whole system are designed first according to the initial specifications, the values imposed by the designer are the torque, speed and system efficiency. After locating these main conditions, extra operating points were defined in order to increase the resolution of the objective torque-speed-efficiency map. The PMSM designed using the methodology attains the efficiency targets for the torque-speed-area being the SSIM between the reference and the design optimization map 0.983, thus the algorithm converges with 1.7% of similarity error. Next, the prototype was manufactured and tested. After performing the experimental test, the torque-speed-efficiency map obtained show high fidelity between the FEA and experimental test. The relative similarity error between both maps is 4 %. Finally, the FEA and experimental system performance was compared obtaining a relative error of 1% in the target efficiencies. This process validates the first hypothesis.

Once the design optimization is designed and validated experimentally, using standard test the PMSM prototype can be validated successfully but with some drawbacks. The main disadvantages are the drive limitation, extensive experimental time set up, torque and speed limitations, etc. On the other hand, important magnitudes such as inductances over injected currents are difficult to measure using standard tests. In order to be able to evaluate the PMSM performance considering different conditions two methodologies are developed. The first methodology is aimed to complement the standard measurements in running operation to

evaluate the control current angle without any position sensor, and the d-q inductances as a function of the current. The second methodology is aimed to evaluate the motor performance without needing any torque transducer and without needing any specific drive. Thus, providing a good complement to characterize the motor a part from standard experimental tests.

Focusing on the first methodology, it is designed an algorithm to estimate the PMSM electromagnetic parameters. This algorithm is meant to be implemented during standard experimental test. The method allows characterizing the motor parameters by considering its performance on the entire torque-speed range, thus, allowing to find the parameter variations as a function of the load conditions. As a main novelty, the identification of the d-q inductances is based on the differential power factor due to the harmonic distortion. To identify the vectors magnitudes and angles, the method does not require any geometry information, no prior knowledge of the control strategy and does not need any position sensor. The method is based on a d-q electrical model with harmonic decomposition without requiring any optimization algorithm to identify the parameters, thus reducing the computational burden. The algorithm was validated using two PMSMs with two different drives. Results presented show an accurate identification of the current space vector and the d-q inductances.

Focusing on the second methodology, an algorithm to identify PMSM parameters to reproduce the PMSM performance has been designed. The parameter identification was performed by applying stand-still experiments. The method does not require geometry knowledge while offering simplicity. A *d-q* electrical model was used to reproduce the PMSM performances considering copper and iron losses. The method was validated using the designed PMSM. First, the *d-q* flux linkages are compared against those obtained through FEA, showing similar values. A second validation is performed calculating the torque-speed-efficiency map. Then, it is compared against FEA and experimental maps. Results show high accuracy when reproducing PMSM performances. Therefore, the parameter estimation method is validated, providing detailed information of the PMSM performance. Thus, validating the third hypothesis.

9. Further Work

The elaboration of this thesis has contributed in several ways to three main fields of the electrical machines research, i.e., design and optimization field, parameter estimation and performance evaluation. Nevertheless, the study still in its early state. More contributions can be done in each of the developed topics.

Considering the design and optimization fields, and working in the same idea of considering the torque-speed-efficiency map as the optimization target, further work can be done. One of the most interesting points within the optimization stage is to apply multi objective optimization not only to the torque-speed-efficiency map but to other maps such as the torque-speed-power factor and temperature maps. Furthermore, it is necessary to study efficient ways of comparing matrices to be applied together with SSIM, thus increasing the optimization sensitivity. Regarding the applicability of the algorithm, different electrical machines topologies can be studied, specially highly saturated Synch-RMs to validate the iron losses model using magneto-static computations. Finally, further development in fast and efficient FEA modelling techniques are needed to avoid as much as possible the performance evaluation with electrical models.

Regarding the parameter estimation methodology, the model can be improved reducing the data dispersion and considering more harmonics without adding noise effects. Further development can be done to detect the flux weakening area, validating if efficient control is being applied or correcting the current control angles and magnitudes considering the parameter estimation values. Another interesting topic not completely studied in this thesis is the fault detection based on the same principle of power factor distortion due to the harmonic content.

Finally, in the same research field of electrical motor performance evaluation, an interesting research would be to complete this methodology with a strategy to identify and separate the iron losses produced in the stator and those produced in the rotor, greatly increasing the versatility of the methodology. More tests can be performed by adding improving the discretization of rotor angles and improving the current detection considering the saliency effect.

10. Thesis Scientific Dissemination

10.1 Journal articles

10.1.1 Electrical machines design and optimization

C. Candelo-Zuluaga, A. Garcia Espinosa, J. -R. Riba and P. T. Blanch, "PMSM Design for Achieving a Target Torque-Speed-Efficiency Map," in *IEEE Transactions on Vehicular Technology*, vol. 69, no. 12, pp. 14448-14457, Dec. 2020, doi: 10.1109/TVT.2020.3040313.

C. Candelo-Zuluaga, J. -R. Riba, A. Garcia Espinosa and P. Tubert, "Customized PMSM Design and Optimization Methodology for Water Pumping Applications," in *IEEE Transactions on Energy Conversion*, doi: 10.1109/TEC.2021.3088674.

10.1.2 Parameter estimation and performance analysis

C. Candelo-Zuluaga, J. -R. Riba and A. Garcia, "PMSM Parameter Estimation for Sensorless FOC Based on Differential Power Factor," in *IEEE Transactions on Instrumentation and Measurement*, doi: 10.1109/TIM.2021.3096861.

Candelo-Zuluaga, C.; Riba, J.-R.; Garcia, A. PMSM Performance Evaluation from Parameter Estimation Based on Stand Still Test. *Energies* **2021**, **Under minor revision**.

10.1.3 Other contributions

Candelo-Zuluaga, C.; Riba, J.-R.; López-Torres, C.; Garcia, A. Detection of Inter-Turn Faults in Multi-Phase Ferrite-PM Assisted Synchronous Reluctance Machines. *Energies* **2019**, *12*, 2733. <https://doi.org/10.3390/en12142733>.

Candelo-Zuluaga, C.; Riba, J.-R.; Thangamuthu, D.V.; Garcia, A. Detection of Partial Demagnetization Faults in Five-Phase Permanent Magnet Assisted Synchronous Reluctance Machines. *Energies* **2020**, *13*, 3496. <https://doi.org/10.3390/en13133496>.

10.2 Conference articles

10.2.1 Electrical machines design and optimization

C. Candelo-Zuluaga, A. G. Espinosa, J. Riba, P. T. Blanch and F. J. Descalzo, "Water-Pumping Permanent Magnet Synchronous Motor Optimization Based on Customized Torque-Speed Operating Area and Performance Characteristics," *IECON 2019 - 45th Annual Conference of the IEEE Industrial Electronics Society*, 2019, pp. 1471-1476, doi: 10.1109/IECON.2019.8927579.

C. Candelo-Zuluaga, A. G. Espinosa, J. -R. Riba and P. T. Blanch, "Computationally Efficient Analysis of Spatial and Temporal Harmonics Content of the Magnetic Flux Distribution in a PMSM for Efficiency Maps Computation," *2020 International Conference on Electrical Machines (ICEM)*, 2020, pp. 415-421, doi: 10.1109/ICEM49940.2020.9270900.

10.2.2 Parameter estimation and performance analysis

C. Candelo-Zuluaga, A. Garcia Espinosa, J. -R. Riba, P. Tubert Blanch and G. Rojas-Dueñas, "Fast and Efficient PMSM Electromagnetic Parameter Identification Methodology from the Efficiency Map," *IECON 2020 The 46th Annual Conference of the IEEE Industrial Electronics Society*, 2020, pp. 1584-1589, doi: 10.1109/IECON43393.2020.9254966.

10.2.3 Other contributions

G. Rojas-Dueñas, J. -R. Riba, M. Moreno-Eguilaz and **C. Candelo-Zuluaga**, "Non-Intrusive Parameter Identification of a Three-Phase Rectifier Based on an Optimization Approach," *IECON 2020 The 46th Annual Conference of the IEEE Industrial Electronics Society*, 2020, pp. 1389-1394, doi: 10.1109/IECON43393.2020.9254824.

11. Bibliography

- [1] E. D. N. Ndihi and S. Cherkaoui, "Simulation methods, techniques and tools of computer systems and networks," *Model. Simul. Comput. Networks Syst.*, pp. 485–504, Jan. 2015, doi: 10.1016/B978-0-12-800887-4.00017-1.
- [2] M. Baranyai, A. Mosavi, I. Vajda, and A. R. Varkonyi-Koczy, "Optimal Design of Electrical Machines: State of the Art Survey," Springer, Cham, 2018, pp. 209–216.
- [3] G. Pellegrino, T. M. Jahns, N. Bianchi, W. Soong, and F. Cupertino, *The Rediscovery of Synchronous Reluctance and Ferrite Permanent Magnet Motors*. Cham: Springer International Publishing, 2016.
- [4] E. A. Watson, "The economic aspect of the utilization of permanent magnets in electrical apparatus," *J. Inst. Electr. Eng.*, vol. 63, no. 344, pp. 822–834, Aug. 1925, doi: 10.1049/jjee-1.1925.0099.
- [5] F. Strauss, "Synchronous Machines with Rotating Permanent-Magnet Fields; Part II. Magnetic and Electrical Design Considerations [includes discussion]," *Trans. Am. Inst. Electr. Eng. Part III Power Appar. Syst.*, vol. 71, no. 4, pp. 887–893, Oct. 1952, doi: 10.1109/AIEEPAS.1952.4498552.
- [6] R. (Ramu) Krishnan, *Permanent magnet synchronous and brushless DC motor drives*, 2nd edn. Blacksburg: CRC Press, 2017.
- [7] "Ever Given accident: the implications for the future of shipping canals." <https://www.ship-technology.com/features/ever-given-accident-implication-future-shipping-canals/> (accessed Jul. 15, 2021).
- [8] "Neodymium | 2012-2021 Data | 2022-2023 Forecast | Price | Quote | Chart | Historical." <https://tradingeconomics.com/commodity/neodymium> (accessed Jul. 14, 2021).
- [9] "SS7 Series Eco PM Motor | YASKAWA." <https://www.yaskawa.com.sg/product/ac-inverter-drives/ss7-series-eco-pm-motor--permanent-magnet-synchronous-motor> (accessed Jul. 15, 2021).
- [10] "BMD - Servomotores : Bonfiglioli." <https://www.bonfiglioli.com/spain/es/producto/bmd---servomotores> (accessed Jul. 15, 2021).
- [11] "Low-voltage | VEM Group." <https://www.vem-group.com/en/products-services/low-voltage.html> (accessed Jul. 15, 2021).

- [12] A. Blondel, C. O. Mailloux, and C. A. Adams, *Synchronous Motors and Converters: Theory and Methods of Calculation and Testing*. McGraw-Hill Book Company, 1913.
- [13] J. K. Kostko, "Polyphase reaction synchronous motors," *J. Am. Inst. Electr. Eng.*, vol. 42, no. 11, pp. 1162–1168, Nov. 1923, doi: 10.1109/JoAIEE.1923.6591529.
- [14] "Synchronous reluctance motors - Process performance motors (IEC Low voltage motors) | ABB." <https://new.abb.com/motors-generators/iec-low-voltage-motors/process-performance-motors/synchronous-reluctance-motors> (accessed Jul. 15, 2021).
- [15] "LSHRM - Dyneo+ - Leroy-Somer Motors & Drives Productos." <https://acim.nidec.com/es-es/motors/leroy-somer/products/synchronous-reluctance-permanent-magnet-motors/lshrm> (accessed Jul. 15, 2021).
- [16] J. Corrales Martín, *Cálculo industrial de máquinas eléctricas*. Barcelona, Spain: Marcombo, 1982.
- [17] J. Pyrhönen, T. Jokinen, and V. Hrabovcová, *Design of Rotating Electrical Machines*, 2nd edn. Hoboken: Wiley, 2008.
- [18] J. F. Gieras, *Permanent magnet motor technology : design and applications*, 2nd edn. New York, United States: CRC Press, 2010.
- [19] D. C. Hanselman, *Brushless Permanent Magnet Motor Design*. Magna Physics Publishing, 2006.
- [20] M. Le Guyadec, L. Gerbaud, E. Vinot, V. Reinbold, and C. Dumont, "Use of reluctance network modelling and software component to study the influence of electrical machine pole number on hybrid electric vehicle global optimization," *Math. Comput. Simul.*, vol. 158, pp. 79–90, Apr. 2019, doi: 10.1016/J.MATCOM.2018.06.001.
- [21] J. Turowski, "Reluctance Networks," in *Computational Magnetism*, Dordrecht: Springer Netherlands, 1995, pp. 145–178.
- [22] J. Turowski, M. Turowski, and M. Kopec, "Method of three-dimensional network solution of leakage field of three-phase transformers," *IEEE Trans. Magn.*, vol. 26, no. 5, pp. 2911–2919, 1990, doi: 10.1109/20.104906.
- [23] K. Davey and E. King, "A Three Dimensional Scalar Potential Field Solution and its Application to the Turbine Generator End Region," *IEEE Trans. Power Appar. Syst.*, vol. PAS-100, no. 5, pp. 2302–2310, May 1981, doi: 10.1109/TPAS.1981.316744.

- [24] C. J. Carpenter, "Finite-element network models and their application to eddy-current problems," *Proc. Inst. Electr. Eng.*, vol. 122, no. 4, p. 455, 1975, doi: 10.1049/piee.1975.0125.
- [25] M. Djurovic and J. Monson, "Stray Losses in the Step of a Transformer Yoke with a Horizontal Magnetic Shunt," *IEEE Trans. Power Appar. Syst.*, vol. PAS-101, no. 8, pp. 2995–3000, Aug. 1982, doi: 10.1109/TPAS.1982.317629.
- [26] C. Lopez-Torres, A. Garcia Espinosa, J.-R. Riba, and L. Romeral, "Design and Optimization for Vehicle Driving Cycle of Rare-Earth-Free SynRM Based on Coupled Lumped Thermal and Magnetic Networks," *IEEE Trans. Veh. Technol.*, vol. 67, no. 1, pp. 196–205, Jan. 2018, doi: 10.1109/TVT.2017.2739020.
- [27] T. Raminosoa, I. Rasoanarivo, F. Meibody-Tabar, and F.-M. Sargos, "Time-Stepping Simulation of Synchronous Reluctance Motors Using a Nonlinear Reluctance Network Method," *IEEE Trans. Magn.*, vol. 44, no. 12, pp. 4618–4625, Dec. 2008, doi: 10.1109/TMAG.2008.2002996.
- [28] S. Asfirane, S. Hlioui, Y. Amara, O. D. La Barriere, G. Barakat, and M. Gabsi, "Global Quantities Computation Using Mesh-Based Generated Reluctance Networks," *IEEE Trans. Magn.*, vol. 54, no. 11, pp. 1–4, Nov. 2018, doi: 10.1109/TMAG.2018.2829155.
- [29] J. Nerg, M. Rilla, and J. Pyrhonen, "Thermal Analysis of Radial-Flux Electrical Machines With a High Power Density," *IEEE Trans. Ind. Electron.*, vol. 55, no. 10, pp. 3543–3554, Oct. 2008, doi: 10.1109/TIE.2008.927403.
- [30] E. MISHKIN, "THEORY OF THE SQUIRREL-CAGE INDUCTION MACHINE DERIVED DIRECTLY FROM MAXWELL'S FIELD EQUATIONS," *Q. J. Mech. Appl. Math.*, vol. 7, no. 4, pp. 472–487, Jan. 1954, doi: 10.1093/qjmam/7.4.472.
- [31] E. R. Laithwaite and S. A. Nasar, "Linear-Motion Electrical Machines," *Proc. IEEE*, vol. 58, no. 4, pp. 531–540, 1970, doi: 10.1109/PROC.1970.7692.
- [32] A. Fratta, G. P. Troglia, A. Vagati, and F. Villata, "Evaluation of torque ripple in high performance synchronous reluctance machines," in *Conference Record - IAS Annual Meeting (IEEE Industry Applications Society)*, 1993, vol. 1, pp. 163–170, doi: 10.1109/ias.1993.298919.
- [33] T. M. Jahns and W. L. Soong, "Pulsating torque minimization techniques for permanent magnet AC motor drives - A review," *IEEE Trans. Ind. Electron.*, vol. 43, no. 2, pp. 321–

- 330, 1996, doi: 10.1109/41.491356.
- [34] B. P. Alvarenga *et al.*, “Anisotropic layer model theory applied to synchronous machine analysis,” *IET Electr. Power Appl.*, vol. 14, no. 14, pp. 2873–2880, Dec. 2020, doi: 10.1049/iet-epa.2019.0887.
- [35] Y. M. Desai, *Finite element method with applications in engineering*. Dorling Kindersley, 2011.
- [36] I. Boldea and L. Tutelea, *Electric machines: steady state, transients, and design with MATLAB*. CRC Press, 2010.
- [37] N. Bianchi, T. M. Jahns, and W. . (2004. 10. 05. (Seattle, *Design, analysis, and control of interior PM synchronous machines: tutorial course notes; Seattle, Oct. 5, 2004*. CLEUP, 2004.
- [38] C. Lopez-Torres, G. Bacco, N. Bianchi, A. G. Espinosa, and L. Romeral, “A Parallel Analytical Computation of Synchronous Reluctance Machine,” in *2018 XIII International Conference on Electrical Machines (ICEM)*, Sep. 2018, pp. 25–31, doi: 10.1109/ICELMACH.2018.8507210.
- [39] S. J. (Sheppard J. Salon, *Finite Element Analysis of Electrical Machines*. Springer US, 1995.
- [40] N. Bianchi, *Electrical Machine Analysis Using Finite Elements*. CRC Press, 2005.
- [41] T. J. E. (Timothy J. E. Miller, *Brushless permanent-magnet and reluctance motor drives*. Oxford, United Kingdom: Clarendon Press, 1989.
- [42] C. Lopez-Torres, C. Colls, A. Garcia, J.-R. Riba, and L. Romeral, “Development of a Behavior Maps Tool to Evaluate Drive Operational Boundaries and Optimization Assessment of PMa-SynRMs,” *IEEE Trans. Veh. Technol.*, vol. 67, no. 8, pp. 6861–6871, Aug. 2018, doi: 10.1109/TVT.2018.2823339.
- [43] B. Silwal *et al.*, “Computation of Torque of an Electrical Machine With Different Types of Finite Element Mesh in the Air Gap,” *IEEE Trans. Magn.*, vol. 50, no. 12, pp. 1–9, Dec. 2014, doi: 10.1109/TMAG.2014.2333491.
- [44] G. Lei *et al.*, “A Review of Design Optimization Methods for Electrical Machines,” *Energies*, vol. 10, no. 12, p. 1962, Nov. 2017, doi: 10.3390/en10121962.
- [45] J. Bu, M. Zhou, X. Lan, and K. Lv, “Optimization for Airgap Flux Density Waveform of

- Flywheel Motor Using NSGA-2 and Kriging Model Based on MaxPro Design,” *IEEE Trans. Magn.*, vol. 53, no. 8, pp. 1–7, Aug. 2017, doi: 10.1109/TMAG.2017.2702758.
- [46] G. Lei, J. Zhu, and Y. Guo, *Multidisciplinary design optimization methods for electrical machines and drive systems*. Heidelberg, 2016.
- [47] A. G. Aissaoui, A. Tahour, and I. Colak, *Optimization and control of electrical machines*. IntechOpen, 2018.
- [48] A. Mosavi, “Optimal Engineering Design,” University of Debrecen, 2013.
- [49] P. Zhang, D. M. Ionel, and N. A. O. Demerdash, “Saliency ratio and power factor of IPM motors optimally designed for high efficiency and low cost objectives,” in *2014 IEEE Energy Conversion Congress and Exposition (ECCE)*, Sep. 2014, pp. 3541–3547, doi: 10.1109/ECCE.2014.6953882.
- [50] A. Mosavi, “Decision-Making in Complicated Geometrical Problems,” *Int. J. Comput. Appl.*, vol. 87, no. 19, pp. 22–25, Feb. 2014, doi: 10.5120/15460-4057.
- [51] H. Xu, S. Wang, and S.-Y. Wu, *Optimization methods, theory and applications*. Heidelberg, Germany: Springer, 2015.
- [52] X. Zhu, B. Yan, L. Chen, R. Zhang, L. Quan, and L. Mo, “Multi-Objective Optimization Design of a Magnetic Planetary Geared Permanent Magnet Brushless Machine by Combined Design of Experiments and Response Surface Methods,” *IEEE Trans. Magn.*, vol. 50, no. 11, pp. 1–4, Nov. 2014, doi: 10.1109/TMAG.2014.2326668.
- [53] “Chapter 12 Response surface methods,” *Data Handl. Sci. Technol.*, vol. 8, pp. 249–324, Jan. 1992, doi: 10.1016/S0922-3487(08)70259-4.
- [54] N. Taran, D. M. Ionel, and D. G. Dorrell, “Two-Level Surrogate-Assisted Differential Evolution Multi-Objective Optimization of Electric Machines Using 3-D FEA,” *IEEE Trans. Magn.*, vol. 54, no. 11, pp. 1–5, Nov. 2018, doi: 10.1109/TMAG.2018.2856858.
- [55] M. Khelifa, M. Mordjaoui, and A. Medoued, “An inverse problem methodology for design and optimization of an interior permanent magnetic BLDC motor,” *Int. J. Hydrogen Energy*, vol. 42, no. 28, pp. 17733–17740, Jul. 2017, doi: 10.1016/J.IJHYDENE.2017.02.017.
- [56] H. Jung, D. Kim, C. B. Lee, J. Ahn, and S. Y. Jung, “Numerical and experimental design validation for adaptive efficiency distribution compatible to frequent operating range of IPMSM,” *IEEE Trans. Magn.*, vol. 50, no. 2, Feb. 2014, doi: 10.1109/TMAG.2013.2285409.

- [57] J. Du, X. Wang, and H. Lv, "Optimization of Magnet Shape Based on Efficiency Map of IPMSM for EVs," *IEEE Trans. Appl. Supercond.*, vol. 26, no. 7, Oct. 2016, doi: 10.1109/TASC.2016.2594834.
- [58] C. Lopez-Torres, A. Garcia, J.-R. Riba, G. Lux, and L. Romeral, "Computationally Efficient Design and Optimization Approach of PMA-SynRM in Frequent Operating Torque–Speed Range," *IEEE Trans. Energy Convers.*, vol. 33, no. 4, pp. 1776–1786, Dec. 2018, doi: 10.1109/TEC.2018.2831249.
- [59] D. M. Ionel and M. Popescu, "Ultrafast finite-element analysis of brushless PM machines based on space-time transformations," *IEEE Trans. Ind. Appl.*, vol. 47, no. 2, pp. 744–753, Mar. 2011, doi: 10.1109/TIA.2010.2102733.
- [60] V. Ruuskanen, J. Nerg, J. Pyrhonen, S. Ruotsalainen, and R. Kennel, "Drive cycle analysis of a permanent-magnet traction motor based on magnetostatic finite-element analysis," *IEEE Trans. Veh. Technol.*, vol. 64, no. 3, pp. 1249–1254, Mar. 2015, doi: 10.1109/TVT.2014.2329014.
- [61] X. Wang, T. D. Strous, D. Lahaye, H. Polinder, and J. A. Ferreira, "Modeling and Optimization of Brushless Doubly-Fed Induction Machines Using Computationally Efficient Finite-Element Analysis," *IEEE Trans. Ind. Appl.*, vol. 52, no. 6, pp. 4525–4534, Nov. 2016, doi: 10.1109/TIA.2016.2593715.
- [62] H. Chen, X. Liu, N. A. O. Demerdash, A. M. El-Refaie, Z. Chen, and J. He, "Computationally efficient optimization of a five-phase flux-switching PM machine under different operating conditions," *IEEE Trans. Veh. Technol.*, vol. 68, no. 7, pp. 6495–6508, Jul. 2019, doi: 10.1109/TVT.2019.2915239.
- [63] L. Xu, W. Zhao, G. Liu, and C. Song, "Design Optimization of a Spoke-Type Permanent-Magnet Vernier Machine for Torque Density and Power Factor Improvement," *IEEE Trans. Veh. Technol.*, vol. 68, no. 4, pp. 3446–3456, Apr. 2019, doi: 10.1109/TVT.2019.2902729.
- [64] H. Fang and D. Wang, "A Novel Design Method of Permanent Magnet Synchronous Generator from Perspective of Permanent Magnet Material Saving," *IEEE Trans. Energy Convers.*, vol. 32, no. 1, pp. 48–54, Mar. 2017, doi: 10.1109/TEC.2016.2621133.
- [65] X. Sun, Z. Shi, G. Lei, Y. Guo, and J. Zhu, "Analysis and Design Optimization of a Permanent Magnet Synchronous Motor for a Campus Patrol Electric Vehicle," *IEEE Trans. Veh. Technol.*, vol. 68, no. 11, pp. 10535–10544, Nov. 2019, doi:

- 10.1109/TVT.2019.2939794.
- [66] M. Fasil, N. Mijatovic, B. B. Jensen, and J. Holboll, "Finite-Element Model-Based Design Synthesis of Axial Flux PMLDC Motors," *IEEE Trans. Appl. Supercond.*, vol. 26, no. 4, Jun. 2016, doi: 10.1109/TASC.2016.2537743.
- [67] H. C. Jung, G. J. Park, D. J. Kim, and S. Y. Jung, "Optimal Design and Validation of IPMSM for Maximum Efficiency Distribution Compatible to Energy Consumption Areas of HD-EV," *IEEE Trans. Magn.*, vol. 53, no. 6, Jun. 2017, doi: 10.1109/TMAG.2017.2660524.
- [68] C. T. Krasopoulos, M. E. Beniakar, and A. G. Kladas, "Multicriteria PM motor design based on ANFIS evaluation of EV driving cycle efficiency," *IEEE Trans. Transp. Electrification*, vol. 4, no. 2, pp. 525–535, Jun. 2018, doi: 10.1109/TTE.2018.2810707.
- [69] H. Dhulipati, E. Ghosh, S. Mukundan, P. Korta, J. Tjong, and N. C. Kar, "Advanced design optimization technique for torque profile improvement in six-phase pmsm using supervised machine learning for direct-drive ev," *IEEE Trans. Energy Convers.*, vol. 34, no. 4, pp. 2041–2051, Dec. 2019, doi: 10.1109/TEC.2019.2933619.
- [70] J. Y. Alsawalhi and S. D. Sudhoff, "Design optimization of asymmetric salient permanent magnet synchronous machines," *IEEE Trans. Energy Convers.*, vol. 31, no. 4, pp. 1315–1324, Dec. 2016, doi: 10.1109/TEC.2016.2575138.
- [71] O. Wallscheid and J. Böcker, "Global identification of a low-order lumped-parameter thermal network for permanent magnet synchronous motors," *IEEE Trans. Energy Convers.*, vol. 31, no. 1, pp. 354–365, Mar. 2016, doi: 10.1109/TEC.2015.2473673.
- [72] G. H. Jang, J. H. Ahn, B. O. Kim, D. H. Lee, J. S. Bang, and J. Y. Choi, "Design and Characteristic Analysis of a High-Speed Permanent Magnet Synchronous Motor Considering the Mechanical Structure for High-Speed and High-Head Centrifugal Pumps," *IEEE Trans. Magn.*, vol. 54, no. 11, pp. 1–6, Nov. 2018, doi: 10.1109/TMAG.2018.2845874.
- [73] T. R. Brinner, R. H. McCoy, and T. Kopecky, "Induction versus permanent-magnet motors for electric submersible pump field and laboratory comparisons," *IEEE Trans. Ind. Appl.*, vol. 50, no. 1, pp. 174–181, 2014, doi: 10.1109/TIA.2013.2288203.
- [74] R. Antonello, M. Carraro, A. Costabeber, F. Tinazzi, and M. Zigliotto, "Energy-Efficient Autonomous Solar Water-Pumping System for Permanent-Magnet Synchronous Motors," *IEEE Trans. Ind. Electron.*, vol. 64, no. 1, pp. 43–51, Jan. 2017, doi:

- 10.1109/TIE.2016.2595480.
- [75] B. Singh and S. Murshid, "A grid-interactive permanent-magnet synchronous motor-driven solar water-pumping system," *IEEE Trans. Ind. Appl.*, vol. 54, no. 5, pp. 5549–5561, Sep. 2018, doi: 10.1109/TIA.2018.2860564.
- [76] S. Murshid and B. Singh, "Energy-efficient single-stage solar PV powered sensorless PMSM drive for water pumping," *IET Renew. Power Gener.*, vol. 13, no. 13, pp. 2267–2277, Oct. 2019, doi: 10.1049/iet-rpg.2018.6205.
- [77] S. Murshid and B. Singh, "Implementation of PMSM Drive for a Solar Water Pumping System," in *IEEE Transactions on Industry Applications*, Sep. 2019, vol. 55, no. 5, pp. 4956–4964, doi: 10.1109/TIA.2019.2924401.
- [78] O. Beik, "Design Optimization of a PM Motor: A Practical Approach for Mass Production," *IEEE Trans. Energy Convers.*, vol. 35, no. 4, pp. 1849–1858, Dec. 2020, doi: 10.1109/TEC.2020.2991531.
- [79] A. Al-Timimy *et al.*, "Design and Losses Analysis of a High Power Density Machine for Flooded Pump Applications," *IEEE Trans. Ind. Appl.*, vol. 54, no. 4, pp. 3260–3270, Jul. 2018, doi: 10.1109/TIA.2018.2821623.
- [80] Z. H. Liu, H. L. Wei, X. H. Li, K. Liu, and Q. C. Zhong, "Global Identification of Electrical and Mechanical Parameters in PMSM Drive Based on Dynamic Self-Learning PSO," *IEEE Trans. Power Electron.*, vol. 33, no. 12, pp. 10858–10871, Dec. 2018, doi: 10.1109/TPEL.2018.2801331.
- [81] O. Sandre-Hernandez, R. Morales-Caporal, J. Rangel-Magdaleno, H. Peregrina-Barreto, and J. N. Hernandez-Perez, "Parameter Identification of PMSMs Using Experimental Measurements and a PSO Algorithm," *IEEE Trans. Instrum. Meas.*, vol. 64, no. 8, pp. 2146–2154, Aug. 2015, doi: 10.1109/TIM.2015.2390958.
- [82] K. Liu, J. Feng, S. Guo, L. Xiao, and Z. Q. Zhu, "Identification of flux linkage map of permanent magnet synchronous machines under uncertain circuit resistance and inverter nonlinearity," *IEEE Trans. Ind. Informatics*, vol. 14, no. 2, pp. 556–568, Feb. 2018, doi: 10.1109/TII.2017.2722470.
- [83] M. S. Rifaq and J. W. Jung, "A Comprehensive Review of State-of-the-Art Parameter Estimation Techniques for Permanent Magnet Synchronous Motors in Wide Speed Range," *IEEE Trans. Ind. Informatics*, vol. 16, no. 7, pp. 4747–4758, Jul. 2020, doi:

- 10.1109/TII.2019.2944413.
- [84] E. Armando, R. I. Bojoi, P. Guglielmi, G. Pellegrino, and M. Pastorelli, "Experimental identification of the magnetic model of synchronous machines," *IEEE Trans. Ind. Appl.*, vol. 49, no. 5, pp. 2116–2125, 2013, doi: 10.1109/TIA.2013.2258876.
- [85] G. Pellegrino, B. Boazzo, and T. M. Jahns, "Magnetic Model Self-Identification for PM Synchronous Machine Drives," *IEEE Trans. Ind. Appl.*, vol. 51, no. 3, pp. 2246–2254, May 2015, doi: 10.1109/TIA.2014.2365627.
- [86] S. A. Odhano, R. Bojoi, Ş. G. Roşu, and A. Tenconi, "Identification of the Magnetic Model of Permanent-Magnet Synchronous Machines Using DC-Biased Low-Frequency AC Signal Injection," *IEEE Trans. Ind. Appl.*, vol. 51, no. 4, pp. 3208–3215, Jul. 2015, doi: 10.1109/TIA.2015.2413383.
- [87] A. Hosfeld, F. Hiester, and U. Konigorski, "Analysis of DC Motor Current Waveforms Affecting the Accuracy of 'Sensorless' Angle Measurement," *IEEE Trans. Instrum. Meas.*, vol. 70, 2021, doi: 10.1109/TIM.2020.3034598.
- [88] J. Kim and J. S. Lai, "Quad Sampling Incremental Inductance Measurement through Current Loop for Switched Reluctance Motor," *IEEE Trans. Instrum. Meas.*, vol. 69, no. 7, pp. 4251–4257, Jul. 2020, doi: 10.1109/TIM.2019.2949319.
- [89] G. Feng, C. Lai, K. Mukherjee, and N. C. Kar, "Current Injection-Based Online Parameter and VSI Nonlinearity Estimation for PMSM Drives Using Current and Voltage DC Components," *IEEE Trans. Transp. Electr.*, vol. 2, no. 2, pp. 119–128, Jun. 2016, doi: 10.1109/TTE.2016.2538180.
- [90] M. S. Rifaq, F. Mwasilu, J. Kim, H. H. Choi, and J. W. Jung, "Online Parameter Identification for Model-Based Sensorless Control of Interior Permanent Magnet Synchronous Machine," *IEEE Trans. Power Electron.*, vol. 32, no. 6, pp. 4631–4643, Jun. 2017, doi: 10.1109/TPEL.2016.2598731.
- [91] O. C. Kivanc and S. B. Ozturk, "Sensorless PMSM Drive Based on Stator Feedforward Voltage Estimation Improved with MRAS Multiparameter Estimation," *IEEE/ASME Trans. Mechatronics*, vol. 23, no. 3, pp. 1326–1337, Jun. 2018, doi: 10.1109/TMECH.2018.2817246.
- [92] R. Raja, T. Sebastian, and M. Wang, "Online stator inductance estimation for permanent magnet motors using PWM excitation," *IEEE Trans. Transp. Electr.*, vol. 5, no. 1, pp. 107–

- 117, Mar. 2019, doi: 10.1109/TTE.2019.2891047.
- [93] D. Liang, J. Li, R. Qu, and W. Kong, "Adaptive second-order sliding-mode observer for PMSM sensorless control considering VSI Nonlinearity," *IEEE Trans. Power Electron.*, vol. 33, no. 10, pp. 8994–9004, Oct. 2018, doi: 10.1109/TPEL.2017.2783920.
- [94] Y. Yan, J. Yang, Z. Sun, C. Zhang, S. Li, and H. Yu, "Robust Speed Regulation for PMSM Servo System with Multiple Sources of Disturbances via an Augmented Disturbance Observer," *IEEE/ASME Trans. Mechatronics*, vol. 23, no. 2, pp. 769–780, Apr. 2018, doi: 10.1109/TMECH.2018.2799326.
- [95] W. Lu, B. Tang, K. Ji, K. Lu, D. Wang, and Z. Yu, "A New Load Adaptive Identification Method Based on an Improved Sliding Mode Observer for PMSM Position Servo System," *IEEE Trans. Power Electron.*, vol. 36, no. 3, pp. 3211–3223, Mar. 2021, doi: 10.1109/TPEL.2020.3016713.
- [96] W. Deng, C. Xia, Y. Yan, Q. Geng, and T. Shi, "Online Multiparameter Identification of Surface-Mounted PMSM Considering Inverter Disturbance Voltage," *IEEE Trans. Energy Convers.*, vol. 32, no. 1, pp. 202–212, Mar. 2017, doi: 10.1109/TEC.2016.2621130.
- [97] L. Colombo, M. L. Corradini, A. Cristofaro, G. Ippoliti, and G. Orlando, "An Embedded Strategy for Online Identification of PMSM Parameters and Sensorless Control," *IEEE Trans. Control Syst. Technol.*, vol. 27, no. 6, pp. 2444–2452, Nov. 2019, doi: 10.1109/TCST.2018.2862415.
- [98] C. Wu, Y. Zhao, and M. Sun, "Enhancing Low-Speed Sensorless Control of PMSM Using Phase Voltage Measurements and Online Multiple Parameter Identification," *IEEE Trans. Power Electron.*, vol. 35, no. 10, pp. 10700–10710, Oct. 2020, doi: 10.1109/TPEL.2020.2978200.
- [99] M. Pulvirenti, G. Scarcella, G. Scelba, A. Testa, and M. M. Harbaugh, "On-line stator resistance and permanent magnet flux linkage identification on open-end winding PMSM Drives," in *IEEE Transactions on Industry Applications*, Jan. 2019, vol. 55, no. 1, pp. 504–515, doi: 10.1109/TIA.2018.2869877.
- [100] H. Wang, K. Lu, D. Wang, and F. Blaabjerg, "Online Identification of Intrinsic Load Current Dependent Position Estimation Error for Sensorless PMSM Drives," *IEEE Access*, vol. 8, pp. 163186–163196, Aug. 2020, doi: 10.1109/access.2020.3019690.
- [101] Q. Wang, G. Wang, N. Zhao, G. Zhang, Q. Cui, and D. Xu, "An Impedance Model-Based

- Multiparameter Identification Method of PMSM for Both Offline and Online Conditions,” *IEEE Trans. Power Electron.*, vol. 36, no. 1, pp. 727–738, Jan. 2021, doi: 10.1109/TPEL.2020.3000896.
- [102] A. Belqorchi, U. Karaagac, J. Mahseredjian, and I. Kamwa, “Standstill Frequency Response Test and Validation of a Large Hydrogenerator,” *IEEE Trans. Power Syst.*, vol. 34, no. 3, pp. 2261–2269, May 2019, doi: 10.1109/TPWRS.2018.2889510.
- [103] Q. Wang, G. Zhang, G. Wang, C. Li, and D. Xu, “Offline Parameter Self-Learning Method for General-Purpose PMSM Drives with Estimation Error Compensation,” *IEEE Trans. Power Electron.*, vol. 34, no. 11, pp. 11103–11115, Nov. 2019, doi: 10.1109/TPEL.2019.2900559.
- [104] X. Wu, X. Fu, M. Lin, and L. Jia, “Offline Inductance Identification of IPMSM with Sequence-Pulse Injection,” *IEEE Trans. Ind. Informatics*, vol. 15, no. 11, pp. 6127–6135, Nov. 2019, doi: 10.1109/TII.2019.2932796.
- [105] N. Leboeuf, T. Boileau, B. Nahid-Mobarakeh, N. Takorabet, F. Meibody-Tabar, and G. Clerc, “Estimating permanent-magnet motor parameters under inter-turn fault conditions,” in *IEEE Transactions on Magnetics*, Feb. 2012, vol. 48, no. 2, pp. 963–966, doi: 10.1109/TMAG.2011.2177642.
- [106] F. S. Sellschopp and M. A. Arjona, “Determination of synchronous machine parameters using standstill frequency response tests at different excitation levels,” in *Proceedings of IEEE International Electric Machines and Drives Conference, IEMDC 2007*, 2007, vol. 2, pp. 1014–1019, doi: 10.1109/IEMDC.2007.382815.
- [107] E. da C. Bortoni and J. A. Jardini, “A standstill frequency response method for large salient pole synchronous machines,” *IEEE Trans. Energy Convers.*, vol. 19, no. 4, pp. 687–691, Dec. 2004, doi: 10.1109/TEC.2004.832047.
- [108] T. L. Vandoorn, F. M. De Belie, T. J. Vyncke, J. A. Melkebeek, and P. Lataire, “Generation of multisinusoidal test signals for the identification of synchronous-machine parameters by using a voltage-source inverter,” *IEEE Trans. Ind. Electron.*, vol. 57, no. 1, pp. 430–439, Jan. 2010, doi: 10.1109/TIE.2009.2031135.
- [109] “115-2009 - IEEE Guide for Test Procedures for Synchronous Machines Part I—Acceptance and Performance Testing Part II—Test Procedures and Parameter Determination for Dynamic Analysis - Redline | IEEE Standard | IEEE Xplore.”

- <https://ieeexplore-ieee-org.recursos.biblioteca.upc.edu/document/5953453> (accessed Jun. 19, 2021).
- [110] J. Zou, D. Zeng, Y. Xu, B. Wang, and Q. Wang, “An Indirect Testing Method for the Mechanical Characteristic of Multiunit Permanent-Magnet Synchronous Machines With Concentrated Windings,” *IEEE Trans. Ind. Electron.*, vol. 62, no. 12, pp. 7402–7411, Dec. 2015, doi: 10.1109/TIE.2015.2455018.
- [111] J. Zou and Y. Xu, “Analysis and Discussion of the Indirect Testing Method for the Losses of Permanent Magnet Synchronous Machines,” *IEEE Trans. Magn.*, vol. 54, no. 11, Nov. 2018, doi: 10.1109/TMAG.2018.2855934.
- [112] G. Feng, C. Lai, and N. C. Kar, “Practical Testing Solutions to Optimal Stator Harmonic Current Design for PMSM Torque Ripple Minimization Using Speed Harmonics,” *IEEE Trans. Power Electron.*, vol. 33, no. 6, pp. 5181–5191, Jun. 2018, doi: 10.1109/TPEL.2017.2738613.
- [113] Z. Wang, A. C. Bovik, H. R. Sheikh, and E. P. Simoncelli, “Image Quality Assessment: From Error Visibility to Structural Similarity,” *IEEE Trans. Image Process.*, vol. 13, no. 4, pp. 600–612, Apr. 2004, doi: 10.1109/TIP.2003.819861.
- [114] F. Verbelen, A. Abdalh, H. Vansompel, K. Stockman, and P. Sergeant, “Sizing Methodology Based on Scaling Laws for a Permanent Magnet Electrical Variable Transmission,” *IEEE Trans. Ind. Electron.*, vol. 67, no. 3, pp. 1739–1749, Mar. 2020, doi: 10.1109/TIE.2019.2903763.
- [115] A. Mahmoudi, W. L. Soong, G. Pellegrino, and E. Armando, “Loss Function Modeling of Efficiency Maps of Electrical Machines,” *IEEE Trans. Ind. Appl.*, vol. 53, no. 5, pp. 4221–4231, Sep. 2017, doi: 10.1109/TIA.2017.2695443.
- [116] S. Stipetic, J. Goss, D. Zarko, and M. Popescu, “Calculation of Efficiency Maps Using a Scalable Saturated Model of Synchronous Permanent Magnet Machines,” *IEEE Trans. Ind. Appl.*, vol. 54, no. 5, pp. 4257–4267, Sep. 2018, doi: 10.1109/TIA.2018.2837672.
- [117] C. Candelo-Zuluaga, A. G. Espinosa, J.-R. Riba, P. T. Blanch, and F. J. Descalzo, “Water-Pumping Permanent Magnet Synchronous Motor Optimization Based on Customized Torque-Speed Operating Area and Performance Characteristics,” Dec. 2019, pp. 1471–1476, doi: 10.1109/iecon.2019.8927579.
- [118] R. H. Staunton, C. W. Ayers, L. D. Marlino, J. N. Chiasson, and B. A. Burress, “Evaluation

- of 2004 Toyota Prius Hybrid Electric Drive System,” Oak Ridge, TN (United States), May 2006. doi: 10.2172/890029.
- [119] T. A. Burress *et al.*, “Evaluation of the 2007 Toyota Camry Hybrid Synergy Drive System,” Oak Ridge, TN (United States), Apr. 2008. doi: 10.2172/928684.
- [120] N. Bianchi, *Theory and design of fractional-slot PM machines : IEEE IAS tutorial course [sic] notes*. CLEUP, 2007.
- [121] “Emetor - Electric motor winding calculator.” <https://www.emetor.com/windings/> (accessed Jul. 21, 2021).
- [122] I. 5199:2002(en), *Technical specifications for centrifugal pumps — Class II*. International Organization for Standardization, Geneva, Switzerland.
- [123] N. Bernard, R. Missoum, L. Dang, N. Bekka, H. Ben Ahmed, and M. E. H. Zaim, “Design Methodology for High-Speed Permanent Magnet Synchronous Machines,” *IEEE Trans. Energy Convers.*, vol. 31, no. 2, pp. 477–485, Jun. 2016, doi: 10.1109/TEC.2015.2513669.
- [124] *IEC 60034-30-1:2014 Rotating Electrical Machines-Part 30-1: Efficiency classes of line operated AC motors (IE code)*. .
- [125] J. Nakatsugawa, Y. Notohara, D. Li, and Y. Iwaji, “Inductance measurement method for permanent magnet synchronous motors using AC with DC bias,” 2008, doi: 10.1109/ICELMACH.2008.4800054.
- [126] “Dell Black Precision 7820 Tower Workstation, Rs 190000 /piece | ID: 19009211197.” <https://www.indiamart.com/proddetail/dell-precision-7820-tower-workstation-19009211197.html> (accessed Jun. 28, 2019).
- [127] “Intel Core i9 7940X @ 3798.68 MHz - CPU-Z VALIDATOR.” <https://valid.x86.fr/l4gldm> (accessed Jun. 28, 2019).
- [128] “LMG450 - Power Analyzer - ZES ZIMMER.” <https://www.zes.com/en/Products/Precision-Power-Analyzers/LMG450> (accessed Jun. 28, 2019).
- [129] “7986874-40.jpg (JPEG Image, 2000 × 1026 pixels) — Scaled (59%).” https://es.farnell.com/productimages/large/en_GB/7986874-40.jpg (accessed May 22, 2021).
- [130] “A621 A622 Current Probes Datasheet | Enhanced Reader.” <moz-extension://12ec33d7-c075-4592-8a49-eb4a5e6c134c/enhanced->

- reader.html?openApp&pdf=http%3A%2F%2Fwww.farnell.com%2Fdatasheets%2F2239667.pdf (accessed May 22, 2021).
- [131] “81KwOSHutFL._AC_SX355_.jpg (JPEG Image, 355 × 339 pixels).” https://images-na.ssl-images-amazon.com/images/I/81KwOSHutFL._AC_SX355_.jpg (accessed Jul. 09, 2021).
- [132] “Pinza amperimétrica CA/CC i30s | Fluke.” <https://www.fluke.com/es-es/producto/accesorios/pinzas-de-corriente/fluke-i30s#> (accessed Jul. 09, 2021).
- [133] “5S Components |VS750B | VS Traction Voltage Sensors.” <https://www.5scomponents.com/vs750b> (accessed May 22, 2021).
- [134] “articles-news-torque-meter-with-cylindrical-shaft-stubs.png (PNG Image, 673 × 412 pixels).” <https://www.eeweb.com/wp-content/uploads/articles-news-torque-meter-with-cylindrical-shaft-stubs.png> (accessed May 22, 2021).
- [135] “high-temperature-thermocouple-type-k-exposed-tip-plug-40-to-1000c.jpg (JPEG Image, 800 × 800 pixels) — Scaled (75%).” <https://www.priggen.com/media/image/product/18253/lg/high-temperature-thermocouple-type-k-exposed-tip-plug-40-to-1000c.jpg> (accessed May 22, 2021).
- [136] “PCIe-6259 - NI.” <https://www.ni.com/es-es/support/model.pcie-6259.html> (accessed May 22, 2021).
- [137] “SCB-68 - NI.” <https://www.ni.com/es-es/support/model.scb-68.html> (accessed May 22, 2021).
- [138] “USB-6353 - NI.” <https://www.ni.com/es-es/support/model.usb-6353.html> (accessed Jul. 09, 2021).
- [139] “DEVICE SPECIFICATIONS NI 6353 X Series Data Acquisition: 1.25 MS/s, 32 AI, 48 DIO, 4 AO.”
- [140] “APM SP300VAC600W Advanced Programmable AC Source | Batter Fly.” <https://www.batterfly.com/shop/es/apm-sp300vac600w-a> (accessed Jul. 09, 2021).
- [141] “ABB AC Brushless Servodrives DGV Converters for driving Brushless AC Permanent Magnet Servomotors Installation Manual,” 2003, doi: 10.02.2005.
- [142] “YROTATE-IT-RX23T |.” <https://www.renesas.com/eu/en/products/boards-and-kits/device/YROTATE-IT-RX23T.html> (accessed Jun. 28, 2019).

Appendix - Resources

This section presents the different resources used to develop the research, including software, hardware, measurement devices, test benches and motor drives.

A.1 Software

The software used is listed below:

- MATLAB®: Mathematical environment for programming and developing different models and algorithms.
- COMSOL Multiphysics 5.2®: Multiphysics finite element analysis software for general purposes.
- Altair FLUX®: Electromagnetic and thermal finite element analysis software focused in electrical machines.
- Motor CAD®: Thermal lumped parameters analysis software focused in electrical machines.
- Microsoft Word®: Text editor.
- Microsoft Visio®: Diagrams creator.
- AutoCAD®: CAD software.

A.2 Hardware

Figure 71 shows the workstation used during the three years of development.



Figure 71: Dell Precision 7820 Workstation [126]

- Processor: Intel® Core™ i9-7940X CPU @ 3.10 GHz 3.10 GHz.

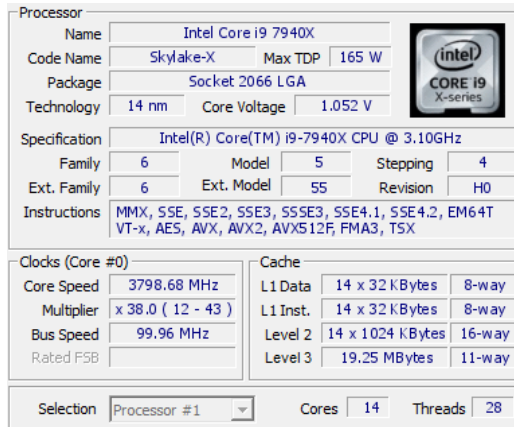


Figure 72: CPU features [127]

- RAM: 64 GB.

A.3 Measurement devices

The measuring devices used for the project development are detailed below.

A.3.1 Power analyzers

- ZES ZIMMER LMG450:

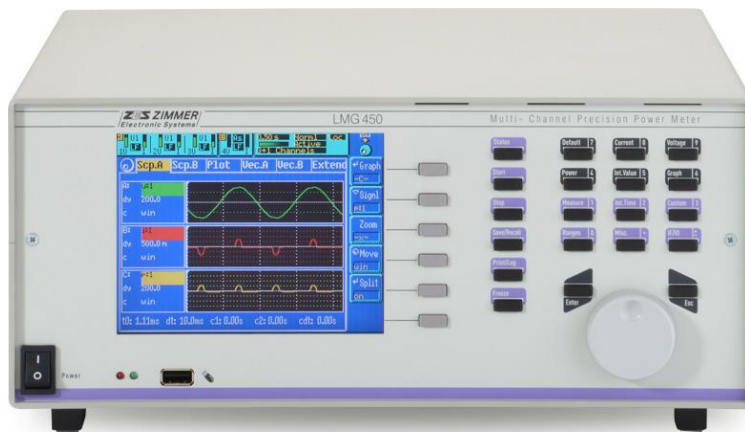


Figure 73: Zimmer four channel power analyzer LMG450 [128]

Table 47: ZES Zimmer power analyzer LMG450 characteristics

Characteristic	LMG450
Measurement ranges	Direct Voltage: 6-600 Vrms Direct Current: 0.6-16 Arms

A.3.2 Current transducers

Two different current transducers have been used.

- Tektronix A622 current probe:



Figure 74: Tektronix A622 current probe [129]

Table 48: Tektronix A622 current probe characteristics [130]

Characteristic	A622
Frequency range	DC to 100 kHz
Maximum input current	100 A peak
Output	10 mV/A, 100 mV/A
Maximum conductor diameter	11.8 mm
Termination	BNC
Maximum bare-wire voltage	600 V (CAT III)
Safety	UL3111-2-032, CSA1010.2.032, EN61010-2-032, IEC61010-2-032

- Current Clamp FLUKE i30s:



Figure 75: FLUKE i30s current clamp [131]

Table 49: FLUKE i30s current clamp characteristics [132]

Characteristic	FLUKE i30s
Frequency range	DC to 100 kHz (0.5 dB)
Measurement range	± 30 A
Maximum input current	500 A
Output	100 mV/A
Resolution	± 1 mA
Termination	BNC

A.3.3 Voltage transducers

To measure line voltages, ABB VS750B is selected.

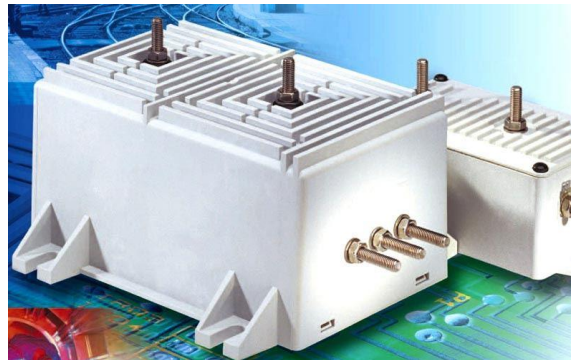


Figure 76: ABB VS750B voltage transducer [133]

Table 50: ABB VS750B voltage transducer characteristics [133]

Characteristic	VS750B
Nominal primary voltage (U_{PN})	750 V
Measuring range (U_P max)	± 1125 V
Secondary current (I_s) at U_{PN}	50 mA
Supply voltage	$\pm 12V / \pm 24V$
Accuracy at U_{PN}	$\pm 0.3-0.9$ %

A.3.4 Torque transducer

The torque transducer used to perform the experimental tests was the HBM T20WN.



Figure 77: HBM T20WN torque transducer [134]

Table 51: HBM T20WN torque transducer characteristics

Torque measuring system	
Characteristic	T20WN
Nominal sensitivity	± 10 V
Characteristic tolerance	± 0.2 %
Power supply	12 V DC (10.8-13.2) V
Linearity deviation	± 0.1 %
Secondary current (I_s) at U_{PN}	50 mA
Nominal speed	10000 rpm
Speed/angle of rotation measurement system	
Measurement system	Visual
Pulses per rotation	360
Output signal	5 V (asymmetric); Two square signals 90° shifted

A.3.5 Temperature sensors

For measuring temperature, a type K thermocouple is selected.



Figure 78: Thermocouple type K [135]

Table 52: Thermocouple type K characteristics [135]

Characteristic	Type K thermocouple
Temperature Measurement Range	-75 °C to 250 °C

A.4 Data acquisition devices

A.4.1 DAQ NI PCI 6259 / NI SCB 68

For the acquisition and synchronization of data the DAQ NI PCI 6259 with NI SCB 68 is used.



Figure 79: DAQ NI PCI 6259 (a) [136] and NI SCB 68 (b) [137]

Table 53: DAQ NI PCI 6259 [136] and NI SCB 68 [137] characteristics

DAQ NI PCI 6259/NI SCB 68	
Number of channels	16 differential or 32 single ended
ADC resolution	16 bits
Sample rate	Single channel 1.25 MS/s
	Multichannel maximum 1.00 MS/s
Input range	$\pm 0.1, 0.2, 0.5, 1, 2, 5$ and 10 V

A.4.2 DAQ NI-6353



Figure 80: NI USB-6353 DAQ [138]

Table 54: DAQ NI-6353 [139]

DAQ NI-6353	
Number of channels	16 differential or 32 single ended
ADC resolution	16 bits
Sample rate	Single channel 1.25 MS/s
	Multichannel maximum 1.00 MS/s
Input range	$\pm 0.1, 0.2, 0.5, 1, 2, 5$ and 10 V

A.5 Voltage sources



Figure 81: SP300VAC600W [140]

Table 55: SP300VAC600W Voltage Source specifications [140]

SP300VAC600W Voltage Source	
Output frequency range	15 – 1000 Hz
Built in IEC standard	IEC1000-4-11

A.6 Motor drives

Two different motor drives are used for the experimental validation.

A.6.1 ABB DGV700 converter

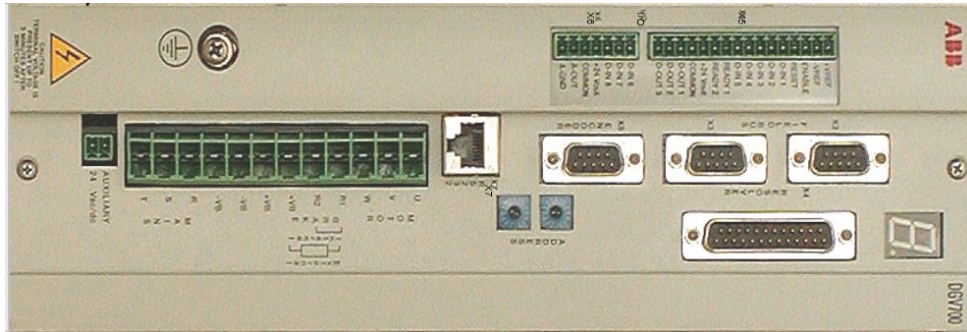


Figure 82: ABB DGV700 converter [141]

Table 56: ABB DGV700 converter characteristics [141]

ABB DGV700 converter	
Power supply phase to phase voltage	3~ 110-440 V _{RMS} ± 10%
Power supply frequency	50/60 Hz
Auxiliary supply voltage	21-36 V _{DC} – 40 VA
Max Auxiliary supply current	2 A _{DC}
Rated input current I _{VN}	13.8 A _{RMS}
Rated output current I _{aN}	13 A _{RMS}
Output continuous power (400 V)	9 kVA
Control Algorithm	FOC with 90° current control and flux weakening

A.6.2 YROTATE-IT-RX23T drive

The brushless motor kit YROTATE-IT-RX23T. This tool allows to apply field oriented control (FOC) with field weakening capability.

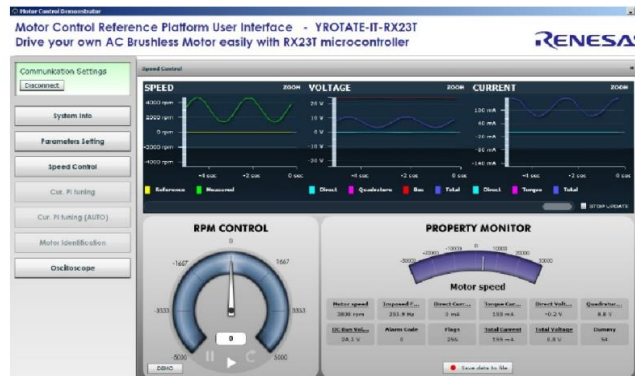
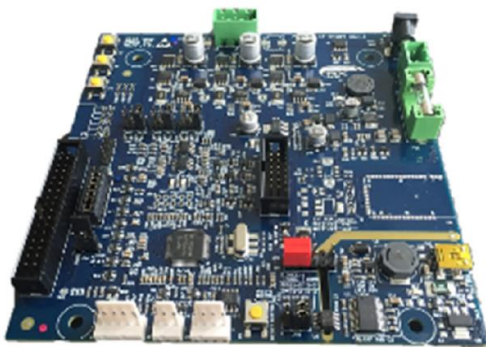


Figure 83: Brushless motor kit YROTATE-IT-RX23T [142]

Table 57: YROTATE-IT-RX23T characteristics

YROTATE-IT-RX23T characteristics	
Power supply phase to phase voltage	1~ 230 V _{RMS}
Power supply frequency	50/60 Hz
Output continuous power (220 V)	2 kW
Control Algorithm	FOC with 90° current control and flux weakening

A.8 APICOM Cento test bench

A second test bench is used to validate the electrical machine performance. This bench is composed by a Foucault current brake and a system to control the torque load. The axis is composed by a Gimbal coupling allowing to correct possible misalignments. The motor is fixed by a manual system allowing to correct the axis position in any direction and angle.

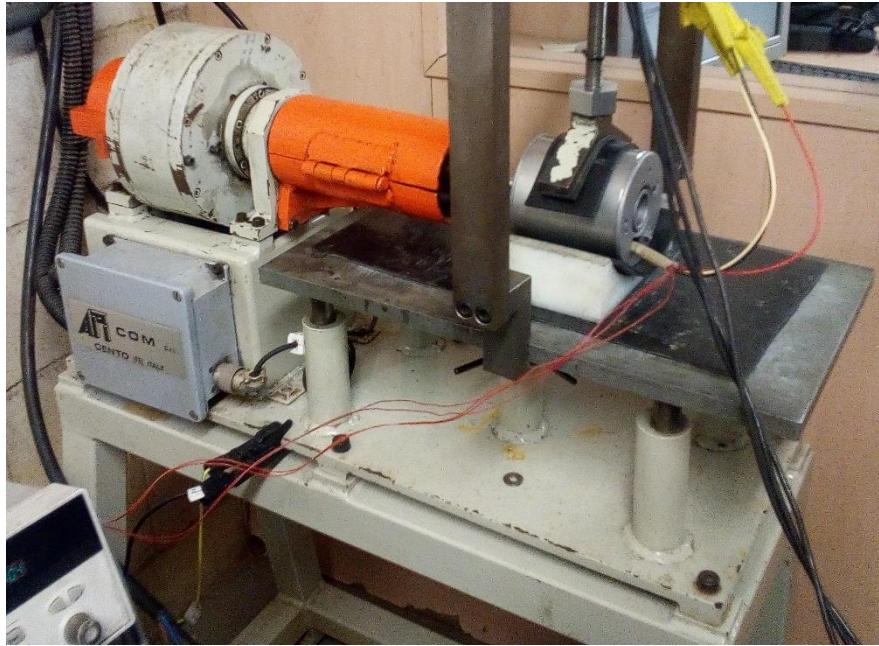


Figure 85: Apicom cento test bench (eddy current dynamometer)

A.9 Parameter estimation and performance evaluation test bench

Alternatively, a parameter estimation experimental setup for performance evaluation is designed. The motor is connected to a programmable single phase source. Then, voltage is acquired through a voltage divider and the current magnitude through a transducer. These are connected to a data acquisition device. Regarding the PMSM, its rotor is blocked in different angle positions. The positive terminal of the AC source is connected to one of the motor phases which is considered as the reference phase, and the negative terminal is connected to the two remaining phases.

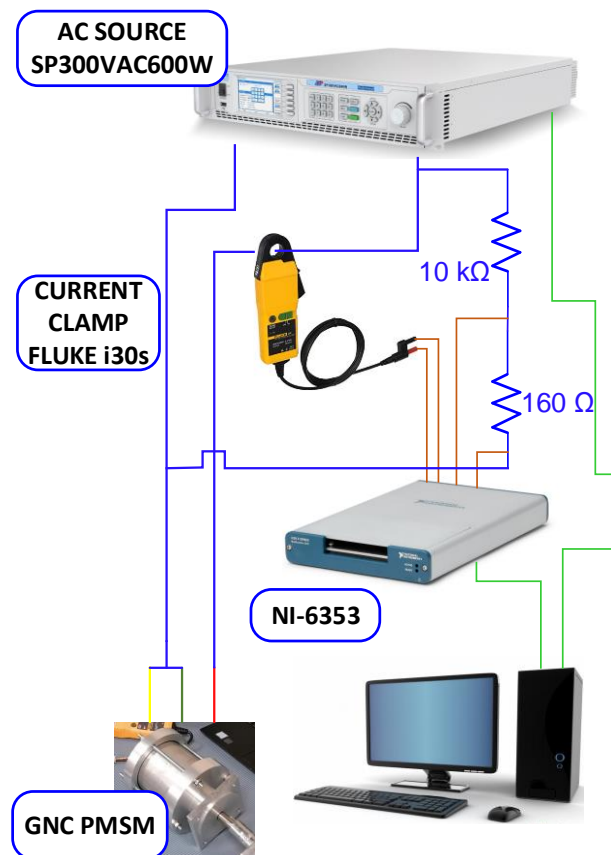


Figure 86: Alternative parameter estimation experimental set up

